Crystallization of Calcium Sulphate during Phosphoric Acid Production: Improving Filtration through Improvement in Particle Shape and Size Distribution

by

You Peng

B.Eng., National University of Singapore (2011)

M.S.CEP, Massachusetts Institute of Technology (2013)

Submitted to the Department of Chemical Engineering
in partial fulfillment of the requirements for the degree of
Doctor of Philosophy in Chemical Engineering
at the
MASSACHUSETTS INSTITUTE OF TECHNOLOGY
September 2017

Signature redacted

Author .....
Department of Chemical Engineering
August 23, 2017

Signature redacted

Certified by .....
Allan S. Myerson
Professor of the Practice of Chemical Engineering
Thesis Supervisor

Signature redacted

Certified by .....
Richard D. Braatz
Edward R. Gilliland Professor in Chemical Engineering
Thesis Supervisor

Signature redacted

Accepted by .....
Patrick S. Doyle
Robert T. Haslam Professor of Chemical Engineering
Chairman, Committee for Graduate Students

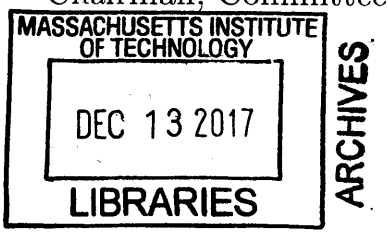

Crystallization of Calcium Sulphate during Phosphoric Acid Production: Improving Filtration through Improvement in Particle Shape and Size Distribution

by

You Peng

Submitted to the Department of Chemical Engineering
on August 23, 2017, in partial fulfillment of the
requirements for the degree of
Doctor of Philosophy in Chemical Engineering

Abstract

The production of phosphoric acid from phosphate mineral rock involves the addition of phosphate rock to a concentrated sulfuric acid solution. The induced reactive crystallization process produces a side product of calcium sulfate hydrates, which become the filter media in the subsequent acid separation process. For most industrial processes, the dihydrate form of calcium sulfate crystals (gypsum) precipitates and its shape and size distribution are key factors in determining the downstream filtration efficiency. Particularly, the metal ion impurities coming from raw phosphate rock play an important role as shape modifiers. The presence of impurities in the acid mixture has an impact both thermodynamically and kinetically, although most of the available literature focuses on their sole role as growth inhibitors and has neglected their potential impact on altering solution speciation.

Past studies on gypsum crystallization in phosphoric acid solutions usually involve the study of crystal growth and nucleation kinetics. However, most of these works did not use the correct definition of supersaturation when quantifying kinetic parameters. The high concentrations in this multicomponent electrolyte system implies that supersaturation, which be written in terms of the solubility product ratio, as governed by nonideal thermodynamics, requires the computation of activity coefficients as well as free ion concentrations. For this purpose, the mixed solvent electrolyte (MSE) model is utilized to capture the solution speciation in order to properly quantify supersaturation at any given condition. The MSE model is a first-principles model that determines solid-liquid equilibrium by calculating excess Gibbs energy from additive pairwise interactions. When impurities are present, additional binary interactions need to be included in the databank, which is carried out by regression analysis using solubility measurements.

Continuous reactive crystallization experiments are carried out with and without additives using a mixed-suspension, mixed-product removal (MSMPR) crystallizer. The crystal size distribution and supersaturation are measured once the pro-

cess reaches steady state. Different conditions are imposed to acquire both the temperature and supersaturation dependency of the crystallization kinetics. A two-dimensional growth model with dispersion is developed in order to capture the needle-like crystal morphology and the temperature dependence of the crystal aspect ratio, which is made possible by performing multi-scale image segmentation and edge detection using the Canny method. Experimental and numerical results are obtained for the base system and in the presence of single and combined impurity ions. Different growth inhibition models are verified and compared for numerical quantification of step advancement retardation in the presence of impurities.

This study goes beyond past studies by providing a full two-dimensional kinetic model for a highly concentrated ionic system that includes crystallization kinetics and a thermodynamically correct driving force accounting for non-ideality as well as the effects of impurities.

Thesis Supervisor: Allan S. Myerson
Title: Professor of the Practice of Chemical Engineering

Thesis Supervisor: Richard D. Braatz
Title: Edward R. Gilliland Professor in Chemical Engineering

Acknowledgments

I am extremely grateful for my Ph.D. advisors Allan Myerson and Richard Braatz for their continued support and guidance. I want to thank them for their consistent patience in listening to my ideas, and providing great feedbacks and suggestions in guiding me towards the right path to explore. They have been a great source of help when I am in need. I have learned so much in the past four years working under their guidance and I will be forever grateful. I would also like to thank my thesis committee members, Daniel Blankschtein, and James Swan, for their insightful comments and encouragement. They have given me great suggestions and support though the years.

I thoroughly enjoyed the many courses that I took during my graduate studies. I thank Martin Bazant and William Deen for teaching me transport phenomena, Arup Chakraborty and Brad Olsen for classical and statistical thermodynamics, Paul Barton and Joe Scott for numerical methods, George Stephanopoulos and Richard Braatz for systems engineering and control theory. I would also like to thank William Deen, Patrick Doyle, George Stephanopoulos and Richard Braatz for their support, advice, and patience while I was a teaching assistant for the undergraduate fluid mechanics and graduate systems engineering course.

Thanks my collaborator Zhilong Zhu. It has been a great pleasure working with him. We have had so many great discussions which are extremely helpful in guiding me with experimental designs and model improvement.

Thanks to the Myerson group members for their help throughout my PhD with special thanks to Chris Lai, who helped me started in the Myerson lab and introduced me to all the basic crystallization skills; to Yuqing Cui, who is always very patient in explaining and demonstrating equipment operation as well as pointing me to the right person for help; and to Naomi Brigges, who has helped me looking after my UROPs while I was away for maternity leave.

Thanks to the Braatz group members for their support and the fun they brought over the past five years with special thanks to Lucas Foguth, Eranda Harinath, Xiaoxiang Zhu, Lifang Zhou whom became really close friends with me (and my family)

and has given me great support when in need.

I gratefully acknowledge the funding agencies that have supported my work: the OCP group.

Lastly, I would like to thank my entire family for being a constant source of moral support. My biological parents Ping Han and Jun Peng have been the most important person in my life since I was born. They have always tried their best to provide me with the best opportunity they can in every aspect of life. Thanks to their extreme generosity, I had the chance to come here after I completed my undergraduate education in Singapore. They have constantly supported me in all my decisions and have shaped me into the person I am today with all the love, wisdom and encouragement they could offer. I could not thank them more. I would also like to offer my most heartfelt thanks and gratitude to my husband Joel Paulson who encouraged me to come back to MIT 4 years ago to pursue a PhD degree. Without his consistent support over the past four years, I would not have made it all the way to graduation and I would probably lost my one in a life chance to receive a doctor's degree. Most importantly, I would like to dedicate this thesis to my 6 months old son: Kai Anthony Paulson. He has been the most precious and adorable angel since he was born and he will continue to bring so much fun and joy to our life. He has given me so much courage in my final stage of PhD. I will always love him and try to be a role model for him. I hope one day he will get a chance to read this work.

Contents

THIS PAGE INTENTIONALLY LEFT BLANK

List of Figures

THIS PAGE INTENTIONALLY LEFT BLANK

List of Tables

Part I

Introduction

Chapter 1

Introduction

Growing Fertilizer Demand The global food demand is predicted to double in the next forty years due to the continuous increase in human population [57]. Particularly, the agricultural crops are the basic food supply and are consumed by almost every person on a daily basis. Today, the majority of phosphoric acid produced is converted to fertilizer which is essential for the growth of crops. Due to the increased agricultural demand, the fertilizer (essentially the phosphoric acid) production rate also needs to keep up. Hence, it is very important to maximize the phosphoric acid production efficiency in order to help meet this growing food demand. Being one of the world's largest phosphoric acid, as well as phosphate fertilizer manufacturers, it is of great interests to OCP to increase their current phosphoric acid production rate and process efficiency.

Industrial Phosphoric Acid Production About 90% of the world's phosphate consumption goes directly into the fertilizer industry[11], which is typically accomplished through converting the raw phosphate rock to phosphoric acid. Industrial phosphoric acid production makes use of the 'wet process,' which consist of two steps: (1) sulfuric acid attack of the ores, and (2) separation of the acid from the calcium sulfate hydrate crystals produced as a side product [11]. The main reaction involved

with raw phosphate rock can be written as [11]

$$\text{Phosphate Rock}(CaO, P_2O_5) + H_2SO_4 \rightarrow H_3PO_4 + CaSO_4 \cdot \underbrace{xH_2O}_{\text{hydrates}}$$

where x equals 0, 0.5, or 2 depending on temperature and acid concentration (see table 1.1). Since calcium sulfate hydrates have very small solubility even at relatively high temperature ($\sim$ 100 °C), they can be separated from the acid product this way. A phase diagram showing the stable regimes for each of the hydrate forms are presented in Figure 1-1[74].

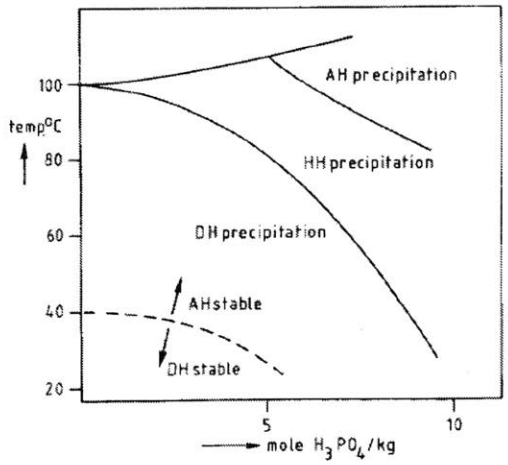

Figure 1-1: $CaSO_4$ hydrate precipitates as a function of the H_3PO_4 concentration and temperature of the solution. DH: dihydrate, $x = 2$; HH: hemihydrate, $x = 0.5$; AH: anhydrite, $x = 0$. Reprinted by permission from Elsevier [74], Copyright 1986.

Table 1.1: Process conditions for different calcium sulfate hydrate form produced from the wet process

x	Hydrate Form	Stability	Process Conditions		
			Temp.	Acid Conc.	P_2O_5 Recovery
2	Dihydrate	Metastable	70-80	Moderate	95-98%
0.5	Hemihydrate	Stable	80-90	Higher	<95%
0	Anhydrate	Stable	90-100	Highest	n/a

A number of different wet manufacturing processes have been developed in the

past, which can be summarized into two main categories: the dihydrate process ($x = 2$, gypsum as the final crystal form) and the nondihydrate process (also known as the hemihydrate process since hemihydrate is involved, although it is not necessarily the final crystal form). The dihydrate process is the earliest developed industrial phosphoric acid production technology. Despite its drawbacks, which include relatively low acid concentration (28–30% P_2O_5) and higher downstream energy consumption, the advantages such as no phosphate rock quality requirement, low operating temperature, infrequent maintenance, simple startup and shutdown operation, and easy scalability still makes the dihydrate process the most widely used technique.[11] Normally, this process will operate somewhere close to the equilibrium line to maximize the produced acid concentration at a given temperature without forming hemihydrates. We are interested in the dihydrate process as it is adopted by OCP in their chemical plants.

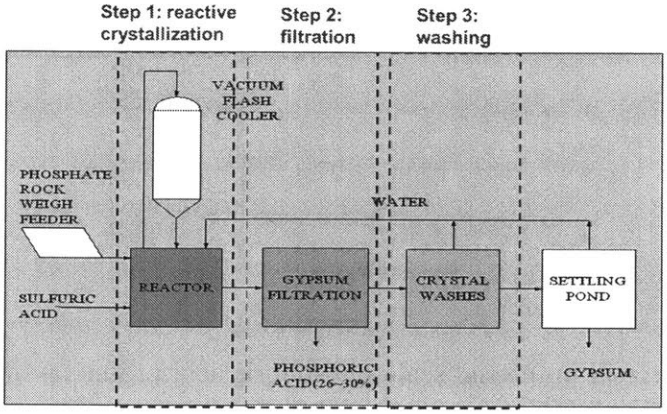

Figure 1-2: Overall phosphoric acid production process flow diagram. Reprint by permission from John Wiley and Sons Publisher [11], Copyright 1986 Verlag Chemie, GmbH.

The overall wet process is summarized in Figure 1-2 [11]. The phosphate rock and sulfuric acid are added continuously to the crystallizer (operates around 78 °C) with calcium sulfate dihydrate ($CaSO_4 \cdot 2H_2O$, Gypsum) formed as a side product under OCP's current process conditions. Although the reaction kinetics may vary depending on the quality and size of the rock, in general, the phosphate rock will reach 90% conversion within 1 minute. The slurry exiting the reactor is then feed to

a circular filtration unit with multiple stages to separate the gypsum crystals from the acid stream. At the same time, a less concentrated phosphoric acid stream ($\sim$ 17% P_2O_5) produced from the filtration unit is recycled back to the reactor. The final acid product from the filtration unit is around 28% P_2O_5 and it is further concentrated to about 56% P_2O_5 with additional treatment for impurity removal. A typical industrial mass flow from the dihydrate process is shown in figure 1-3.

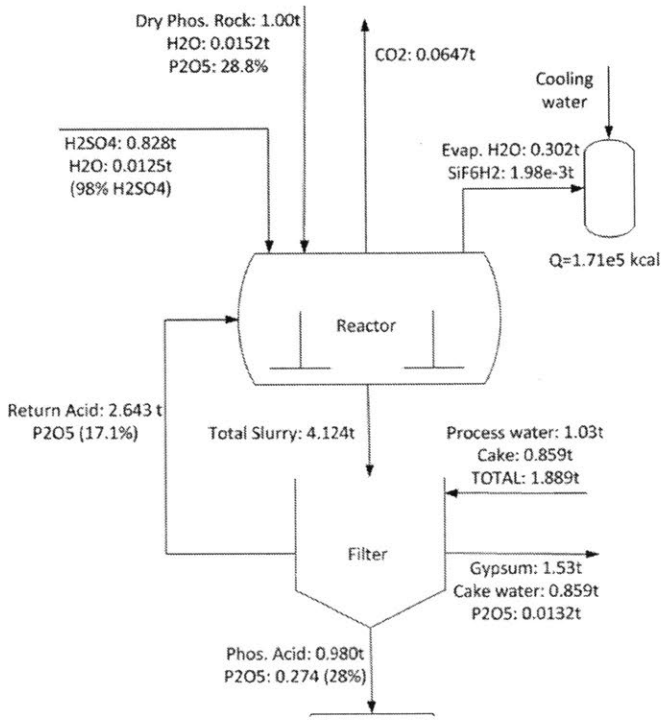

Figure 1-3: A typical industrial scale phosphoric acid production mass flow [11]

Immediately after the reactive crystallization step, filtration is carried out to separate acid from gypsum crystals. The overall productivity is closely correlated to the efficiency of the filtration step due to possible liquid entrainment in the gypsum crystals. This is determined by the gypsum crystal shape (Figure 1-4) and size distributions which are controlled by various factors such as acid concentration, process temperature, solid content, mixing/agitation and etc [11]. However, among all these factors, the impurities (i.e. Al^{3+}, Fe^{3+}, Mg^{3+}, organics) particularly the metal ions in the phosphate rock, also play an important role while their effects (especially quantitatively) have not been extensively studied or well understood. Figure 1-5 illustrates

visually the effect of additives on the morphology of gypsum crystals. Therefore, our work here focus on this particular step in the process and study the individual and combined effects of various impurities on the crystal habit and size distributions under the relevant system conditions.

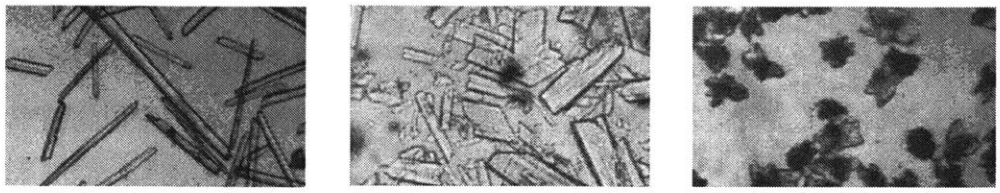

Figure 1-4: Examples of gypsum crystal shapes. From left to right: needle-like, plate, rhombic/cluster. Reprint by permission from John Wiley and Sons Publisher [11], Copyright 1984 Verlag Chemie, GmbH

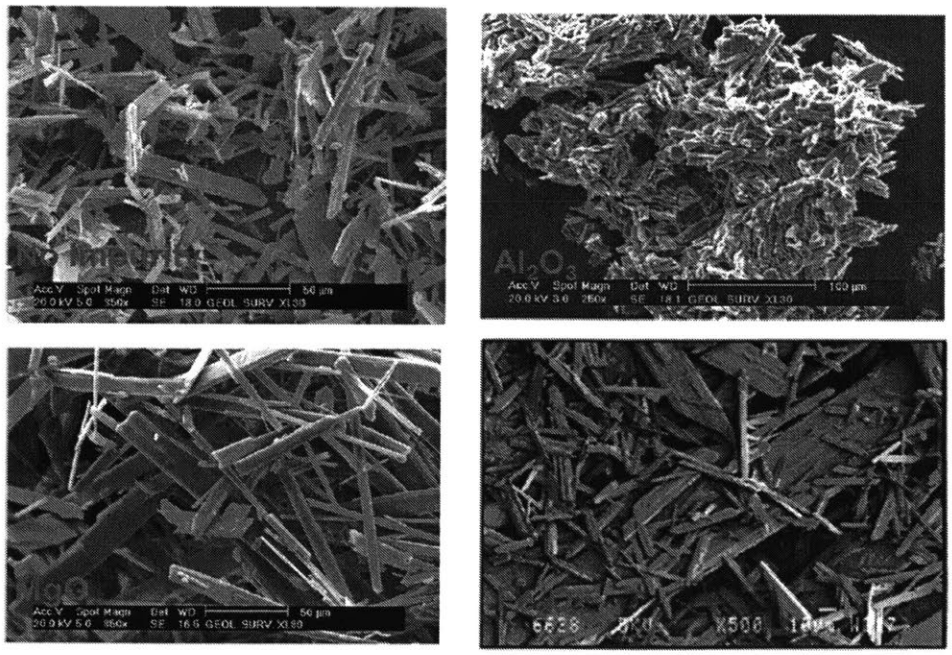

Figure 1-5: Examples of gypsum crystal shapes generated under the simulated phosphoric acid production conditions in the presence of impurity ions. Reprint by permission from Elsevier [61], Copyright 2004.

Thesis Overview The final objective of this work is to improve OCP's current production rate (namely the filtration rate) by implementing changes informed from

optimizing the current process. To achieve this, we hope to understand the role of impurities in modifying crystal shape and crystal size distribution (CSD) which directly influence the efficiency of the filtration process. This requires us to develop a model that can link the composition of impurities in the feed streams to the crystal shape and CSD at any given process conditions. The population balance model (PBM) is the conservation equation for the number of particles. Its mathematical framework enables the modeling of particle formation, growth, breakage, and aggregation. PBMs are widely used to model crystallization processes and is sufficient to serve our purpose in this work. Additionally, a filtration model that is able to relate filter cake resistance with particle shape and CSD is necessary to achieve the goal of process optimization. This is usually done through a combination of a series of models such as Darcy's law, Kozeny-Carmen relationship and the Packing model [75, 85, 40] or heuristics. We need to find out the ones that applies to our system. With these models completed, the overall process can be optimized to maximize filtration efficiency at a given feed/impurity composition (since there are fluctuations in the raw phosphate rock feed) by adjusting the relevant operating conditions. This work flow is summarized in the diagram below (Figure 1-6).

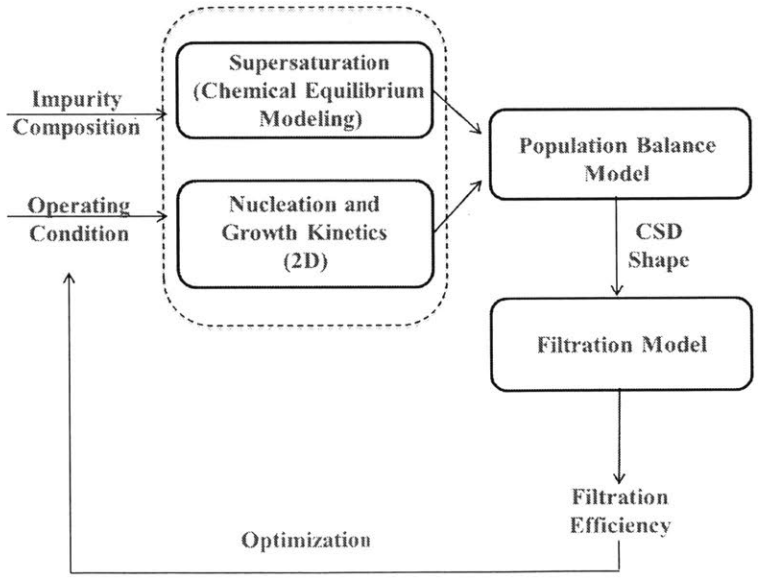

Figure 1-6: Thesis Work-flow

Past studies on gypsum crystallization in phosphoric acid solutions usually involve the study of crystal growth and nucleation kinetics. However, past works did not use the correct definition of supersaturation when fitting kinetic parameters. The high concentrations in this multicomponent electrolyte system implies that supersaturation which be written in terms of the solubility product ratio, as governing by nonideal thermodynamics, requires the computation of activity coefficients as well as free ion concentrations. For this purpose, the mixed solvent electrolyte (MSE) model is utilized to capture the solution speciation in order to properly quantify supersaturation at any given condition. The MSE model is a first-principles model that determines solid-liquid equilibrium by calculating excess Gibbs energy from additive pairwise interactions. When impurities are present, additional binary interactions need to be included in the databank, which is carried out by regression analysis using solubility measurements. This is done for all relevant impurity ions such as Mg^{2+}, Al^{3+}, Fe^{3+}, K^{+}, Na^{+}, etc.

Continuous reactive crystallization experiments are carried out with and without additives using a mixed-suspension, mixed-product removal (MSMPR) crystallizer. Crystal size distribution and supersaturation are measured once the process reaches steady state. Different conditions are imposed to acquire both the temperature and supersaturation dependency of the crystallization kinetics. One-dimensional growth model was first developed for temperature range from 25 to 60 °C. However, it was then found out to be unable to capture the increasing aspect ratio at even higher temperature. A two-dimensional growth model with dispersion is then developed in order to capture this needle-like crystal morphology and the varying crystal aspect ratio with temperature, which is made possible by performing multi-scale image segmentation and edge detection using the canny method. Experimental and numerical results are obtained for the base system and in the presence of single and combined impurity ions. Different growth inhibition models are verified and compared for numerical quantification of step advancement retardation in the presence of impurities.

Lastly, buchner funnel filtration experiments [50] are conducted to record the average filtrate rate for a given cake. Darcy's law is found to be valid here and hence

is used to compute cake permeability from the measured average filtrate rate. These results are then applied to study the relationship between gypsum cake resistance and its crystal size distributions. Most literature models indicates there is a linear relationship between the cake permeability and the square of the mean particle size which can be computed in various ways using the first, second and the third moment of the particle distribution. Here, we again make use of image analysis to measure the two dimensional size distribution for better accuracy in moment calculation. Models are compared based on their performance in fitting and the corresponding predictability of the cake resistance.

This study goes beyond past studies by providing a full two-dimensional population balance model for a highly concentrated ionic system that includes crystallization kinetics and thermodynamically correct driving force accounting non-ideality as well as the effects of an impurity. It also provides a foundation for future study, particularly in the aspect of understanding the effects of impurities on crystal growth and nucleation kinetics for inorganic systems in a multi-dimensional framework.

Part II

Chemical Equilibrium Modeling

THIS PAGE INTENTIONALLY LEFT BLANK

Chapter 2

Thermodynamic Framework

Previous studies on gypsum (or hemihydrate) crystallization in phosphoric acid solutions usually involve the study of crystal growth and nucleation kinetics.[80, 23] However, none of these works have used a correct definition of supersaturation when fitting experimental data to obtain kinetic parameters. The high concentrations in this multicomponent electrolyte system containing ions and hydrate crystals implies that using the total calcium or calcium sulfate concentration is inappropriate. A formal definition for supersaturation needs to be applied and the most intuitive and fundamentally correct way is to follow the thermodynamics, that is, make use of the solubility product ratio, which requires the calculation of activity coefficients as well as free ion concentrations. These calculations can be achieved by developing a proper model that is capable of performing speciation analysis for the system. For this purpose, this work employs a commercially available software platform with a well-established thermodynamic framework specifically targeted at electrolyte solutions.

2.1 Gypsum Solubility

Gypsum dissociates in the presence of aqueous solution and its solubility is governed by solid-liquid equilibrium with its dissociated ions and water molecule. Predicting gypsum solubility in the concentrated multicomponent electrolyte systems usually en-

countered in industrial processes can be challenging. Modeling electrolytes assuming complete dissociation can give comparable results for most simple dilute electrolyte systems, but this approach cannot handle the complicated solution chemistry in multicomponent electrolyte systems. Particularly, for this reactive crystallization system, the true species in solution phase are way beyond the added components (Figure 2-1). To reflect the actual solution chemistry, a speciation-based model is necessary so as to take into account chemical equilibria of all species including ionic, metal-ligand complexes, and undissociated species [6]. By performing speciation analysis, gypsum solubility can be computed by solving systems of nonlinear equations constrained by the chemical equilibria. The equilibrium constants can be evaluated from the standard state thermodynamic model.

$$Ca^{2+} + SO_4^{2-} + 2H_2O \leftrightharpoons CaSO_4 \cdot 2H_2O \tag{2.1}$$

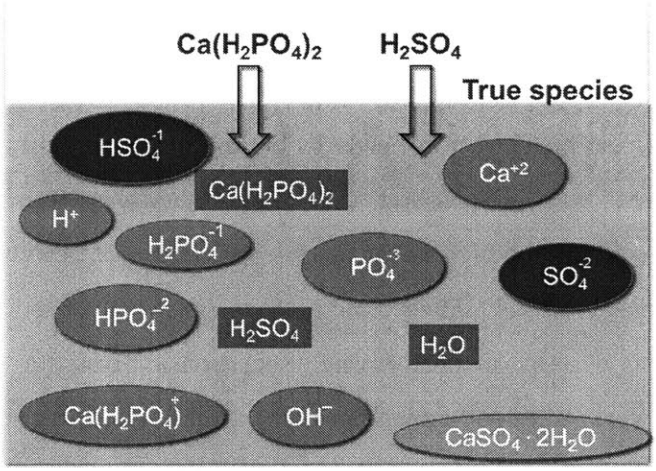

Figure 2-1: Graphic illustration of true species present in the solution phase during reactive crystallization of gypsum

For a concentrated electrolyte system, the ideal solution assumption is no longer valid due to the strong interactions between various species. Modeling of the solution's nonideality has been widely studied and reviews on these models are available.[44, 42] Many of the earlier published models can predict the nonideal behavior only up to a certain level of concentration. More recent development of thermodynamic mod-

els including the mixed solvent electrolyte (MSE) model [77] and electrolyte NRTL model [16] can account for solution nonideality for the entire concentration range from pure solvent to fused salt. It is important to distinguish the concept of speciation from nonideality. A model based on the complete dissociation assumption can still represent nonideal behavior. The MSE model [77] is a speciation-based model that has demonstrated accurate solubility prediction for gypsum systems [9, 10, 8] and many other electrolyte chemical systems [76]. This study makes use of the MSE model, which is available in the OLI software package, to account for the solution nonideality in characterizing gypsum solubility.

2.2 Mixed Solvent Electrolyte (MSE) model

The MSE model is a speciation-based model that determines phase equilibrium by performing speciation calculation while taking into account solution nonideality. The standard state computation in the MSE model relies on the Helgeson-Kirkham-Flowers (HKF)[63] model framework. In this framework, the standard state Gibbs energy (G^o) and any other partial molar properties are modeled based on 7 HKF parameters ($\omega, c_1, c_2, a_1, a_2, a_3, a_4$) as in

$$G^o = f(T, P; \omega, c_1, c_2, a_1, a_2, a_3, a_4) \tag{2.2}$$

where T is temperature and P is pressure. Knowing the standard-state Gibbs energy for all participating species in any equilibrium reaction (i.e., $aA+bB \leftrightarrows cC+dD$), the equilibrium constant (K_{eq}) can be determined at any given temperature and pressure:

$$K_{\text{eq}} = \exp\left(-\triangle G^o/RT\right) \tag{2.3}$$

$$\triangle G^o = \sum_i \nu_i G_i^o \tag{2.4}$$

where R is the gas constant and ν_i is the stoichiometric coefficient for species i.

The excess Gibbs energy, which describes the solution's nonideality, is modeled based on a combined framework of Debye-Huckle, Bromley, Pitzer, Zemaitis, and other contributors [78]. Typically, the nonideality of an electrolyte solution arises from various forces including the electrostatic (long-range), chemical, and physical dispersion forces.[78] While the electrostatic force is generally valid in dilute solutions, the latter two forces become dominant in concentrated solutions. In order to account for all these contributions, the excess Gibbs energy in the MSE model is calculated from

$$G^{ex} = G^{ex}_{LR} + G^{ex}_{II} + G^{ex}_{SR} \tag{2.5}$$

where G^{ex}_{LR} represents the contribution of long-range electrostatic interactions, G^{ex}_{II} accounts for specific ionic (ion-ion and ion-molecule) interactions, and G^{ex}_{SR} is the short-range contribution resulting from intermolecular interactions. The long-range interaction contribution is calculated from the Pitzer-Debye-Hückel formula[56] expressed in terms of mole fractions and is symmetrically normalized. This part of the excess gibbs free energy does not involve any fitting parameters.

$$\frac{G^{ex}_{LR}}{RT} = -(\sum_i n_i)\frac{4A_x I_x}{\rho}\ln(\frac{1+\rho I_x^{1/2}}{\sum_i x_i[1+\rho(I^0_{x,i})^{1/2}]}) \tag{2.6}$$

The short-range contribution G^{ex}_{SR} is calculated from the UNIQUAC equation[3] for mostly neutral-neutral interactions. Although most of the time, it is found that G^{ex}_{II} is better at describing molecule-molecule interactions. Therefore, $\tau_i j$ are normally not fitted.

$$\frac{G^{ex}_{SR}}{RT} = \frac{G^{ex}_{combinatorial}}{RT} + \frac{G^{ex}_{residual}}{RT} \tag{2.7}$$

$$\frac{G^{ex}_{combinatorial}}{RT} = (\sum_i n_i)[\sum_i x_i \ln\frac{\phi_i}{x_i} + \frac{Z}{2}\sum_i q_i x_i \ln\frac{\theta_i}{\phi_i}] \tag{2.8}$$

$$\frac{G^{ex}_{residual}}{RT} = -(\sum_i n_i)[\sum_i q_i x_i \ln(\sum_j \theta_j \tau_{ij})] \tag{2.9}$$

The specific ion-interaction contribution is calculated from an ionic strength-dependent, symmetrical second virial coefficient type expression [78]:

$$G_{II}^{ex} = -RT \sum_i n_i \sum_i \sum_j x_i x_j B_{ij}(I_x) \tag{2.10}$$

where n_i is number of mole of species i, x_i is the mole fraction of species i, B_{ij} is a binary interaction parameter between the species i and j, $B_{ij}(I_x) = B_{ji}(I_x)$, $B_{ii} = B_{jj} = 0$, and the ionic strength dependence of B_{ij} is given by

$$B_{ij}(I_x) = b_{ij} + c_{ij} \exp(-\sqrt{I_x + 0.01}) \tag{2.11}$$

where b_{ij} and c_{ij} are adjustable parameters. In general, the parameters b_{ij} and c_{ij} are functions of temperature with the form

$$b_{ij}(T) = b_{0,ij} + b_{1,ij}T + \frac{b_{2,ij}}{T} + \frac{b_{3,ij}}{T^2} + b_{4,ij} \ln T \tag{2.12}$$

$$c_{ij}(T) = c_{0,ij} + c_{1,ij}T + \frac{c_{2,ij}}{T} + \frac{c_{3,ij}}{T^2} + c_{4,ij} \ln T \tag{2.13}$$

where $b_{0-4,ij}$ and $c_{0-4,ij}$ are coefficients for each interaction pair.

The model equations are embedded in the software package by OLI Systems, Inc. together with some of the model parameters. The pre-existing data bank within the software platform includes interaction parameters that were obtained through extensive data collection and fitting done by OLI Systems, Inc. By comparing model predictions (with all available parameters taken from this pre-existing database) to literature data, possible missing ion-ion and ion-molecule interactions can be identified. The related interaction parameters as described in (2.12) and (2.13) were found through a similar regression study using available literature data such as solubility, heat capacity, and density. A variety of data is used in one single regression to ensure consistency of the model. All model parameters started with an initial value of zero. Sensitivity analysis was performed to select which model parameters to remove from further consideration and which to keep. Their parameter estimation algorithm uses

a series of iterations in which parameters that approach low sensitivity are then fixed and then no longer optimized. The parameter estimation algorithm, as implemented in OLI Systems, Inc., fixes model parameters that have a low sensitivity of the model predictions.

2.3 Supersaturation

Accurate estimation of the solution supersaturation is critical in the study of crystal growth and nucleation kinetics. The classical definition of supersaturation $\sigma = (c - c_{\text{eq}})/c_{\text{eq}}$ may not reflect the actual driving force for gypsum precipitation. A thermodynamically more appropriate definition uses the difference in chemical potential between supersaturated state and solid-liquid equilibrium state as σ.[47, 49] The general expression for the chemical potential of species i in the liquid phase is

$$\mu_i = \mu_i^o + RT\ln a_i \tag{2.14}$$

where μ_i^o is the standard chemical potential of species i, and a_i is the activity of species i, which is a product of its concentration c_i and activity coefficient γ_i. The theoretical dimensionless driving force for crystallization in the liquid phase is

$$\frac{\mu - \mu_{\text{eq}}}{RT} = \ln\left(\frac{\prod_{i=1} a_i^{\nu_i}}{\prod_{i=1} a_{i,\text{eq}}^{\nu_i}}\right) = \ln\left(\frac{\prod_{i=1} a_i^{\nu_i}}{K_{\text{sp}}}\right) \tag{2.15}$$

where $\mu = \sum \nu_i \mu_i$, and K_{sp} is the solubility product defined as the product of species activity at solid-liquid equilibrium. The relative supersaturation can be defined as

$$\sigma = \ln S = \ln\left(\frac{\prod_{i=1} a_i^{\nu_i}}{K_{\text{sp}}}\right) \tag{2.16}$$

where the supersaturation ratio S is the ratio between product of activity and the solubility product. This term is also referred to as scaling tendency in the OLI platform. This definition has been used in the evaluation of potassium chloride crystal growth rate.[17] The σ defined in (2.16) is also known as the *growth affinity* in some

literature.[82, 28] A per unit ion basis has also been seen in some literature to define the supersaturation ratio S' as in [84, 29]

$$S' = S^{\frac{1}{\nu^+ + \nu^-}} \tag{2.17}$$

where ν^+ and ν^- are stoichiometric coefficients of the positive and negative species. Another supersaturation expression includes the $\ln S \approx S - 1$ approximation, which is only valid at low supersaturation. The literature continues to use the approximate form of the supersaturation as it resembles the classical form of supersaturation found in the Burton-Cabera-Frank (BCF) model [52] for crystal growth. In this study, the gypsum supersaturation ratio (S) and relative supersaturation (σ) are defined as

$$S = \frac{a_{SO_4^{2-}} a_{Ca^{2+}} a_{H_2O}^2}{K_{sp,gypsum}} \tag{2.18}$$

$$\sigma = \ln S \tag{2.19}$$

The key in estimating the supersaturation in gypsum crystallization or precipitation in general is to have a model that can accurately predict the activity coefficients as well as the free ion concentration, which has been often neglected in the previous studies[43, 23] due to the complexity of its evaluation. The activity coefficient is often treated as constant, in which case the resulting "supersaturation" depends only on the species' concentration. Thermodynamic models such as the Pitzer model has been used in the estimation of gypsum supersaturation[82, 31] and the Bromley model has been used in the estimation of barium sulfate supersaturation,[79] both of which have application in only a limited concentration range. In this study, the state-of-art MSE model is utilized for calculating the activity coefficients and thus the relative supersaturation in the concentrated multicomponent electrolyte system.

2.4 Parameter Estimation

Generally in the study of crystallization kinetics, due to the direct influence of supersaturation on growth and nucleation kinetics, people always need certain way to quantify solubility at any given conditions. This usually involves work towards building certain model for solubility predication. Most of the time, they try to conduct series of solubility tests at all possible combinations of interested process conditions and then simply fit the experimental data into some functional form (i.e. polynomials) to achieve the above mentioned purpose. Even for our system, people have used such method before [67], but their results are limited to find only the solubility dependency on temperature and phosphoric acid concentration. The main drawbacks of this method is it requires a large set of experiments and the result can only be applied to the range where the solubility tests are conducted (extrapolation of the data is very unreliable). This becomes extremely problematic if we try to add impurity's effect. Also, such method only provides a way to find solubility which as we discussed above, does not provide real value in computing the properly derived supersaturation from basic thermodynamic driving force. Therefore, for our system, it is better to use the above mentioned MSE model that can evaluate solution speciation as well as ion activities at any given process conditions as long as the main interactions parameters are known. It also greatly reduced the number of experiments we need to conduct to collect data for modeling impurity's effects thanks to the model's additive principle.

Therefore, the goal is to find these missing interaction parameters that are relevant to the gypsum system. The following procedure is then proposed and carried out for parameter estimation purpose.

1. Determine the proper electrolyte system to study, for example, the base system for this case would be a mixture of $CaSO_4$, H_3PO_4, H_2SO_4 and H_2O.

2. Conduct extensive literature research to find solubility data for the targeting system (i.e. gypsum in phosphoric acid and sulfuric acid solutions) or any subsystems that contains the same set or a subset of electrolyte species of the targeting system. In the case where literature solubility is unavailable, slurry test

will be performed and solubility data will be collected experimentally through the measurement of total Ca, S, P and the corresponding impurity concentration using the Inductively Coupled Plasma (ICP).

3. Perform speciation analysis for the targeting system at all conditions to identify the dominant ions/molecules/complexes in the solution phase.

4. Checking the current OLI databank for existing pairwise interactions that are relevant to the targeting system.

5. Propose strong missing interactions between the identified dominant species.

6. Usually the collected dataset is divided into a training set (80% of the entire data set) and a validation set (remaining 20%) where the training set data is used to get a good estimate of the parameters at first. Then these estimates are used as an initial guess to continue the fitting by using all the data points. This two-step procedure is used to prevent over-fitting on the training set. Here over-fitting refers to a model that fits to the uncertainty/error in data which usually leads to a decreased power in prediction.

7. All model parameters for the proposed missing interaction pairs started with an initial value of zero when beging regressed. Sensitivity analysis was performed to select which model parameters to remove from further consideration and which to keep. The OLI parameter estimation algorithm uses a series of iterations in which parameters that approach low sensitivity are then fixed and then no longer optimized. The parameter estimation algorithm, as implemented in OLI Systems, Inc. are described in more details below.

8. For each pairwise interaction, up to $b_{4,ij}$ and $c_{4,ij}$ as described in (2.12) and (2.13) might be included. Most of the time, only a constant ($b_{0,ij}$ and $c_{0,ij}$) and a first order temperature dependency term ($b_{1,ij}$ and $c_{1,ij}$) are necessary.

9. The regression study completes for the targeting system when it shows good prediction on the validation data set. The regressed parameters will then be

added to the current databank.

10. Repeat the above steps when adding impurity's effect. The new targeting system should always be built upon the previously regressed parameters involving interactions that are relevant.

The proposed procedure is summarized in the following flow diagram (Figure 2-2).

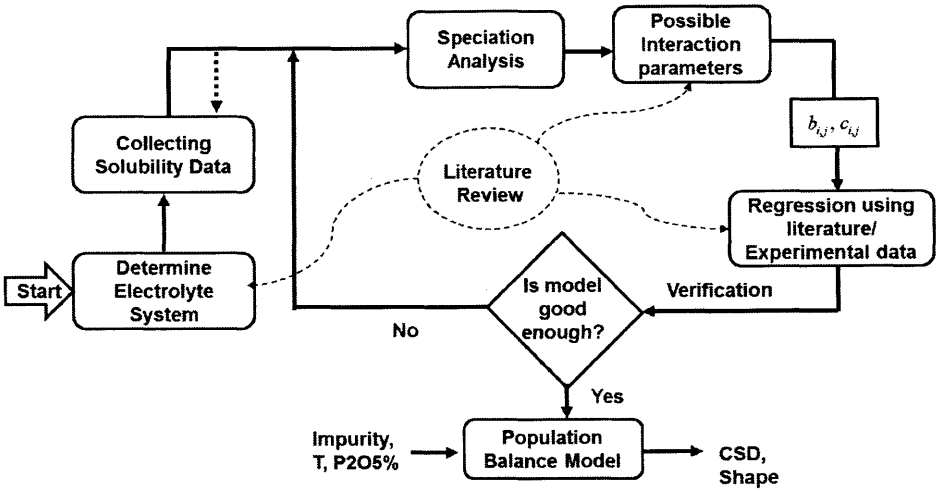

Figure 2-2: Graphic illustration of the proposed procedure to carry out regression study for missing interaction parameters

Estimation Algorithm We used the parameter estimation algorithm within OLI Systems, which treats the details of their algorithm as proprietary. The algorithm used for fitting the MSE parameters in the OLI software has been fairly extensively applied in journal literature that describes its application to various specific systems. As the details are proprietary, the best we can do is make some educated guesses on how their parameter estimation algorithm works, based on using their software and on our understanding of parameter estimation algorithms designed to reduce over-fitting. We started all model parameters with an initial value of zero. Sensitivity analysis was performed to select which model parameters are removed from further consideration and which to keep. Their parameter estimation algorithm uses a series of iterations

in which parameters that approach low sensitivity are then fixed and then no longer optimized. Although OLI Systems does not report their way of reducing the potential for over-fitting, it is reasonably likely that they use some standard regularization technique (very likely to be the two-norm ridge regression as some parameters will approach very small non-zero values during optimization), which is a method that is very easy to implement and well established in the literature. The combination of iterative pruning and regularization are well established and commonly applied in the literature. It is likely that the values of the model parameters are unlikely to be highly accurate. On the other hand, it is well established that regularization methods, especially when combined with pruning, tend to produce models with higher predictive accuracy for the estimation of a large number of parameters which matches our purpose here of making use of the MSE model for supersaturation computation.

THIS PAGE INTENTIONALLY LEFT BLANK

Chapter 3

Gypsum in Acid Mixtures

Initial analysis on the preloaded OLI data bank (MSEPUB data bank) showed that some of the critical interaction parameters of the base multicomponent system ($CaSO_4$ in H_3PO_4, H_2SO_4 and H_2O) had already been derived due to the fact that a variety of the subsystems (the related binary and ternary systems) has already been studied in the past (Table 3.1) by OLI Systems, Inc. This past work is very important as the additive principle of the MSE model enables property prediction of complex multicomponent systems using parameters obtained from studies of subsystems. Therefore, part of the main interaction parameters related to our system were already in the OLI data bank and only the missing parameters needed to be identified and estimated.

Table 3.1: Subsystems of $CaSO_4$-H_3PO_4-H_2SO_4-H_2O studied by OLI

Subsystem	CaO	$CaSO_4$	H_3PO_4	H_2SO_4	H_2O
1		✓			✓
2				✓	✓
3			✓		✓
4	✓		✓		✓

3.1 Gypsum in Phosphoric Acid

Literature data of $CaSO_4$ hydrates' solubility (all three forms) in phosphoric acid solutions at various temperatures [68, 69]were found at first. Observation of the

current OLI databank indicated that the only missing interactions were between the phosphate-related (PO_4^{3-}) species and the sulfate-related (SO_4^{2-}) species (ions or molecules). Detailed speciation analysis was performed using the OLI software and the most abundant species in this multicomponent system at all temperature and acid concentrations were identified to be: H_3PO_4, $H_2PO_4^-$, H_3O^+ and $CaSO_4$, in the following order:

$$H_3PO_4 > H_3O^+, H_2PO_4^- > CaSO_4 \tag{3.1}$$

Therefore the most intuitive pairwise interactions to be included is between $CaSO_4$ and the PO_4^{3-} related species, particularly, H_3PO_4 and $H_2PO_4^-$ as suggested from the speciation study. Further observations on the difference between the preliminary regressed OLI model prediction and the literature data indicated large deviation exists mainly at higher acid concentration. Particularly, P_2O_5 concentration changes significantly (by 10^6 times) from low to high acid concentration although it has been ignored first due to it's small absolute value from speciation analysis.

Interaction parameters between these most abundant species as described in (2.12) and (2.13) were estimated through regression analysis. The literature data used for parameter estimation are listed in Table 3.2. Solubility data of all three $CaSO_4$ hydrate forms were used since they share the exact same set of electrolyte species in solution form, which also ensured consistency and accuracy of the fitted model parameters. Some of the available interactions are slightly modified to help better shape the prediction curve (Table 3.4).

Table 3.2: Summary of literature solubility data used for estimating interaction parameters in the base OLI MSE model

Source	System	$CaSO_4$ hydrate form	Temperature range (°C)
Taperova, 1940 & 1945 [68, 69]	$CaSO_4$-P_2O_5 -H_2O	Dihydrate	25, 40, 60, 80
	$CaSO_4$-P_2O_5 -H_2O	Hemihydrate	25, 40, 60, 80
	$CaSO_4$-P_2O_5 -H_2O	Anhydrite	25, 40 60, 80

The major fitted interaction parameters included in the model are listed in Table 3.3. With these fitted model parameters, the calculated and literature experimental values of gypsum solubility in phosphoric acid solutions is shown in Figures 3-1. The plot indicates that the model fits the data set well for a wide range of temperatures (25°Cto 80°C) and acid concentrations. One thing to note is that although only the solubility plots for gypsum are shown here, the model is general for all three crystal forms.

Table 3.3: Major fitted interaction parameters included in the MSE model

Species i	Species j	b_{ij}	c_{ij}
$CaSO_4$	$H_2PO_4^-$	$b_{0,ij}$–$b_{4,ij}$	$c_{0,ij}$–$c_{4,ij}$
$CaSO_4$	H_3PO_4	$b_{0,ij}$–$b_{4,ij}$	$c_{0,ij}$–$c_{4,ij}$
$CaSO_4$	P_2O_5	$b_{0,ij}$–$b_{3,ij}$	$c_{0,ij}$–$c_{3,ij}$
$CaSO_4$	H_3O^+	$b_{0,ij}$–$b_{4,ij}$	$c_{0,ij}$–$c_{4,ij}$
H_3PO_4	P_2O_5	$b_{3,ij}$	$c_{3,ij}$
$H_2PO_4^-$	P_2O_5	–	$c_{3,ij}$

Table 3.4: Existing Pairwise Interactions that is Modified in the Pure System

Interaction Type	Species 1	Species 2
Neutral - Ion	$CaSO_4$	H_3O^+
Neutral - Neutral	P_2O_5	H_2O
Neutral - Ion	P_2O_5	H_3O^+
Neutral - Neutral	P_2O_5	H_3PO_4
Neutral - Ion	P_2O_5	$H_2PO_4^-$

3.2 Gypsum in Phosphoric and Sulfuric Acid Mixtures

However, the above regressed pairwise interactions does not show good model prediction for gypsum solubility in phosphoric acid with excess sulfuric acid [39]. This is because both the HSO_4^- and SO_4^{2-} ions become significantly important for the system with excess sulfuric acid and their interactions with the phosphate related

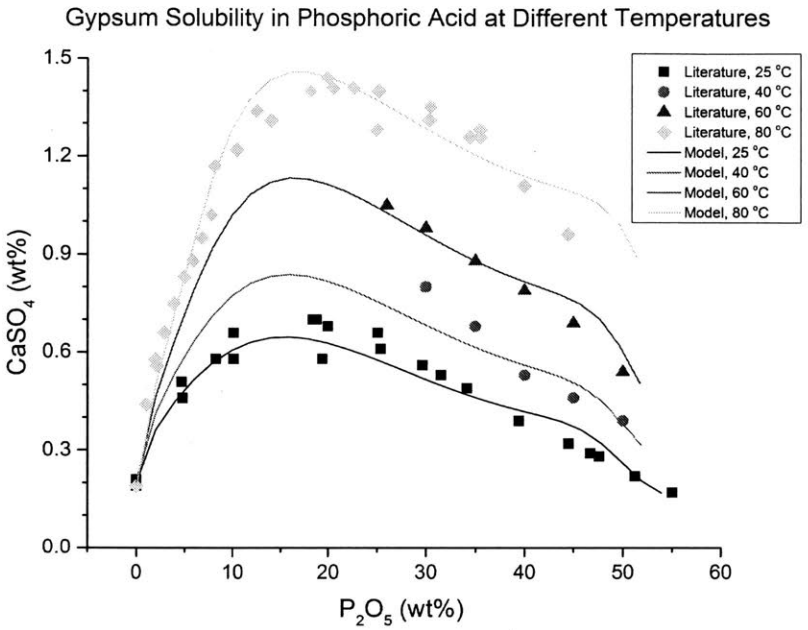

Figure 3-1: $CaSO_4 \cdot 2\,H_2O$ solubility as a function of phosphoric acid concentration at different temperatures. Points are literature experimental data.[68, 69] Curves are OLI model calculation.

species need to be considered as well. Therefore, new regression is performed with all the data combined to generate estimates for the modified set of interaction pairs.

Table 3.5: Additional literature solubility data used for estimating interaction parameters in the base OLI MSE model

Source	System	$CaSO_4$ hydrate form	Temperature range (°C)
Kurteva, 1961 [39]	$CaSO_4$-P_2O_5 H_2SO_4-H_2O	Dihydrate	25 50, 70
	$CaSO_4$-P_2O_5 H_2SO_4-H_2O	Hemihydrate	70
	$CaSO_4$-P_2O_5 H_2SO_4-H_2O	Anhydrite	70

The fitted interaction parameters included in the updated model are listed in Table 3.6. With these updated model parameters, the calculated values of gypsum solubility in acid mixtures matches well now with the literature experimental values as shown in figure 3-2.

The model was validated through comparing its predictions with experimental

Table 3.6: Fitted interaction parameters included in the MSE model

Species i	Species j	b_{ij}	c_{ij}
$CaSO_4$	$H_2PO_4^-$	$b_{0,ij}$–$b_{4,ij}$	$c_{0,ij}$–$c_{4,ij}$
$CaSO_4$	H_3PO_4	$b_{0,ij}$–$b_{4,ij}$	$c_{0,ij}$–$c_{4,ij}$
$CaSO_4$	P_2O_5	$b_{0,ij}$–$b_{3,ij}$	$c_{0,ij}$–$c_{3,ij}$
$CaSO_4$	H_3O^+	$b_{0,ij}$–$b_{4,ij}$	$c_{0,ij}$–$c_{4,ij}$
$CaSO_4$	$Ca(H_2PO_4)^+$	$b_{3,ij}$	$c_{3,ij}$
HSO_4^-	P_2O_5	$b_{2,ij}$,$b_{3,ij}$	$c_{2,ij}$,$c_{3,ij}$
HSO_4^-	H_3PO_4	$b_{0,ij}$,$b_{1,ij}$,$b_{3,ij}$	$c_{0,ij}$,$c_{1,ij}$,$c_{3,ij}$
HSO_4^-	$H_2PO_4^-$	$b_{3,ij}$	$c_{0,ij}$–$c_{4,ij}$
SO_4^{2-}	P_2O_5	$b_{3,ij}$	$c_{3,ij}$
SO_4^{2-}	H_3PO_4	–	$c_{1,ij}$, $c_{3,ij}$
SO_4^{2-}	$H_2PO_4^-$	$b_{3,ij}$	$c_{3,ij}$

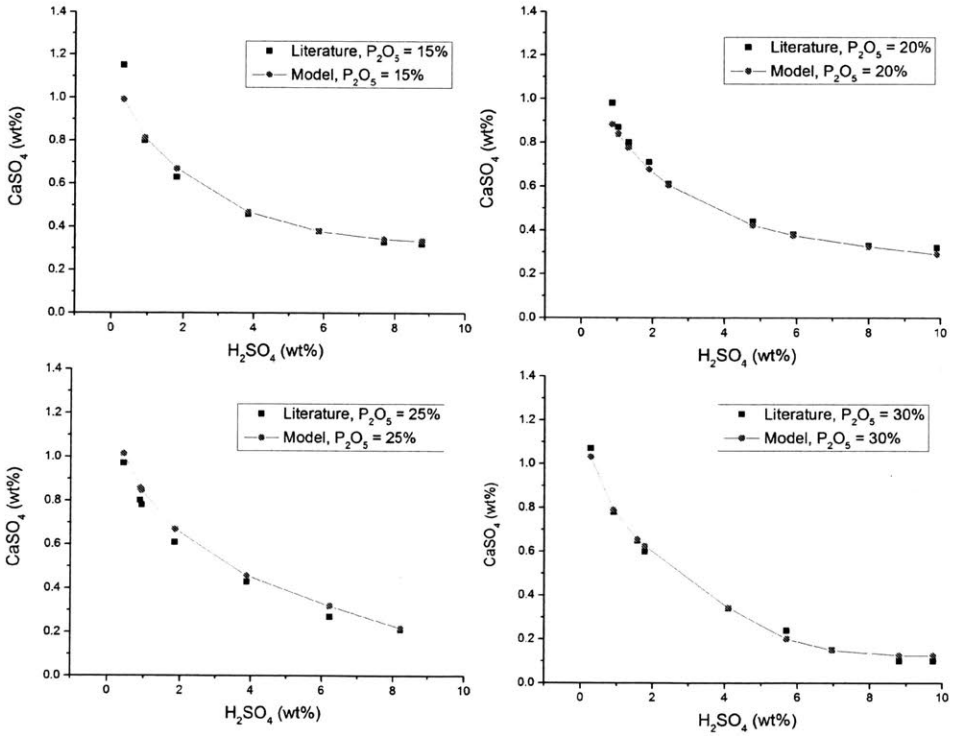

Figure 3-2: $CaSO_4 \cdot 2\,H_2O$ solubility as a function of sulfuric acid concentration at 70°C. Black points are literature experimental data.[39] Red points are OLI model calculation, with lines between the points used only to direct the eye.

values[67] of hemihydrate solubility in phosphoric acid solutions at 90°C. Results are plotted in Figure 3-3. It is clear from the verification plot that the MSE model predicts accurately the solubility of hemihydrate in the phosphoric acid solution using

the fitted interaction parameters at an extrapolated temperature (90°C), which also demonstrates its ability to handle a wide range of temperature and acid compositions. This model was then used throughout the study for computation of supersaturation at any given conditions.

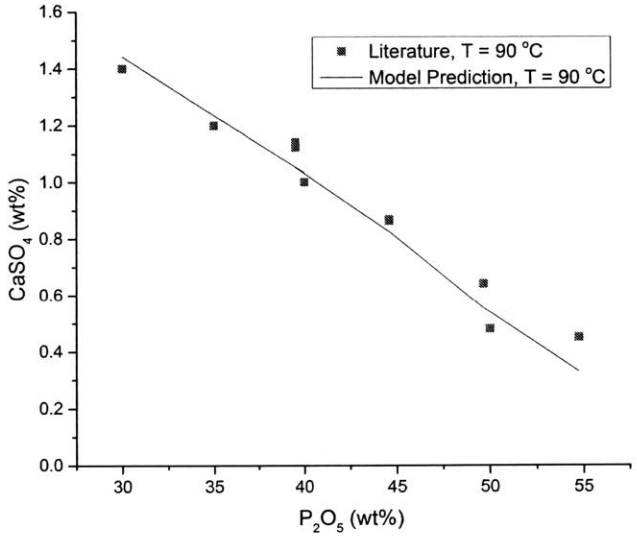

Figure 3-3: $CaSO_4 \cdot 0.5\,H_2O$ solubility as a function of phosphoric acid concentration at 90°C. Red points are literature experimental data[67]. Black line is OLI model prediction.

Chapter 4

Gypsum in Acid Mixtures with Impurity

Most of the literature work on impurity study for gypsum crystallization in phosphoric acid system involves only a qualitative result of the additive ions as shape modifiers [62, 27]. Some tried to quantify growth rates in the presence of these impurity ions [41] but did not provide any model or mechanism that describes the inhibition behavior at all conditions. Others tried to link its effect directly on cake filterability without looking into its impact on crystal size changes [35, 30]. These conclusions are thus not generalizable and provides very limited insights into impurity ions' effects. Most importantly, none of these studies tried to account for impurity's roles in both redistributing solution speciation and retarding growth rates. In this chapter, we describe the work done towards providing a method that quantifies the effects of impurity ions on modifying liquid phase supersaturation which is important for our later study on quantifying its blockage in kink site adsorption.

4.1 Existing Interactions

Before dig into the individual additive's effect on crystallization kinetics, it is important to first look into its impact on electrolytic speciation. A number of studies done in the past have ignored this thermodynamic effect directly without validation and in

most cases lead to improper conclusion on the impurity's growth inhibition behavior. To carry out this study, we first performed a detailed analysis on the existing interactions in the OLI databank. This mainly involves looking into previous studies done by OLI and going through their current databank to find relevant interactions between all the impurity ions we are interested and the base system. The results are shown in figure 4-1 where the red check marks indicates the presence of such interaction pairs (here the base system refers to the $CaSO_4$ - H_3PO_4 - H_2SO_4 - H_2O system).

Interactions in OLI databank.png

Species	Mg^{2+}	Al^{3+}	Fe^{3+}	K^+	Na^+	SiO_2	F^-	Base System
Mg^{2+}				✓	✓			
Al^{3+}					✓	✓		
Fe^{3+}				✓				
K^+					✓		✓	
Na^+						✓	✓	✓
SiO_2							✓	
F^-								✓

Figure 4-1: Existing interactions in the OLI databank between the ions that are relevant to our system

With this analysis, we aim to minimize solubility experiments to be carried out to fill the missing interactions. Here we have to collect our own data set as no literature data were found that involves such a complex system. Six sets of subsystems each with 2-4 different impurity ions were designed for solubility study. For each set, we collected solubility data at 4 different temperatures in the range of 25 to 80 °C, 10 various phosphoric acid concentration levels and 4-5 different impurity concentration combinations. This usually results in about 120-160 data points for training and an additional 40 data points for verification purpose. A final set involves all impurities (except silicone which we could not find one particular chemical that is able to dissolve when Al is present without introducing any foreign species) is also available to verify the overall consistency of the databank with all regressed interactions added together. These studies are summarized in figure 4-2 and the results from each data set is

discussed below. One thing to note, all regression studies carried out here are built upon the base system parameters and the original OLI databank.

Set #	System	Regression	Verification
1	Mg^{2+}– Base System	✓	✓
2	Al^{3+} – Base System	✓	✓
3	Fe^{3+} – Na^{+} – F^{-} – Base System	✓	✓
4	K^{+} – Al^{3+} – Base System	✓	✓
5	SiO_2 – Fe^{3+} – Mg^{2+}	✓	✓
6	Mg^{2+} – Al^{3+} – Fe^{3+} – F^{-}	✓	✓
7	Mg^{2+} – Al^{3+} – Fe^{3+} – K^{+} – Na^{+} – F^{-}	---	✓

Figure 4-2: Set of solubility experiments designed to complete the missing interactions for the complete system

4.2 Slurry Tests

Slurry tests were carried out to collect gypsum solubility data in phosphoric acid solution with the presence of impurity ions. Ten different phosphoric acid solutions with concentrations range from 5 wt% to 50 wt% P_2O_5 were prepared first. Magnesium oxide, aluminum nitrate nonahydrate, ferric phosphate dihydrate, monopotassium phosphate, sodium fluoride and fluosilicic acid were then dissolved in the acid solutions to introduce Mg^{2+}, Al^{3+}, Fe^{3+}, K^{+}, Na^{+}, F^{-} and Si to the system. Solutions are usually prepared with four to five different impurity levels. For example, the subsystem with only Mg^{2+} are prepared with MgO ranging from 0.1 wt% to 0.55 wt%. The details of the slurry tests' experimental conditions for each subsystem can be found in the following results section.

A hot plate with temperature control is used to heat up these solutions to a desired temperature. A reaction block is used to make sure all solutions with the same impurity concentration were heated up at the same time. Excess gypsum crystals were added to the acid solution to ensure there is more than the soluble amount.

Gypsum solids are mixed and stirred in the dissolved solution constantly throughout the entire experiment. Liquid samples are collected by filtering out the excess solids after at least 24 hours to make sure the solution system has reached equilibrium. Then the collected samples are diluted immediately for inductively coupled plasma (ICP) analysis to obtain accurate measurements of Ca, S, P and impurity element concentration. This is important as during the experiments, the acid concentration is likely to change due to possible evaporation especially at higher temperatures. The experiments were always carried out at 25, 40, 60 and 80 °C.

Materials For all experiments, reagent-grade calcium sulfate dihydrate ($CaSO_4 \cdot 2\,H_2O$), phosphoric acid (H_3PO_4, 85 wt%, 99.99 % trace metal basis), magnesium oxide (MgO), aluminum nitrate nonahydrate ($Al(NO_3)_3 \cdot 9\,H_2O$), ferric phosphate dihydrate ($FePO_4 \cdot 2\,H_2O$), monopotassium phosphate (KH_2PO_4), sodium fluoride (NaF) and fluosilicic acid (H_2SiF_6) were purchased from Sigma-Aldrich. Ultrapure water was used for solvent dilution.

4.3 Effect of Impurity Ions

4.3.1 Effect of Mg Impurity

Our experimental results suggest that the presence of Mg^{2+} does not affect gypsum solubility in phosphoric acid solution (Figure 4-3). Small variation in solubility is observed within up to 0.3 wt% of magnesium ion introduced to the system. Although no significant solubility effect was observed, the addition of Mg^{2+} ions to the multicomponent electrolyte solution always leads to alteration in the speciation. The clear deviation in gypsum scaling tendency with and without the presence of Mg^{2+} strongly supports this phenomena (Figure 4-4). The additive principle of the MSE model enables property prediction of complex multicomponent systems using parameters obtained from the studies of subsystems. Therefore, it is important that major interactions related to Mg^{2+} ions to be included in the MSE model databank in addition to the base system interactions. A summary of the solution conditions which

slurry tests were carried out can be found in table 4.1

Table 4.1: Experimental conditions for Mg^{2+} added slurry tests

Temperature (°C)	MgO (wt%)	P_2O_5 (wt%)
25, 40, 60, 80	0.1, 0.23, 0.3, 0.45, 0.55	5, 10, 12.5, 15, 20, 25, 30, 35, 40, 50

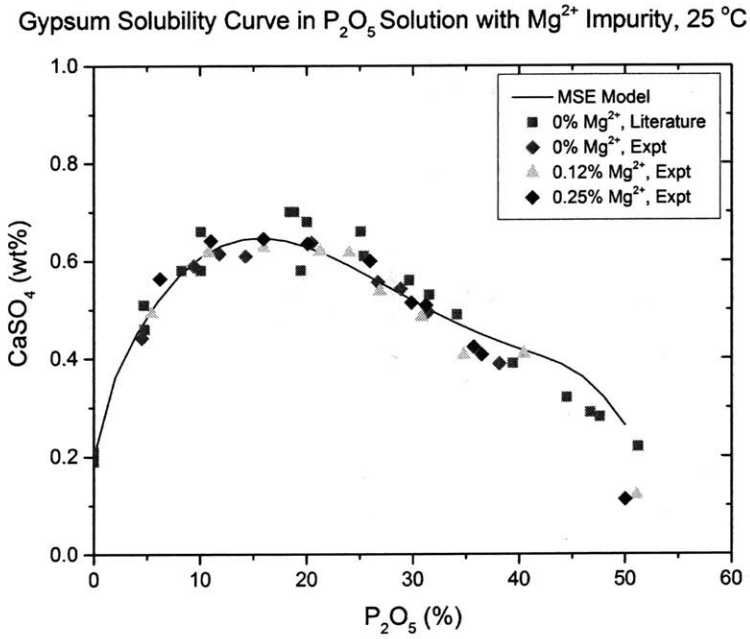

Figure 4-3: Gypsum solubility in phosphoric acid solution with magnesium impurity at 25 °C. Literature points are from Taperova (1945)[68, 69]. Curve is OLI model calculation for the base system.

Further observation indicated that the main missing interactions were between the phosphate -related species (ions or molecules) and Mg^{2+} ions. Detailed speciation analysis was performed using the OLI software, and the most abundant species for this subsystem were identified to be H_3PO_4, $H_2PO_4^-$, $CaSO_4$, $Ca(H_2PO_4)^+$ and Ca^{2+}. The interaction parameters between these species, as described in (2.12) and (2.13), were estimated through regression analysis. The slurry tests data were used for

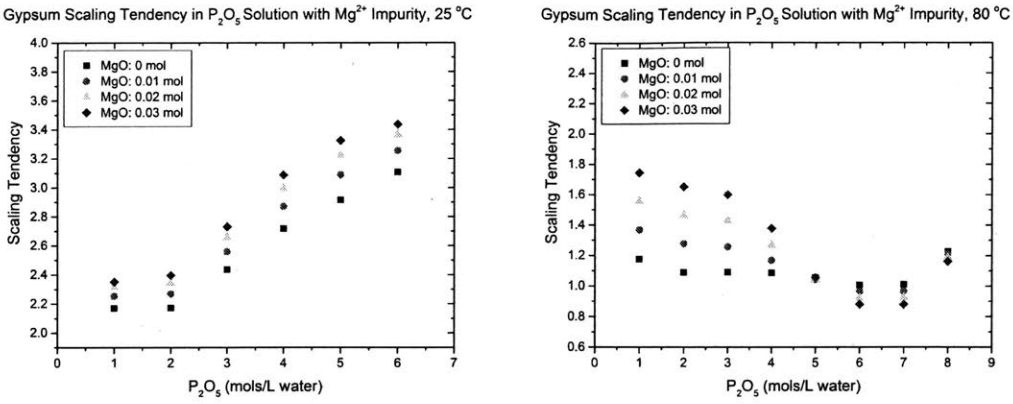

(a) 25 °C (b) 80 °C

Figure 4-4: Gypsum scaling tendency as a function of phosphoric acid concentration at various Mg^{2+} impurity levels

parameter estimation. The data set is divided into a training set (80% of the entire data set) and a validation set (remaining 20%) where the training set data is used to get a good estimate of the parameters at first. Then these estimates are used as an initial guess to continue the fitting by using all the data points. This two-step procedure is used to prevent over-fitting on the training set. Interactions between Mg^{2+} and P_2O_5 were also found to be important to ensure good fitting especially at high acid concentration.

The major fitted interaction parameters found regarding this subsystem are listed in Table 4.2. With these regressed parameters, the model was validated through a comparison of its predictions with experimental values collected in the presence of 0.18 wt% Mg^{2+}. Results are plotted in figure 4-5. It is clear from the verification plot that the current MSE model predicts accurately the solubility of gypsum for a large range of acid concentrations as well as temperatures with the presence of Mg^{2+} ions.

Now the regressed interaction pairs relevant to Mg^{2+} ions are included in the MSE model databank and it can be utilized for calculating saturation ratio when Mg^{2+} is present.

Table 4.2: Major fitted interaction parameters included in the MSE model relevant to Mg^{2+}

Species i	Species j	b_{ij}	c_{ij}
$Ca(H_2PO_4)^+$	Mg^{2+}	$b_{0,ij}$ - $b_{2,ij}$	$c_{0,ij}$ - $c_{2,ij}$
H_3PO_4	Mg^{2+}	$b_{0,ij}$ - $b_{2,ij}$	$c_{0,ij}$,$c_{2,ij}$
Ca^{2+}	Mg^{2+}	$b_{1,ij}$,$b_{2,ij}$	-
$H_2PO_4^-$	Mg^{2+}	$b_{0,ij}$ - $b_{2,ij}$	$c_{1,ij}$, $c_{2,ij}$
P_2O_5	Mg^{2+}	$b_{0,ij}$ - $b_{2,ij}$	$c_{1,ij}$, $c_{2,ij}$
$CaSO_4$	Mg^{2+}	$b_{0,ij}$ - $b_{2,ij}$	$c_{0,ij}$, $c_{1,ij}$

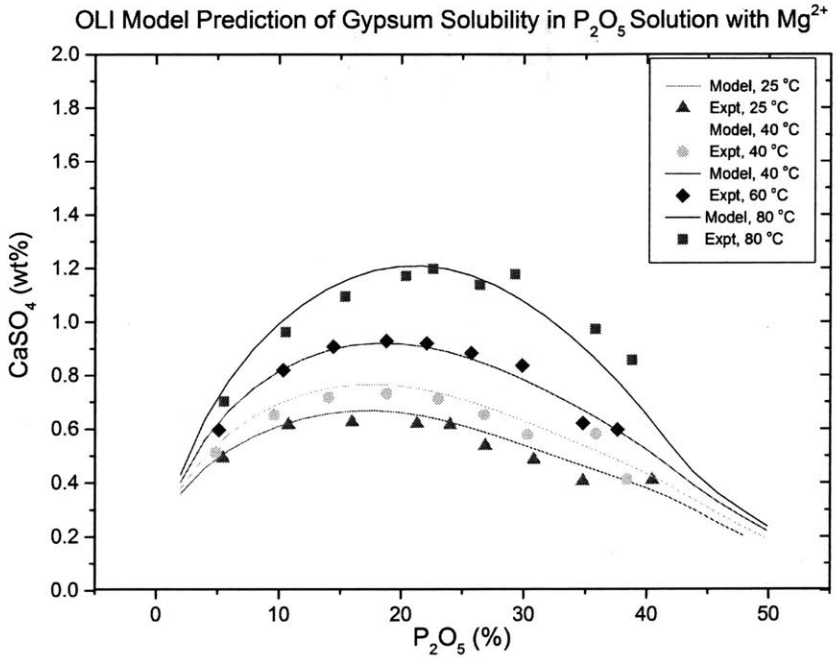

Figure 4-5: Model Prediction compared to experimental gypsum solubility measurements in phosphoric acid solution with the presence of 0.18 wt% Mg^{2+} from 25 to 80 ℃

4.3.2 Effect of Al^{3+} Ions

A similar study to that discussed above for Mg^{2+} is also carried out for Al^{3+} ions. Here we observed significant deviation in gypsum solubility with added Al^{3+} (figure 4-6, which is opposite to the behavior observed for added Mg^{2+}. Therefore, it is clear that additional pairwise interactions related to Al^{3+} ions need to be included in the MSE model databank. A summary of the solution conditions which slurry tests were carried out can be found in table 4.3

Table 4.3: Experimental conditions for Al^{3+} added slurry tests

Temperature (°C)	$Al(NO_3)_3 \cdot 9H_2O$ (wt%)	P_2O_5 (wt%)
25, 40, 60, 80	0.5, 1.5, 3.0, 4.5, 5.0	5, 10, 12.5, 15, 20, 25, 30, 35, 40, 50

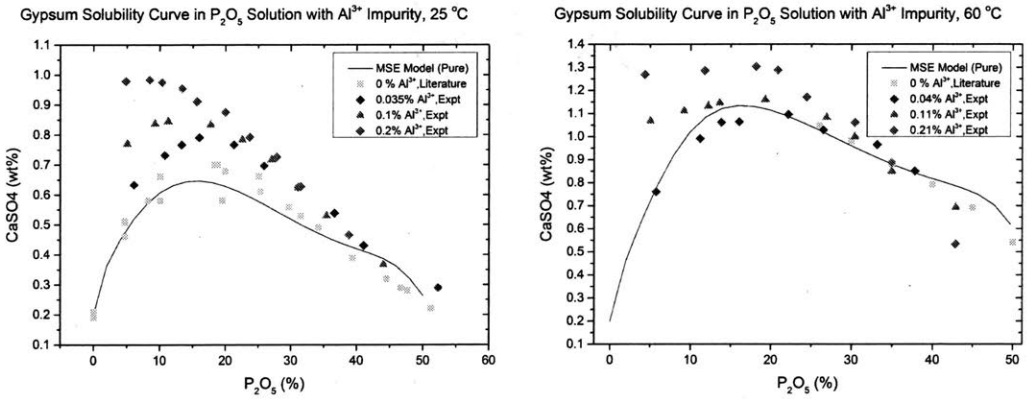

(a) 25 °C (b) 60 °C

Figure 4-6: Effect of Al^{3+} ion on gypsum solubility in phosphoric acid solutions. Literature points are from Taperova (1945)[68, 69]. Curve is OLI model calculation for the base system.

Further speciation analysis suggests for aluminum added system, $Al(SO_4)_2^-$ is also a dominant species in addition to Al^{3+}. As a result, its interactions with the major base system ions also needs to be included. Not to our surprise, the final interactions included involving $Al(SO_4)_2^-$ are mostly positive charged ions and neutral molecules while the ones involving Al^{3+} are negatively charged ions and neutral molecules. Again, their interactions with P_2O_5 are found to be important for better predication at high acid concentration. The regressed parameters are summarized in the table 4.4.

The resulting model prediction, using the regressed parameters is compared to a verification data set with the presence of 0.2 wt% Al^{3+}, and the results are shown in figure 4-7. The model fits and verifies the data well for a range of acid concentrations

Table 4.4: Major fitted interaction parameters included in the MSE model relevant to Al^{3+}

Species i	Species j	b_{ij}	c_{ij}
$H_2PO_4^-$	Al^{3+}	$b_{0,ij}$,$b_{1,ij}$	$c_{0,ij}$,$c_{1,ij}$
H_3PO_4	Al^{3+}	$b_{0,ij}$,$b_{1,ij}$	$c_{0,ij}$,$c_{1,ij}$
P_2O_5	Al^{3+}	$b_{0,ij}$,$b_{1,ij}$	$c_{0,ij}$,$c_{1,ij}$
H_3PO_4	$Al(SO_4)_2^-$	$b_{0,ij}$,$b_{1,ij}$	$c_{0,ij}$,$c_{1,ij}$
$Ca(HPO_4)^+$	$Al(SO_4)_2^-$	$b_{0,ij}$,$b_{1,ij}$	$c_{0,ij}$,$c_{1,ij}$
Ca^{2+}	$Al(SO_4)_2^-$	$b_{0,ij}$,$b_{1,ij}$	$c_{0,ij}$,$c_{1,ij}$
$CaSO_4$	$Al(SO_4)_2^-$	$b_{0,ij}$,$b_{1,ij}$	$c_{0,ij}$,$c_{1,ij}$
P_2O_5	$Al(SO_4)_2^-$	$b_{0,ij}$,$b_{1,ij}$	$c_{0,ij}$,$c_{1,ij}$

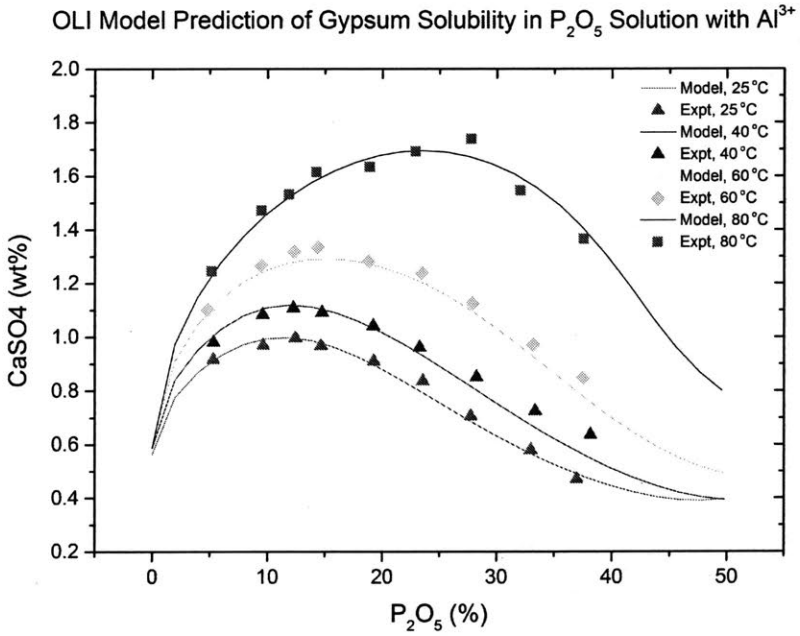

Figure 4-7: Model Prediction compared to experimental gypsum solubility measurements in phosphoric acid solution with the presence of 0.2 wt% Al^{3+} from 25 to 80 °C

and impurity levels. Now the regressed interaction pairs relevant to Al^{3+} ions are included in the MSE model databank and it can be utilized for calculating saturation ratio when Al^{3+} is present.

4.3.3 Effect of Al^{3+} and K^+ Ions

As we have discussed above, there already exists interactions between K^+ and most of the impurity ions. The only one that is missing is between it and the Al^{3+} related species. Therefore, we group these two impurity ions together in one subsystem to study the interaction of K^+ with the base system as well as Al^{3+} related species. However, this thus requires that we found Al^{3+}'s sole effect on the base system first. Therefore, this part of the regression study is carried out after the precious one is completed. A summary of the solution conditions which slurry tests were carried out can be found in table 4.5. The regressed parameters using collected solubility data are summarized in the table 4.6. Here, notice the interaction between K^+ and both Al^{3+} and $Al(SO_4)_2^-$ are included. Also, the interactions between K^+ and $CaSO_4$ and $H_2PO_4^-$ are not listed because they already exists in the original OLI databank.

Table 4.5: Experimental conditions for Al^{3+} and K^+ added slurry tests

Temperature (°C)	$Al(NO_3)_3 \cdot 9H_2O$ (wt%)	KH_2PO_4 (wt%)	P_2O_5 (wt%)
	0.75	0.25	5, 10, 12.5,
25, 40, 60,	1.8	0.65	15, 20, 25,
80	4.0	1.3	30, 35, 40,
	2.5	0.75	50

Table 4.6: Major fitted interaction parameters included in the MSE model relevant to Al^{3+} and K^+

Species i	Species j	b_{ij}	c_{ij}
$Ca(H_2PO_4)^+$	K^+	$b_{0,ij}$,$b_{1,ij}$	$c_{0,ij}$,$c_{1,ij}$
H_3PO_4	K^+	$b_{0,ij}$,$b_{1,ij}$	$c_{0,ij}$,$c_{1,ij}$
P_2O_5	K^+	$b_{0,ij}$,$b_{1,ij}$	$c_{0,ij}$,$c_{1,ij}$
HSO_4^-	K^+	$b_{0,ij}$,$b_{1,ij}$	$c_{0,ij}$,$c_{1,ij}$
Al^{3+}	K^+	$b_{0,ij}$,$b_{1,ij}$	$c_{0,ij}$,$c_{1,ij}$
$Al(SO_4)_2^-$	K^+	$b_{0,ij}$,$b_{1,ij}$	$c_{0,ij}$,$c_{1,ij}$

The resulting model prediction, using the regressed parameters is compared to the validation data set and the results are plotted in figure 4-8. The model fits the data well for a range of acid concentrations and impurity levels and the verification plot

shows reasonably good agreement between the measurement and the model prediction. Now the regressed interaction pairs relevant to K^+ and Al^{3+} ions are included in the MSE model databank and it can be utilized for calculating saturation ratio when both of these ions are present.

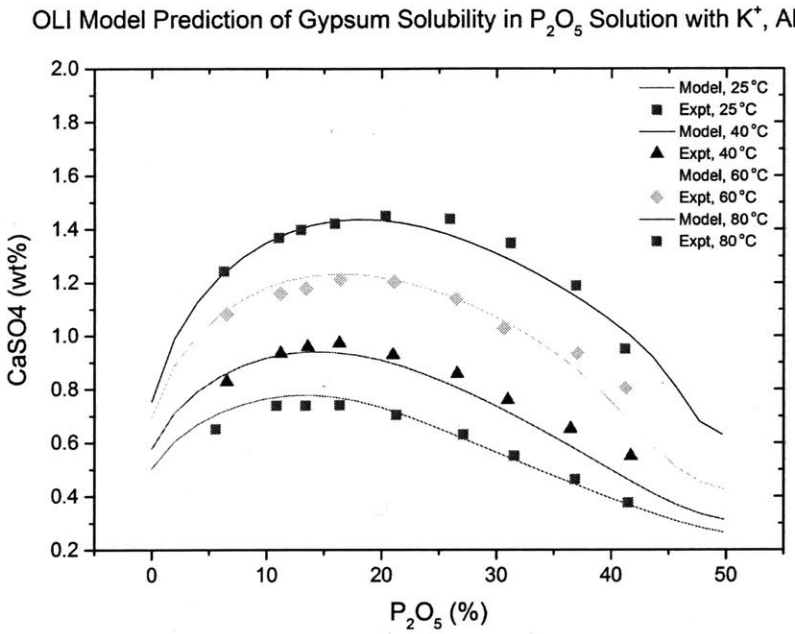

Figure 4-8: Model Prediction compared to experimental gypsum solubility measurements in phosphoric acid solution with the presence of 0.2 wt% Al^{3+} and 0.2 wt% K^+ from 25 to 80 °C

4.3.4 Effect of Fe^{3+} and Na^+ Ions

Similarly, we found that the interactions between Na^+ and most of the impurity ions are present and the only one missing is between it and the Fe^{3+} related species. Hence, we group these two impurity ions together in one subsystem to study the interaction of Fe^{3+} with the base system as well as Na^+. Na^+'s sole effect on the base system are already included in the original databank due to the extensive efforts OLI has put in the past in learning Na^+ interactions in all relevant subsystems of the base system. Therefore, this part of the regression study can be carried directly, building upon the base system study. A summary of the solution conditions which

slurry tests were carried out can be found in table 4.7. The regressed parameters using collected solubility data are summarized in the table 4.8. Here, notice the interaction between HF and H_3PO_4, $H_2PO_4^-$ and Ca^{2+} are also included. This is because F^- also enters the system when NaF completely dissociates in the solution phase and most of it forms the weak acid molecule HF. Some of its interactions with the phosphate-related species were found to be important and thus included in the parameter estimation. In addition, the interactions between Fe^{3+} and $CaSO_4$ and Ca^{2+} are not listed because they already exist in the original OLI databank.

Table 4.7: Experimental conditions for Fe^{3+} and Na^+ added slurry tests

Temperature (°C)	$FePO_4 \cdot 2H_2O$ (wt%)	NaF (wt%)	P_2O_5 (wt%)
	0.22	0.04	5, 10, 12.5,
25, 40, 60,	0.45	0.08	15, 20, 25,
80	0.90	0.15	30, 35, 40,
	0.65	0.10	50

Table 4.8: Major fitted interaction parameters included in the MSE model relevant to Fe^{3+}, Na^+ and F^-

Species i	Species j	b_{ij}	c_{ij}
$Ca(H_2PO_4)^+$	Fe^{3+}	$b_{0,ij}$ - $b_{2,ij}$	$c_{0,ij}$ - $c_{2,ij}$
H_3PO_4	Fe^{3+}	$b_{0,ij}$ - $b_{2,ij}$	$c_{0,ij}$,$c_{2,ij}$
Na^{2+}	Fe^{3+}	$b_{1,ij}$	$c_{1,ij}$
P_2O_5	Fe^{3+}	$b_{0,ij}$, $b_{1,ij}$	$c_{0,ij}$, $c_{1,ij}$
$H_2PO_4^-$	HF	$b_{0,ij}$, $b_{1,ij}$	$c_{0,ij}$, $c_{1,ij}$
H_3PO_4	HF	$b_{0,ij}$, $b_{1,ij}$	$c_{0,ij}$, $c_{1,ij}$
Ca^{2+}	HF	$b_{0,ij}$, $b_{1,ij}$	$c_{0,ij}$, $c_{1,ij}$

The resulting model prediction, using the regressed parameters is compared to the validation data and the results are shown in figure 4-9. The model fits the data well for a range of acid concentrations and impurity levels. The verification plot shows reasonably good agreement between the measurement and the model prediction. Now the regressed interaction pairs relevant to Na^+ and Fe^{3+} ions are included in the MSE model databank and it can be utilized for calculating saturation ratio when both of

these ions are present.

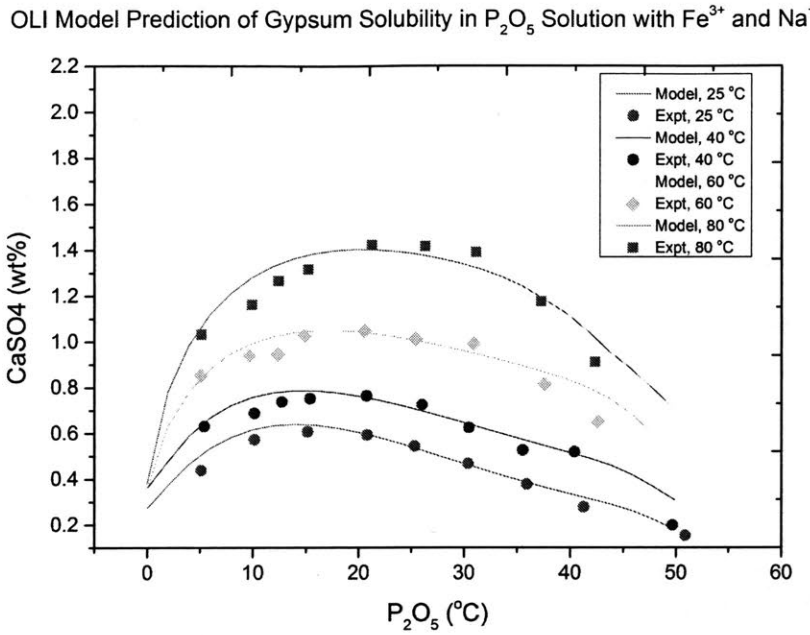

Figure 4-9: Model Prediction compared to experimental gypsum solubility measurements in phosphoric acid solution with the presence of 0.20 wt% Fe^{3+} and 0.05 wt% Na^+ from 25 to 80 °C

4.3.5 Effect of SiO_2, Fe^{3+} and Mg^{2+} Ions

Here we picked H_2SiF_6 to add silica impurity to our system without introducing any new ions. It is also the only chemical we found that was able to dissolved in this acid mixture to the extend that is similar to the industrial scale we were dealing with. $HSiF_6^-$ is thus found to be the dominant species involving silica in the solution phase. Again, we group it together with Fe^{3+} and Mg^{2+} ions in one subsystem since its interactions with the rest of the impurity ions are already present. Also, interactions between Fe^{3+} and Mg^{2+} are yet to be found. However, this thus requires that we found Fe^{3+} and Mg^{2+}'s sole effect on the base system first. Therefore, this part of the regression study is carried out after the preciously discussed ones are completed. A summary of the solution conditions which slurry tests were carried out can be found in table 4.9. Not to our surprise, interactions are included between all dominant species

in the base system and $HSiF_6^-$. The regressed parameters using collected solubility data are summarized in the table 4.10.

Table 4.9: Experimental conditions for Si, Fe^{3+} and Mg^{2+} added slurry tests

Temp. (°C)	$HSiF_6$ (wt%)	$FePO_4 \cdot 2H_2O$ (wt%)	MgO (wt%)	P_2O_5 (wt%)
	3.50	0.90	0.45	5, 10, 12.5,
25, 40, 60,	1.90	0.47	0.23	15, 20, 25,
80	0.45	0.25	0.09	30, 35, 40,
	0.95	0.60	0.15	50

Table 4.10: Major fitted interaction parameters included in the MSE model relevant to Si, Fe^{3+} and Mg^{2+}

Species i	Species j	b_{ij}	c_{ij}
H_3PO_4	$HSiF_6^-$	$b_{0,ij}$-$b_{2,ij}$	$c_{0,ij}$-$c_{2,ij}$
$Ca(H_2PO_4)^+$	$HSiF_6^-$	$b_{0,ij}$-$b_{2,ij}$	$c_{0,ij}$-$c_{2,ij}$
$H_2PO_4^-$	$HSiF_6^-$	$b_{0,ij}$-$b_{2,ij}$	$c_{0,ij}$-$c_{2,ij}$
$CaSO_4$	$HSiF_6^-$	$b_{0,ij}$-$b_{2,ij}$	$c_{0,ij}$-$c_{2,ij}$
P_2O_5	$HSiF_6^-$	$b_{0,ij}$-$b_{2,ij}$	$c_{0,ij}$-$c_{2,ij}$
H_2SO_4	$HSiF_6^-$	$b_{0,ij}$-$b_{2,ij}$	$c_{0,ij}$-$c_{2,ij}$
HSO_4^-	$HSiF_6^-$	$b_{0,ij}$-$b_{2,ij}$	$c_{0,ij}$-$c_{2,ij}$
SO_4^{2-}	$HSiF_6^-$	$b_{0,ij}$-$b_{2,ij}$	$c_{0,ij}$-$c_{2,ij}$
Mg^{2+}	$HSiF_6^-$	$b_{0,ij}$-$b_{2,ij}$	$c_{0,ij}$-$c_{2,ij}$
Fe^{3+}	$HSiF_6^-$	$b_{1,ij}$-$b_{2,ij}$	$c_{1,ij}$-$c_{2,ij}$
Mg^{2+}	Fe^{3+}	$b_{1,ij}$	$c_{1,ij}$

The resulting model prediction, using the regressed parameters is compared to the validation data and the results are shown in figure 4-10. The model fits the data well for a range of acid concentrations and impurity levels. The verification plot shows reasonably good agreement between the measurement and the model prediction. Now the regressed interaction pairs relevant to $HSiF_6^-$, Mg^{2+} and Fe^{3+} ions are included in the MSE model databank and it can be utilized for calculating saturation ratio when all of these ions are present.

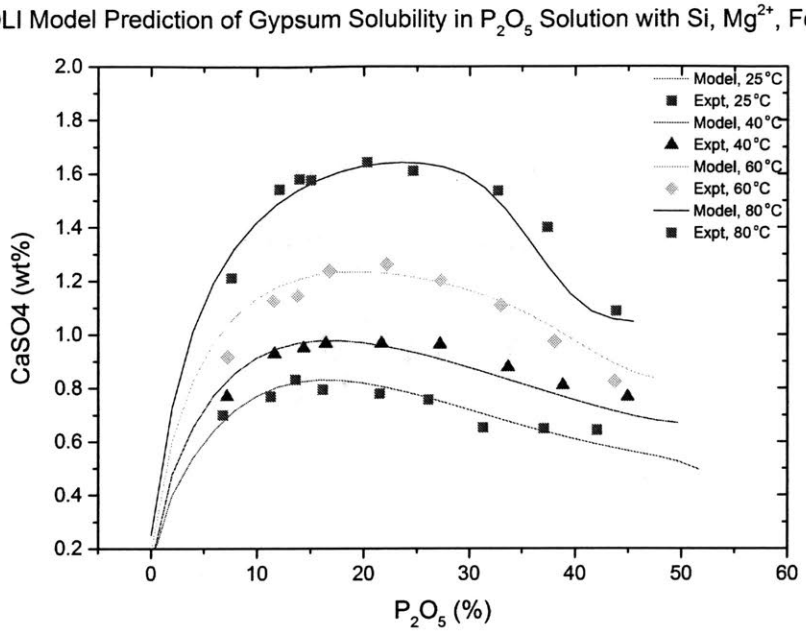

Figure 4-10: Model Prediction compared to experimental gypsum solubility measurements in phosphoric acid solution with the presence of 0.18 wt% Si, 0.18 wt% Fe^{3+} and 0.09 wt% Mg^{2+} from 25 to 80 °C

4.3.6 Effect of Mg^{2+}, Al^{3+}, Fe^{3+}, Na^{+} and F^{-} Ions

This is the last impurity subsystem we need to study before we fill the databank with all the strong missing interactions with respect to all impurity ions that appear in our system. A summary of the solution conditions which slurry tests were carried out can be found in table 4.11. During the study of this subsystem, we have encountered more difficulty than we expected due to the increased complexity in the system with the presence of both Al^{3+} and F^{-} ions. There are six different species in the form of $AlF_x^{(3-x)+}$ (x can be any number from 1 to 6) and the dominant species in the solution could be different depends on the total aluminum, fluoride concentration as well as the solution temperature and pH conditions [34]. Also, the presence of aluminium sulfate complex ($Al(SO_4)_2^{-}$) adds an additional level of complexity since it establishes new equilibrium with $AlF_x^{(3-x)+}$ complexes [34]. Based on our analysis, it is possible to have the following situations: 1)AlF_3 as the sole dominant species; 2)AlF_4^{-} as the sole dominant species; 3) AlF_4^{-} and Al^{3+} as the dominant species; 4)AlF_4^{-},$Al(SO_4)_2^{-}$

and Al^{3+} as the dominant species; 5)AlF_4^-,AlF_3 and Al^{3+} as the dominant species; 6)AlF_4^-,AlF_3, AlF_2^+ and Al^{3+} as the dominant species. Out of all the options, we found (2) gives the best performance in all cases. The regressed parameters using collected solubility data are summarized in the table 4.12.

Table 4.11: Experimental conditions for Mg^{2+}, Al^{3+}, Fe^{3+}, Na^+ and F^- added slurry tests

Temp. (°C)	MgO (wt%)	$Al(NO_3)_3 \cdot 9H_2O$ (wt%)	$FePO_4 \cdot 2H_2O$ (wt%)	NaF (wt%)	P_2O_5 (wt%)
25, 40, 60, 80	0.45	3.50	0.90	1.60	5, 10, 12.5, 15, 20, 25, 30, 35, 40, 50
	0.23	1.80	0.48	0.90	
	0.10	0.74	0.26	0.60	
	0.30	2.60	0.60	1.30	
	0.15	1.40	0.30	0.50	

Table 4.12: Major fitted interaction parameters included in the MSE model relevant to Mg^{2+}, Al^{3+}, Fe^{3+}, Na^+ and F^-

Species i	Species j	b_{ij}	c_{ij}
H_3PO_4	AlF_4^-	$b_{0,ij}$-$b_{1,ij}$	$c_{0,ij}$-$c_{1,ij}$
$Ca(H_2PO_4)^+$	AlF_4^-	$b_{0,ij}$-$b_{1,ij}$	$c_{0,ij}$-$c_{1,ij}$
$H_2PO_4^-$	AlF_4^-	$b_{0,ij}$-$b_{1,ij}$	$c_{0,ij}$-$c_{1,ij}$
$CaSO_4$	AlF_4^-	$b_{0,ij}$-$b_{1,ij}$	$c_{0,ij}$-$c_{1,ij}$
HSO_4^-	AlF_4^-	$b_{0,ij}$-$b_{1,ij}$	$c_{0,ij}$-$c_{1,ij}$
HF	AlF_4^-	$b_{0,ij}$-$b_{1,ij}$	$c_{0,ij}$-$c_{1,ij}$
F^-	AlF_4^-	$b_{0,ij}$-$b_{1,ij}$	$c_{0,ij}$-$c_{1,ij}$
Na^-	AlF_4^-	$b_{1,ij}$	$c_{1,ij}$
Mg^{2+}	Al^{3+}	$b_{1,ij}$	$c_{1,ij}$
Fe^{3+}	Al^{3+}	$b_{1,ij}$	$c_{1,ij}$
F^-	Al^{3+}	-	$c_{0,ij}$-$c_{1,ij}$
HF	Al^{3+}	$b_{0,ij}$-$b_{1,ij}$	-

The resulting model prediction, using the regressed parameters is compared to the validation data and the results are shown in figure 4-11. The model fits the data well for a range of acid concentrations and impurity levels. The verification plot shows reasonably good agreement between the measurement and the model prediction. Now

the regressed interaction pairs relevant to AlF_4^-, Mg^{2+}, Al^{3+}, HF and F^- ions are included in the MSE model databank and it can be utilized for calculating saturation ratio when all of these ions are present.

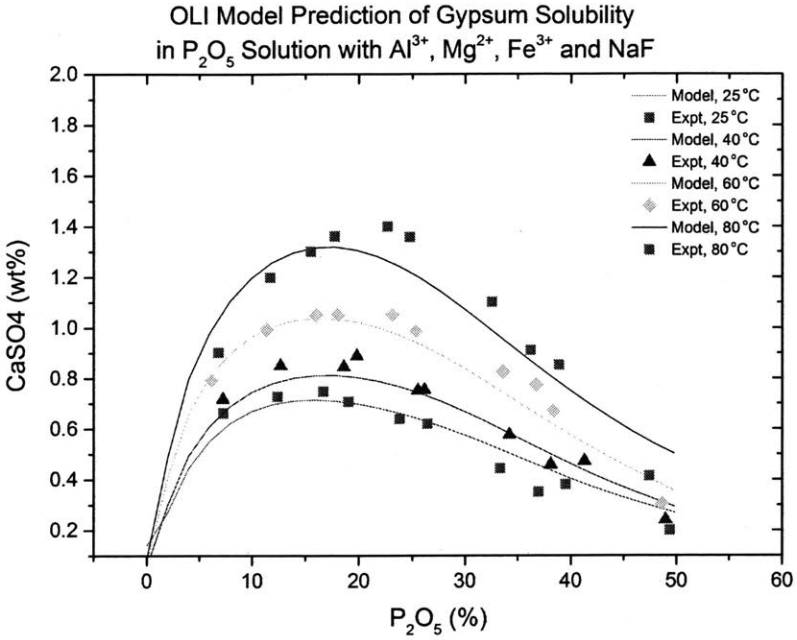

Figure 4-11: Model Prediction compared to experimental gypsum solubility measurements in phosphoric acid solution with the presence of 0.1 wt% Mg^{2+}, 0.11 wt% Al^{3+}, 0.09 wt% Fe^{3+}, 0.24 wt% Na^+ and 0.23 wt% F^- from 25 to 80 °C

4.4 Overall Verification

As a final step to check the overall consistency of the databank, we combined all fitted interaction parameters from above study and use that to predict gypsum solubility in phosphoric acid when all impurity ions are present.

The resulting model prediction, using the regressed parameters combined is compared to the validation data and the results are shown in figure 4-12. The verification plot shows reasonably good agreement between the measurement and the model prediction. This consolidated the MSE model framework and supported the additive principle of pairwise interactions. Now we have a model platform that can be utilized

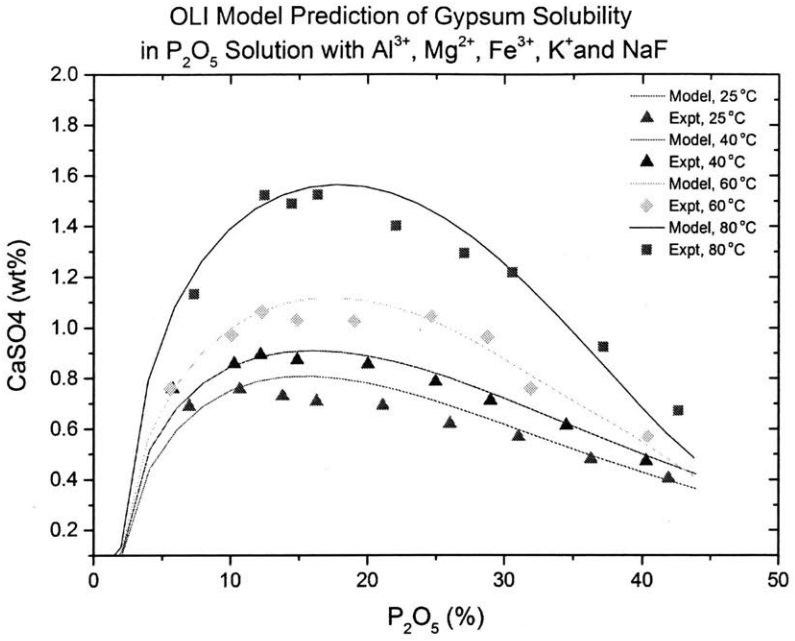

Figure 4-12: Model Prediction compared to experimental gypsum solubility measurements in phosphoric acid solution with the presence of 0.24 wt% Mg^{2+}, 0.07 wt% Al^{3+}, 0.09 wt% Fe^{3+}, 0.05 wt% K^+, 0.4 wt% Na^+ and 0.4 wt% F^- from 25 to 80 °C

for calculating saturation ratio when all of the impurity ions are present.

Part III

Crystal Growth and Nucleation Kinetics

THIS PAGE INTENTIONALLY LEFT BLANK

Chapter 5

Population Balance Modeling

The population balance model (PBM)[33, 60] is a conservation equation for the number of particles. Therefore, it is widely used to model particulate processes especially crystallization processes. Its mathematical framework enables the modeling of particle formation, growth, breakage, and aggregation. The vast majority of published crystallization models involve only a single independent characteristic length, which is limited to crystals of non-varying shape. The two-dimensional PBM has two characteristic lengths to describe the three-dimensional crystal structure, which is enough degrees of freedom for crystals that are produced from most crystallizing procedures (e.g., rods, needles, plates; in rare cases, three characteristic length scales would be needed). The extra length dimension allows the PBM to incorporate crystal shape information and simulate crystals of varying aspect ratio that would not be captured by a one dimensional model.

In order to make use of such model to describe particle size distribution in a reaction system, the crystal nucleation and growth kinetics are needed. In general, these kinetics can be described by semi-empirical power law equations and they are highly dependent on the solution phase supersaturation. Therefore, studying the kinetic parameters is a key step for using PBM in this study. With PBM implemented and linked to the thermodynamic model, which is built within the OLI software platform, crystal size distributions (CSDs) from this nonseeded reactive crystallization process can be predicted at any given operating conditions.

In this chapter, the theoretical background regarding crystallization kinetics as well as PBM will be reviewed. In addition, the methods we adopted in fitting kinetic parameters will be discussed. Both cases (1D and 2D) will be covered.

5.1 Crystal Kinetics

Crystallization kinetics describe crystal nucleation rate and growth rate from measurable states such as temperature and supersaturation in the crystallizer. Nucleation in a continuous system is dominated by secondary nucleation due to the large number of existing particles in the suspension. Therefore, its rate depends on the amount of crystals in the crystallizer. In the case of having only a single characteristic length, crystal growth and secondary nucleation kinetics are typically modeled by semi-empirical functions of supersaturation and temperature as in

$$G = k_g \sigma^g = k_g^{'} \exp\left(\frac{-E_g}{RT}\right) \sigma^g \tag{5.1}$$

$$B = k_b \sigma^b \mu_i^j \delta(L) = k_b^{'} \exp\left(\frac{-E_b}{RT}\right) \sigma^b \mu_i^j \delta(L) \tag{5.2}$$

$$B = B_0 \delta(L) \tag{5.3}$$

where k_g and k_b are temperature-dependent reaction constants that follow the Arrhenius form, E_g and E_b are activation energies. $\delta(L)$ is a Dirac delta function indicating that new crystals that are birthed have insignificantly small size. μ_i is the ith order moment where most of the time, $i = 2$ or 3. The second (μ_2) and the third-order moment (μ_3) is proportional to the total crystal surface area and volume per unit reaction volume receptively.

The power law relation is used in this work as it has been found to be able to describe nearly all reported experimental data[51]. The parameter j takes a value of either 1 or 2 that usually suggests the dominance of crystal–impeller collision ($j = 1$) or crystal–crystal collision ($j = 2$) in the secondary nucleation[73]. All of the main growth rate models have a supersaturation power dependency g between 1 and 2,

with many models having values of 1 or 2 in limiting cases[47]. For example, the diffusion–integration model has $g = 1$ if the growth rate is diffusion limited and $g = 1$ or 2 if it is surface integration limited. The Burton–Cabrera–Frank (BCF) model has $g_i = 1$ at high supersaturation and $g_i = 2$ at low supersaturation[13].

The model parameters can be estimated by fitting these semi-empirical equations against growth and secondary nucleation rates at different supersaturation and temperature levels. Such pairs of data can be obtained by performing continuous crystallization experiments until steady state when all measurable states remain constant. Growth rate information can be extracted from the steady-state CSD while the corresponding secondary nucleation rate can be calculated from the overall mass balance, as detailed in the next section.

When two characteristic lengths are present, a two-dimensional size-independent crystal growth and secondary nucleation kinetics are typically assumed to take place in the system. Similarly as described above, they can be modeled by semi-empirical functions of supersaturation and temperature in power law forms (5.4) - (5.6). It is a direct extension of the above 1D equations.

$$G_1 = k_{g_1}\sigma^{g_1} = k'_{g_1}\exp\left(\frac{-E_{g_1}}{RT}\right)\sigma^{g_1} \tag{5.4}$$

$$G_2 = k_{g_2}\sigma^{g_2} = k'_{g_2}\exp\left(\frac{-E_{g_2}}{RT}\right)\sigma^{g_2} \tag{5.5}$$

$$B = k_b\sigma^b\mu_{i,j}\delta(L_1)\delta(L_2) = k'_b\exp\left(\frac{-E_b}{RT}\right)\sigma^b\mu_{i,j}\delta(L_1)\delta(L_2) \tag{5.6}$$

$$B = B_0\delta(L_1)\delta(L_2) \tag{5.7}$$

where k_{g_1}, k_{g_2} and k_b are temperature-dependent reaction constants that follow the Arrhenius form, E_{g_1}, E_{g_2} and E_b are activation energies, and $\delta(L_1)$ and $\delta(L_2)$ are Dirac delta functions indicating that new crystals that are birthed have insignificantly small size. Particularly, cross-moment $\mu_{i,j}$ as defined in (5.8) are used in the nucleation

model ((5.6)) since two-dimensional size distribution information is available now.

$$\mu_{i,j} = \int_0^\infty \int_0^\infty f(L_1, L_2) L_1^i L_2^j \, \mathrm{d}L_1 \mathrm{d}L_2 \tag{5.8}$$

Most of the time, the second order moment $\mu_{1,1}$ which is proportional to the total crystal surface area, or the third-order moment $\mu_{1,2}$, which is proportional to the total volume of crystals in the crystallizer, could be used in (5.6). The nucleation model is typically dependent on the stirring rate, but is not included here as stirring was kept constant for all experiments. Again, both g_1 and g_2 should lie in between 1 and 2. Nucleation power b needs to be greater or equal to $\min(g_1, g_2)$ to make sure steady state slurry density is positive. In order to obtain estimates for these kinetic parameters, we propose to fit all the parameters simultaneously by minimizing the total sum of squared errors from all three rates weighted by its sample variance.

$$\theta = [k_{g_1}^{'}, k_{g_2}^{'} k_b^{'}, E_{g_1}, E_{g_2}, E_b, g_1, g_2, b] \tag{5.9}$$

$$\min_\theta \frac{1}{\sigma_{G_1,m}^2}(G_{1,m} - G_1)^2 + \sum_{G_{2,m}} \frac{1}{\sigma_{G_2,m}^2}(G_{2,m} - G_2)^2 + \sum_{G_1,G_2} \frac{1}{\sigma_{B,m}^2}(B_m - B)^2 \tag{5.10}$$

where $G_{1,m}$ and $G_{2,m}$ are the measured growth rates, $B_m = \frac{M_T}{6G_1G_2\tau^4}$ from mass balance using the predicted growth rates G_1 and G_2. $\sigma_{G_1,m}^2$, $\sigma_{G_2,m}^2$ and $\sigma_{B,m}^2$ are the corresponding sample variance for G_1 and G_2 and B. The method is found to be more robust to uncertainties in the data compared to the traditional method wherein each term is fit separately. This might due to the fact that the nucleation rate is a derived quantity. Therefore, this method is utilized in this work.

5.2 One Dimensional PBM Equation

The one-dimensional (1D) dynamic population balance equation (PBE) for a continuous crystallization process can be written as

$$\frac{\partial f(L,t)}{\partial t} + G(\sigma)\frac{\partial f(L,t)}{\partial L} = -\frac{f(L,t)}{\tau} + B \tag{5.11}$$

where $f(L,t)$ is the crystal number density distribution or number probability density function (pdf), t is time, L is crystal size/characteristic length. τ is the mean residence time of the reactor system, and it equals to $\frac{V}{Q}$, V is the reaction volume and Q is the total feed flowrate. Because the B term involves a Dirac delta function which only takes non-zero value at $L = 0$, it is easier to transform the above equation to the following one ((5.12)) with an additional boundary condition $f(0,t) = B_0/G$.

$$\frac{\partial f(L,t)}{\partial t} + G(\sigma)\frac{\partial f(L,t)}{\partial L} = -\frac{f(L,t)}{\tau} \tag{5.12}$$

The dynamic PBE (5.12) can be solved to obtain $f(L,t)$ for an initial condition given by the CSD of the seed crystals, $f(L,0) = f_{\text{seed}}$ and the boundary condition. The assumptions made to arrive at the PBE (5.12) are:

- Inlet streams contain no particles
- Reactants are well-mixed in the crystallizer
- Reaction volume remains constant
- Size-independent growth
- Nucleation and growth are dominant kinetic phenomena.

The assumption of size-independent growth has been experimentally observed to be true for most, but not all, crystallization systems. Uniform mixing can be easily achieved for small-scale bench experiments.

Since both the growth and secondary nucleation rates have a supersaturation dependency, which correlates directly with reactant concentration, the PBE must be solved together with its coupled mass balance equation:

$$\frac{dc_i}{dt} = \nu_i \rho k_v 3G \int_0^\infty f L^2 \mathrm{d}L + \frac{c_{\text{in},i} - c_i}{\tau} \tag{5.13}$$

where c_i is the concentration of species i in the crystallizer and the outlet stream, ν_i is the stoichiometric coefficient of the reaction, c_{in} is the inlet/feed concentration, ρ is crystal solid density, and k_v is crystal volume shape factor.

For our system, reactive crystallization takes place with two inlet streams. To handle this situation with PBM, the reaction time is assumed to be instantaneous, which is equivalent to feeding one highly supersaturated calcium sulfate solution. This assumption is made applicable here as ionic reactions are known to be fast and even in the industrial scale, we know 90% of the raw phosphate rocks dissolves in the strong sulfuric acid in the order of a few minutes. This is on a much smaller scale when comparing to the flow system residence time.

At steady state, all variables don't change with time any more. Therefore, letting $\frac{\partial f(L,t)}{\partial t} = 0$ in equation (5.12) transform the dynamic model to one that we can use to derive the steady-state analytic solution for such continuous process.

This transformed equation becomes:

$$G(\sigma)\frac{df(L,t)}{dL} = -\frac{f(L,t)}{\tau} \tag{5.14}$$

The above equation can then be easily solved to find the steady state analytical solution for $f(L)$. It is shown in (5.15) [60]. Here, we notice that the steady state size distribution does not depend on the seed crystal size distribution at all. This is because for continuous system, eventually all seed crystals get washed out of the system. Therefore, seeding won't affect the steady state result at all.

$$f_{\mathrm{ss}}(L) = \frac{B_0}{G}\exp\left(-\frac{L}{G\tau}\right) \tag{5.15}$$

Additionally, at steady state the crystallization agent concentration remain constant with time and this transform the dynamic mass balance equation (5.13) into the one below:

$$3\nu_i\rho k_v G\int_0^\infty f_{ss}(L)L^2\mathrm{d}L = \frac{c_{\mathrm{in},i} - c_{ss,i}}{\tau} \tag{5.16}$$

Solving the above equation can then generate the steady-state mass balance relationship. Then plug in the result for f_{ss} using equation (5.15), we can obtain the

below relations [60]:

$$c_{\text{in}} - c_{ss} = M_t \tag{5.17}$$

$$M_t = \rho k_v \mu_3 = 6\rho k_v \frac{B_0}{G}(G\tau)^4 \tag{5.18}$$

Where M_t is the slurry density. These equations are used to calculate nucleation rates at steady state from measured growth rates and concentrations.

Numerical Solution for Dynamic System: The Method of Characteristics

Several numerical approaches have been reported in the literature for solving dynamic PBEs[18, 4]. One of the most efficient and accurate numerical methods for solving PBEs is the method of characteristics (MOC). MOC has demonstrated to be efficient and highly resolved for solving PBEs for growth-dominant processes[59, 1]. It discovers curves along the L-t plane that transform the PBE (5.12) into ordinary differential equations:

$$\frac{dL_i}{dt} = G_i \tag{5.19}$$

$$\frac{df_i}{dt} = -\frac{f_i}{\tau} \tag{5.20}$$

$$\mu_k = \int_0^\infty f L^k \mathrm{d}L \approx \sum_i^N f_i L_i^k \Delta L_i \tag{5.21}$$

where the continuous size domain is evaluated at discrete points L_i, the population density evaluated at these points referred to as f_i, and the integral term in (5.21) was approximated by a summation. The solution to these system of ODEs gives the characteristic curves that propagate the size density information, which are used to construct the population density function at any given time. In the presence of nucleation, new characteristics are defined to account for the newborn nuclei. The boundary condition is imposed iteratively (every Δt) and the system of ODEs are solved simultaneously using *ode15s* in Matlab.

5.3 Two Dimensional PBM Equation

For crystals that takes up non-spherical shapes, we can assume that its morphology is represented by two characteristic lengths, L_1 and L_2, as shown in Figure5-1. With such approximations, the crystal surface area and volume can be calculated as

$$A_c = k_a(2L_1L_2 + L_2^2) \tag{5.22}$$

$$V_c = k_v L_1 L_2^2 \tag{5.23}$$

where k_a and k_v are the crystal surface and volume shape factor. Based on this simplification, A_c is proportional to $2\mu_{1,1} + \mu_{0,2}$ and V_c is proportional to $\mu_{1,2}$. Therefore, $2\mu_{1,1} + \mu_{0,2}$ or $\mu_{1,2}$ could be used in the nucleation rate equation (5.6). In the case of long needles where $L_1 \gg L_2$, surface area A_c would be proportional to a simplified $\mu_{1,1}$ term. That is why in most literature works, we often just see $\mu_{1,1}$ or $\mu_{1,2}$ in the nucleation rate equation.

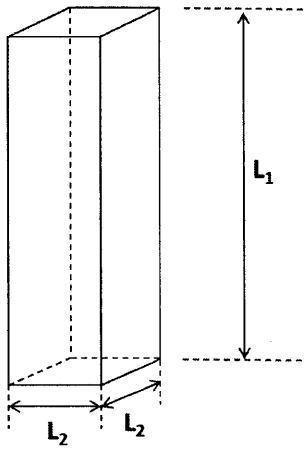

Figure 5-1: Two-dimensional approximation of crystal morphology for a hexagonal cross-section.

The two dimensional (2D) dynamic population balance equation (PBE) for a continuous crystallization process can be written as

$$\frac{\partial f(L_1, L_2, t)}{\partial t} + G_1 \frac{\partial f(L_1, L_2, t)}{\partial L_1} + G_2 \frac{\partial f(L_1, L_2, t)}{\partial L_2} = -\frac{f(L_1, L_2)}{\tau} + B \tag{5.24}$$

for describing size distribution changes for crystals with approximated 2D shape. The steady-state 2D population balance equation (PBE) for an MSMPR is

$$G_1 \frac{\partial f(L_1, L_2)}{\partial L_1} + G_2 \frac{\partial f(L_1, L_2)}{\partial L_2} = -\frac{f(L_1, L_2)}{\tau} + B_0 \delta(L_1)\delta(L_2) \tag{5.25}$$

where $f(L_1, L_2)$ is the steady-state 2D population number density, G_i is the crystal growth rate in the i dimension, τ is the residence time, B_0 is the nucleation rate, δ is the Dirac delta function.

An analytical solution to the steady-state 2D PBE (5.25) was reported by Klein et al. [58], but the reported analytical solution had a non-zero number density along the L_1 and L_2 axes, which cannot occur experimentally. Newborn crystals can only originate at $(0, 0)$ theoretically as defined by the product of two Dirac δ functions in the source term in (5.25). Therefore, for the 2D case, only numerical approach can be used to properly handle the nucleation term in order to find the steady-state 2D size distribution solution.

The MOC for handling both growth and nucleation in a multidimensional PBM for a crystallization process has not yet been reported in the literature. An approach for solving the 2D PBE (5.25) by MOC is to convert the nucleation at the origin to its equivalent boundary condition and the 2D PBE becomes

$$G_1 \frac{\partial f(L_1, L_2)}{\partial L_1} + G_2 \frac{\partial f(L_1, L_2)}{\partial L_2} = -\frac{f(L_1, L_2)}{\tau} \tag{5.26}$$

If we integrate equation (5.26) with respect to either L_1 or L_2, we find it reduces to the 1D PBM and therefore, we know the steady state solution for the marginalized distribution for each dimension is the same as the 1D analytical solution shown in equation (5.15). The resulting solution can be found in equation (5.27).

$$f_{\mathrm{ss},1}(L_1) = \int_0^\infty f_{ss}(L_1, L_2)\mathrm{d}L_2 = \frac{B_0}{G_1} \exp\left(-\frac{L}{G_1\tau}\right) \tag{5.27}$$

$$f_{\mathrm{ss},2}(L_2) = \int_0^\infty f_{ss}(L_1, L_2)\mathrm{d}L_1 = \frac{B_0}{G_2} \exp\left(-\frac{L}{G_2\tau}\right) \tag{5.28}$$

The equivalent boundary condition for the 2D case for the marginalized distribution then becomes

$$f_1(L_1) = \frac{B_0}{G_1} \tag{5.29}$$

$$f_2(L_2) = \frac{B_0}{G_2} \tag{5.30}$$

Additionally, mass balance equation at steady state for the 2D case becomes:

$$\rho k_v G \int_0^\infty \int_0^\infty f_{ss}(L_1, L_2) L_1 L_2^2 \mathrm{d}L_1 \mathrm{d}L_2 = \frac{c_{\mathrm{in},i} - c_{ss,i}}{\tau} \tag{5.31}$$

Solving the above equation can then generate the steady-state mass balance relationship. Then using the result for $f_{1,ss}$ and $f_{2,ss}$ shown in equation (5.27) and (5.28), we can obtain the below relations:

$$c_{\mathrm{in}} - c_{ss} = M_t \tag{5.32}$$

$$M_t = \rho k_v \mu_{1,2} = 6 \rho k_v B_0 G_1 G_2^2 \tau^4 \tag{5.33}$$

These equations are used to calculate nucleation rates at steady state from measured growth rates and concentrations.

5.4 Integration with OLI software

The functionality of the OLI software is made possible in other programming environments by OLI Engine 8.2, which is a collection of libraries that enables access to the OLI equilibrium calculation. Access to OLI functionality was implemented in an Excel Macro based on an example file provided by the OLI Systems, Inc. Since the MOC is solved in the Matlab environment, these Excel Macros were used as an intermediate that passes liquid-phase composition from the Matlab program to OLI Engine. Once a calculation is triggered, the OLI engine returns speciation and supersaturation value back to the Matlab program. To reduce the number of OLI Engine function calls, the equilibrium computation is only triggered when there is a

significant (0.1%) change in the amount of gypsum crystallized. This integration is done by my collaborator and the details of this work could be found in his thesis.

THIS PAGE INTENTIONALLY LEFT BLANK

Chapter 6

One Growth Dimension Kinetic Model

The use of population balance model requires the knowledge of crystallization kinetics. Reaction kinetics can be studied using either a batch or a mixed-suspension, mixed-product removal (MSMPR) reactor. However, since our target system in the industrial scale is carried out in a continuous fashion, it is be better to use MSMPR in this case to replicate the process. Also, using MSMPR for kinetic study ensures more accurate measurement of operating conditions since all variables are constant at steady state. The most common way to obtain kinetic parameters is to run the MSMPR crystallizer until it reaches steady state (s.s). Then we need to collect and measure the liquid sample for quantifying supersaturation and solid sample for their size distribution, $f_{measured}(L)$. Continuous reactive crystallization experiments needs to be carried out at different operating conditions to acquire both the temperature and supersaturation dependency of the crystallization kinetics. In this chapter, we will discuss the experiments performed and the corresponding results obtained when we assume only one characteristic length is sufficient for describing gypsum crystal growth.

6.1 Continuous Crystallization Experiments

Materials For all experiments, reagent-grade calcium phosphate dibasic $CaHPO_4$, sulfuric acid H_2SO_4 (96 wt%), phosphoric acid H_3PO_4 (85 wt%, 99.99 % trace metal basis) were purchased from Sigma-Aldrich. Ultrapure water was used for solvent dilution. A couple of choices such as $CaHPO_4$ [2, 61] and $Ca(H_2PO_4)_2$ [74, 5] can be used to model raw phosphate rock and the choice should not affect the kinetic study results.

Experimental Setup Figure 6-1 is a schematic diagram of the experimental setup designed to simulate the wet phosphoric acid production process. Two feed streams consisting of calcium phosphate dibasic and sulfuric acid respectively were pumped continuously to a 50-ml glass-jacked crystallizer. Overhead mechanical agitation was used to ensure good mixing of the reactants and the reaction volume was maintained at a constant value by fixing the outlet position. Both inlet solutions were prepared using diluted phosphoric acid solution (25 wt% P_2O_5) to match industrial process condition (reactions carried out in a concentrated acid environment). The detailed feed compositions can be found in Table 6.1.

Table 6.1: Feed compositions for all MSMPR experiments

	$CaHPO_4$ (wt%)	H_2SO_4 (wt%)	P_2O_5 (wt%)
$CaHPO_4$ Feed	5.60	–	23.60
H_2SO_4 Feed	–	4.10	23.98

This MSMPR setup was used to perform reactive crystallization until achieving steady state. Both feed solutions and the crystallizer were preheated beforehand to the desired temperature and maintained at the same value throughout the experiment. The crystallizer was thermostatically regulated by circulating water through the jacketed walls. The two inlet solutions were fed to an initially empty crystallizer at constant and equal volumetric flowrates. Slurry solutions withdrawn from the outlet were separated into solid and liquid phases by filtration. Here an intermittent withdrawal scheme is employed to remove all the slurry above the set level (usually

around 10% of the total reaction volume), therefore the withdrawal would take place every 1.5 to 4.5 minutes depending on the inlet flowrates and the discharge time is set to about 25 s. This way the outflow rate would be sufficiently high to carry out all crystals and no slurry would settle back to the reactor vessel. Both particle size distribution and solute concentration were monitored from startup to steady state operation. Different steady states can be achieved by manipulating the residence time of the reaction system through adjusting the flowrate of the feed solutions.

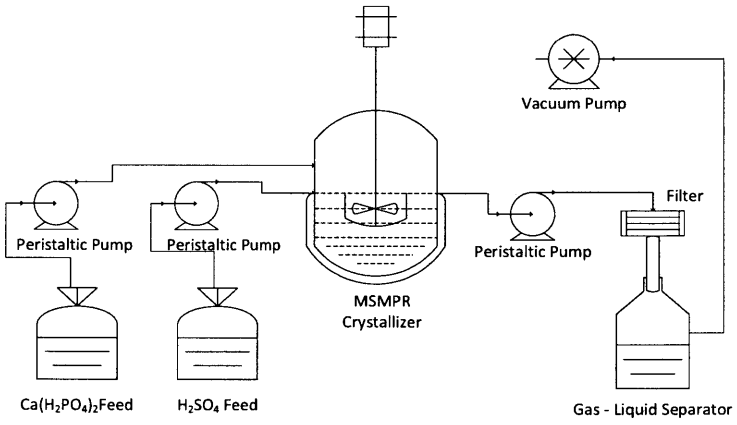

Figure 6-1: Schematic diagram of the MSMPR experimental setup

Sample Characterization The system is said to have reached its steady state when (1) crystal size density reaches a stable distribution, and (2) solute concentration does not change with time. CSD is monitored directly online using focused beam reflectance measurement (FBRM). Once the particle density is observed to be relatively stable, the solute concentration (total calcium concentration) was then measured using an ion-specific electrode (ISE) from a 100 times diluted sample. The concentration measurement process is repeated every ten to fifteen minutes until less than 1% change is observed for two consecutive measurements. The ISE is only used to further confirm that the system has reached its steady state in addition to a fixed

particle chrod length distribution detected by FBRM. Each steady-state liquid sample is analyzed by inductively coupled plasma (ICP) for accurate total Ca, S, and P element concentration. All three element concentrations are collected to cross-verify the measurement through overall mass balance and reaction stoichiometry. The steady-state supersaturation ratio defined in equation (2.18) can then be computed using the MSE thermodynamic model by providing the ICP measured solution composition.

6.2 Growth Rate Estimation from CSD

Here, FBRM measurement is used directly and assumed to be equivalent to the true size distribution data. Therefore, before fitting kinetic parameters, we need to find out the corresponding growth rate at the steady state condition. To do this, we make use of the steady state analytical solution (Equation (5.15)). Since $f_{measured}(L)$ is known from FBRM, one thing we could do to find out $G(\sigma)$ at given σ is to fit $f_{measured}(L)$ against L directly. This can be easily done by taking the logarithm at both sides of equation (5.15) and then directly apply linear regression. However, in practice, this could not be easily done because FBRM has a detection limit. All particles with size smaller than $1\mu m$ could not be detected although at steady state, the smaller the crystals are, its number grows exponentially based on the analytical solution. This is illustrated in Figure 6-2.

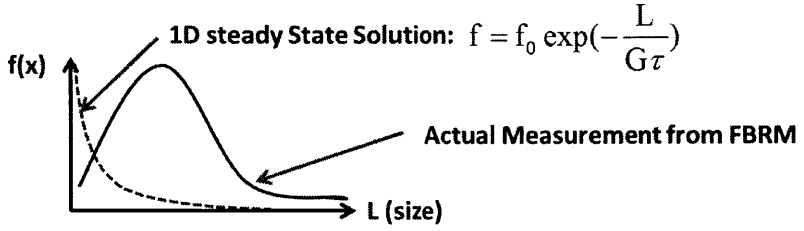

Figure 6-2: Graphical illustration of FBRM measurement compared to analytical steady state solution of CSD

One way to overcome this problem is to convert the number density $f(L)$ to volume density denoted as $f_v(L)$. This way, the effect of small size crystals almost diminishes as their volume contribution is almost negligible. Here the volume density

refers to a normalized density.

$$f_v(L_i) = \frac{\int_{L_i}^{L_{i+1}} L^3 f(L) dL}{\int_0^{\infty} L^3 f(L) dL} \tag{6.1}$$

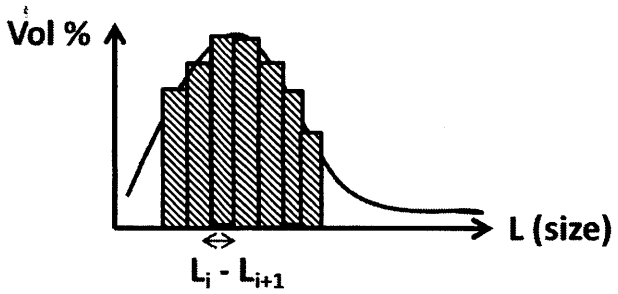

Figure 6-3: Graphical illustration of converting number density to volume density

The analytical volume density (equation (6.2)) can be derived from the steady state solution.

$$f_v(L_i) = \frac{\int_{L_i}^{L_{i+1}} L^3 f(L) dL}{\int_0^{\infty} L^3 f(L) dL} \tag{6.2}$$

$$= \frac{\int_{L_i}^{L_{i+1}} L^3 f_0 e^{-\frac{L}{G\tau}} dL}{\int_0^{\infty} L^3 f_0 e^{-\frac{L}{G\tau}} dL} \tag{6.3}$$

$$= \frac{\int_{L_i}^{L_{i+1}} L^3 e^{-\frac{L}{G\tau}} dL}{6(G\tau)^4} \tag{6.4}$$

Now we can estimate growth rate based on volume density measurements by minimizing the sum of squared errors between the measured volume density and the analytical volume density to find $G(\sigma)$.

$$\min_G \sum_{L_i} (f_{v,m}(L_i) - f_v(L_i))^2 \tag{6.5}$$

Nucleation rate is calculated from steady state mass balance equation (5.17) using the estimated G value from CSD.

6.3 Kinetic Parameters

Kinetic parameters of the semi-empirical growth and nucleation relations (5.1) and (5.2) were estimated using data collected from steady-state MSMPR experiments. Equations (5.1) and (5.2) were transformed by taking the logarithm at both sides so linear regression can be applied. The growth rate exponent was fixed at 2 while all the other kinetic parameters are fitted. This is done because when growth rate exponent is relaxed in parameter fitting, it is found to be very close to 2, therefore we fix it at 2 to give an extra degree of freedom in fitting. Detailed experimental conditions of all the MSMPR experiments conducted were summarized in Table 6.2. Model parameters were fit for the 25, 40, and 60°C data. The estimated growth and nucleation kinetic parameters are summarized in Table 6.3.

Table 6.2: Experimental conditions for MSMPR experiments

Expt.#	Temperate (°C)	Residence time (min)	Feed flowrate (ml/min)	Agitation rate (rpm)
1–3	25	12, 24, 54	1.70, 0.90, 0.40	350
4–6	40	24, 32, 75	1.40, 1.00, 0.45	350
7–9	60	17, 30, 64	1.50, 0.85, 0.50	350
10–12	50	19, 23, 55	1.10, 0.90, 0.40	350

Table 6.3: Fitted growth and nucleation kinetic parameters

Parameters	G	Parameters	B
$\ln k_g'$ (μm/min)	$28.449 \pm 3\%$	$\ln k_b'$ (#/m^{3}min)	$27.363 \pm 0.5\%$
E_g/R (K)	$8.53 \times 10^3 \pm 3\%$	E_b/R (K)	–
g	2.00	b	$2.88 \pm 5\%$

The model-calculated growth and nucleation rates and the experimentally measured values at different supersaturation as well as temperatures are plotted against each other in Figures 6-4 and 6-5. The power law relation with an Arrhenius form of the rate constant is observed to well describe the gypsum crystal growth rate in phosphoric acid solutions. The nucleation rate is found to have a very weak dependency on temperature (the hypothesis test of $E_b/R = 0$ gives a P-value of 0.4 indicates that

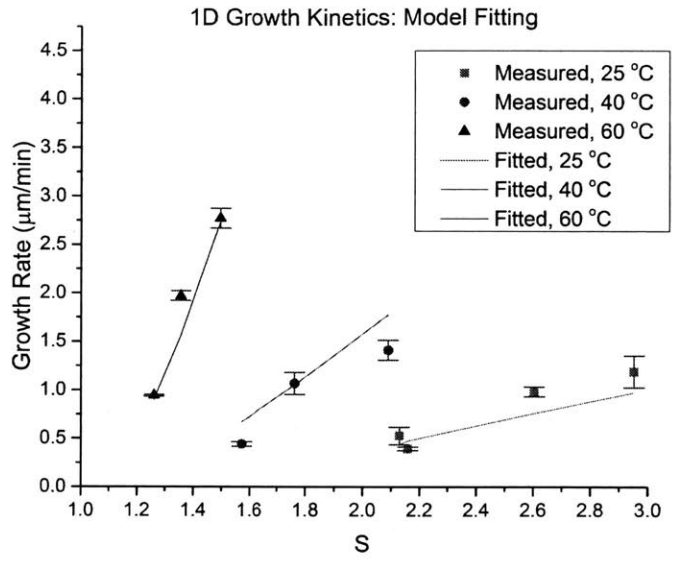

Figure 6-4: $CaSO_4 \cdot 2\,H_2O$ 1D growth kinetics at different supersaturation ratio and temperature. Points are experimental measurements. The lines are the power law model calculation.

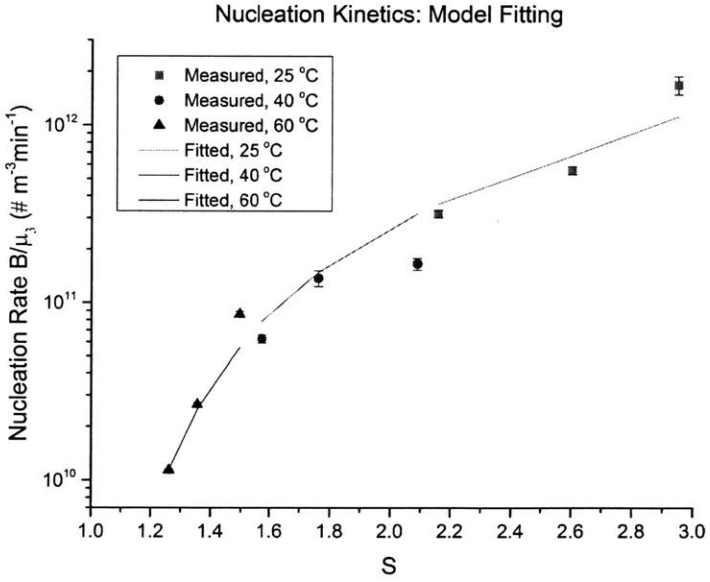

Figure 6-5: $CaSO_4 \cdot 2\,H_2O$ secondary nucleation kinetics at different supersaturation ratio and temperature. Points are experimental measurements. The lines are the power law model calculation.

it is not necessary to include the temperature term in the model), therefore a fixed rate constant is used in the rate law instead of the Arrhenius form. Efforts were made to compare our numbers with prior published results, however, very limited study on the kinetics of gypsum crystallization from a phosphoric acid solution has been found (most of the literature work involves a different solution system such as water, salt water, or sulfuric acid). The only prior result that we could find that studies the exact same system is from White [80], where the presented growth rate also employs an Arrhenius-form rate constant with a second-order supersaturation dependency and the nucleation rate has no temperature term with only a first-order supersaturation dependency. However, their study defines supersaturation in terms of the concentration of total calcium ion, which is not a proper way to represent supersaturation as pointed out in our earlier discussion (see chapter 2). Numerical comparison has been made between our and their kinetic models at the same conditions. The growth rate prediction is about 30–60 times different while the nucleation rate prediction is different by orders of magnitude. Overall, it seems that there are not any prior published results that are directly comparable to the results presented here.

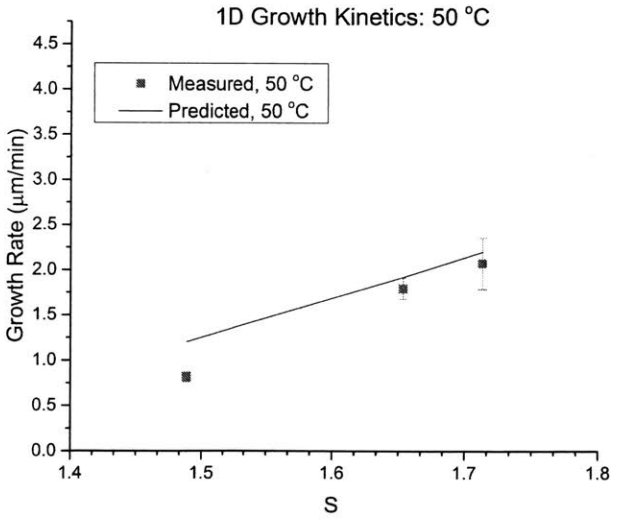

Figure 6-6: $CaSO_4 \cdot 2H_2O$ 1D growth kinetics at different supersaturation ratio and 50°C. Points are experimental measurements. The line is the power law model prediction.

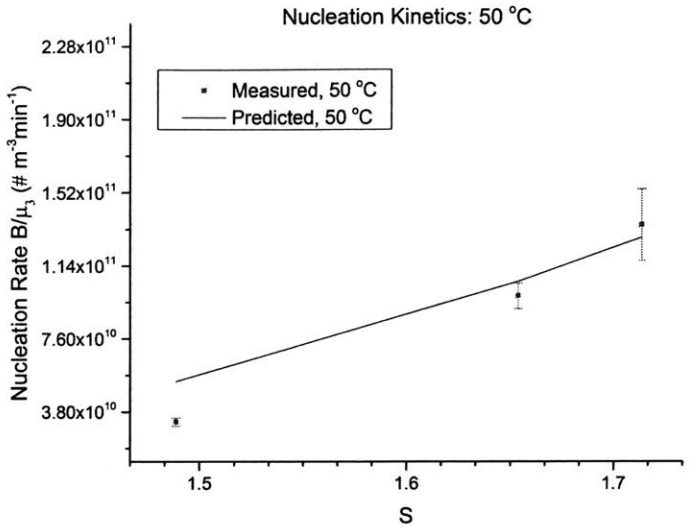

Figure 6-7: $CaSO_4 \cdot 2\,H_2O$ secondary nucleation kinetics at different supersaturation ratio and 50°C. Points are experimental measurements. The line is the power law model prediction.

Again, model verification is performed using the last set of data collected from the MSMPR experiments at 50°C, with results shown in Figures 6-6 and 6-7. The predicted growth and nucleation rates are reasonably consistent with the experimental data.

6.4 Limitation of 1D Model

Although the fitted model shows reasonable predication at 50 °C, when we apply it to 80 °C, both growth and nucleation prediction are not satisfactory (Figure 6-8 and 6-9). This indicates that our 1D model is not capable of describing gypsum crystallization in phosphoric acid solution at high temperature.

This is very likely due to the fact that gypsum crystals produced from dihydrate processes are generally in needle-like morphology (Figure 6-10). Therefore, they are not very close to uniform spheres so FBRM's measurement of particle chord length distribution does not represent their true size distribution to a good extend. However, our model works reasonable up to 60 °C, which implies that gypsum needles are not

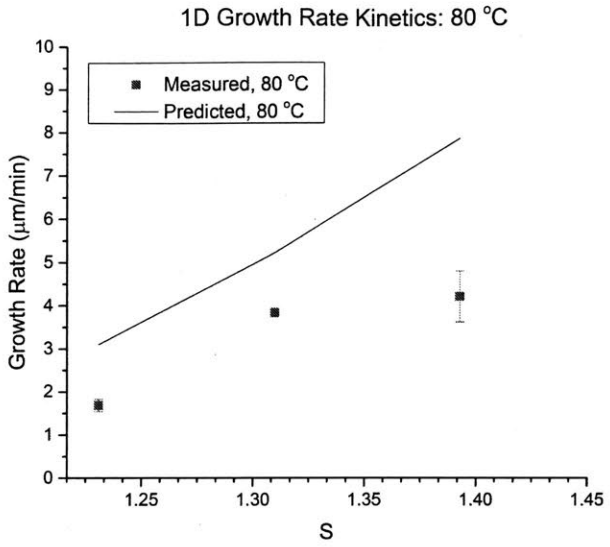

Figure 6-8: $CaSO_4 \cdot 2\,H_2O$ 1D growth kinetics at different supersaturation ratio and 80°C. Points are experimental measurements. The line is the power law model prediction.

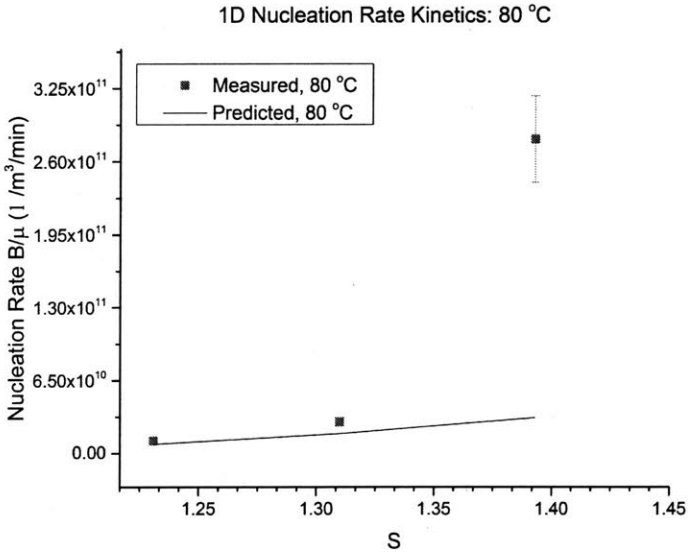

Figure 6-9: $CaSO_4 \cdot 2\,H_2O$ secondary nucleation kinetics at different supersaturation ratio and 80°C. Points are experimental measurements. The line is the power law model prediction.

very long at relatively low temperature but its effect becomes more dominant at high temperature. This hypothesis is consistent with our observation as the aspect ratio

exhibit an increasing trend from low to high temperature (Figure 6-11).

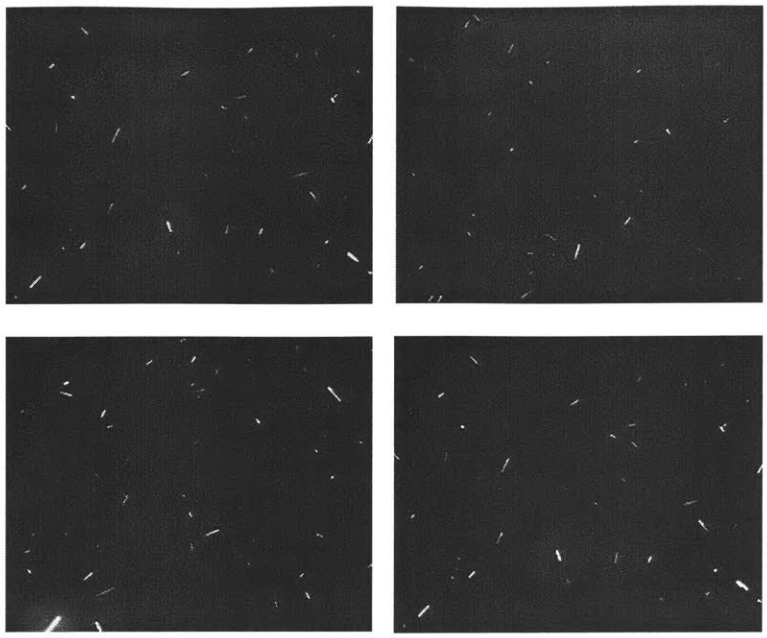

Figure 6-10: Microscopic image of $CaSO_4 \cdot 2\,H_2O$ crystal produced from high temperature MSMPR reactions

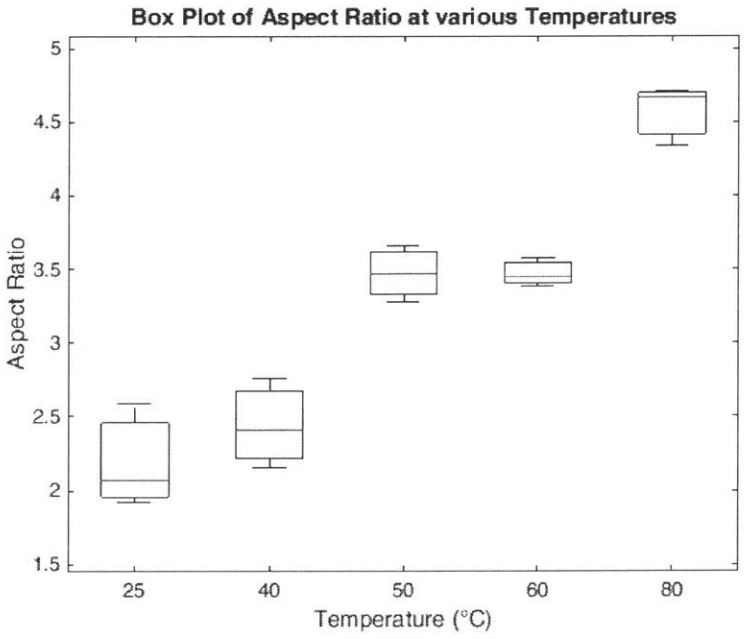

Figure 6-11: Boxplot of aspect ratio distribution at various temperatures

Hence, one independent growth dimension model is not sufficient in this case in describing needle crystal growth kinetics. We would need to make use of the two growth dimension model. The work done is discussed in the next chapter.

Chapter 7

Two Growth Dimension Kinetic Model

Our previous study[55] and other qualitative work[2] on gypsum crystallization have demonstrated that gypsum crystals exhibit a varying aspect ratio at different temperature and concentration, which is due to each facet of the crystal particle having different surface chemistry. Each dimension grows at a different rate, which causes the ratio between the dimensions of the crystal lattice to vary with temperature. As discussed earlier, the 1D PBM is insufficient to model crystal morphology, and thus a 2D PBM is necessary to model distributions of crystals of varying shape (i.e., aspect ratio). This thus requires the use of 2D growth kinetics. This chapter presents the work done towards obtaining such kinetic framework, which includes the experimental procedure for measuring the 2D CSD, and the methodology finding corresponding growth rates. The fitted model and its estimated parameters are quantitatively validated against experimental measurements.

7.1 Gypsum Crystal Morphology

Gypsum crystal morphology is represented by two characteristic lengths, L_1 and L_2, as shown in Figure 5-1 with a hexagonal cross-sectional area. In this description of gypsum crystals, the shorter dimension (L_2) represents twice the circumradius of the

hexagonal cross section and the crystal volume and surface area is

$$V_c = \frac{3\sqrt{3}}{8} L_1 L_2^2 \tag{7.1}$$

$$A_c = 3L_1 L_2 + \frac{3\sqrt{3}}{4} L_2^2 \tag{7.2}$$

where k_v, the crystal shape factor, in this case has a value of $\frac{3\sqrt{3}}{8} \approx 0.65$. Therefore, $\mu_{1,2}$ or $\mu_{1,1} + \frac{\sqrt{3}}{4}\mu_{0,2} \approx \mu_{1,1}$ can be used in the nucleation rate equation.

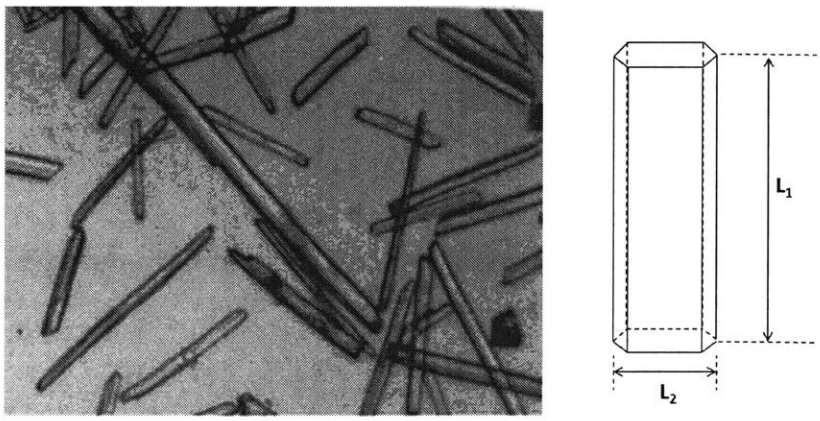

(a) Needle shape gypsum crystals. Reprint(b) 2D description of needle by permission from John Wiley and Sons [11],shape gypsum crystals Copyright 1984.

Figure 7-1: Gypsum crystal morphology

7.2 Continuous Crystallization Experiments

Materials For all experiments, reagent-grade calcium phosphate monobasic $Ca(H_2PO_4)_2$, sulfuric acid H_2SO_4 (96 wt%), and phosphoric acid H_3PO_4 (85 wt%, 99.99% trace metal basis) were purchased from Sigma-Aldrich. Ultrapure water was used for solvent dilution. A couple of choices such as $CaHPO_4$ [2, 61] and $Ca(H_2PO_4)_2$ [74, 5] can be used to model raw phosphate rock and the choice should not affect the kinetic study results. However, we later found that the purchased $Ca(H_2PO_4)_2$ has almost no metal impurities, which makes it a better choice for the crystallization kinetics of the pure system. Therefore, calcium phosphate monobasic is used instead of calcium

phosphate dibasic as in the 1D study.

Experimental Setup The same setup as shown in figure 6-1 is used here to carry out MSMPR experiments. Two feed streams consisting of calcium phosphate monobasic and sulfuric acid respectively were pumped continuously to a 50-ml glass-jacked crystallizer. Overhead mechanical agitation was used to ensure good mixing of the reactants and the reaction volume was maintained at a constant value by fixing the outlet position. Both inlet solutions were prepared using diluted phosphoric acid solution (25 wt% P_2O_5) to match industrial process condition (reactions carried out in a concentrated acid environment). The detailed feed compositions can be found in Table 7.1.

Table 7.1: Feed compositions in wt% for all MSMPR experiments

	$Ca(H_2PO_4)_2$	H_2SO_4	P_2O_5	H_2O
$Ca(H_2PO_4)_2$ feed	7.5 - 10.0	–	22.50 - 23.13	67.50 - 69.38
H_2SO_4 feed	–	3 - 4.10	23.98 - 24.25	71.92 - 72.75

The MSMPR setup was used to perform reactive crystallization until steady-state operation was obtained. Both feed solutions and the crystallizer were preheated beforehand to the desired temperature and maintained at the same value throughout the experiment. The crystallizer was thermostatically regulated by circulating water through the jacketed walls. The two inlet solutions were fed to an initially empty crystallizer at constant and equal volumetric flowrates. Slurry solutions withdrawn from the outlet were separated into solid and liquid phases by filtration. An intermittent withdrawal scheme was employed to remove all the slurry above the set level (usually around 10% of the total reaction volume), so that the withdrawal takes place every 1.5 to 4.5 minutes depending on the inlet flowrates and the discharge time was set to about 15 seconds. In this way, the outflow rate would be sufficiently high to carry out all crystals and no slurry would settle back to the reactor vessel. Both the particle size distribution and solute concentration were monitored from startup to steady-state operation. The system was judged as reaching its steady state when (1)

the crystal size density reached a stable distribution, and (2) the solute concentration did not change with time. Different steady states can be achieved by manipulating the residence time of the reaction system through adjusting the flowrate of the feed solutions. The conditions for all of the experiments are summarized in Table 7.2. Residence time is computed based on the measured volume and flowrate for accuracy.

Table 7.2: Experimental conditions for MSMPR experiments

Temperature (°C)	Residence time (min)	Feed flowrate (ml/min)	Volume (ml)	Agitation rate (rpm)
25	14,21,53	1.65, 1.05, 0.42	45, 45, 45	450
30	10, 15, 30	1.54, 0.91, 0.46	32, 28, 28	450
40	19, 26, 44	1.34, 0.91, 0.53	52, 47, 47	450
45	15, 27	1.59, 0.89	48, 48	450
50	13, 19, 31	1.51, 1.03, 0.53	39, 39, 33	450
55	12, 21, 47	1.66, 0.98, 0.44	42, 42, 42	450
60	13, 19, 19, 54	1.67, 0.98, 1.48, 0.53	43, 37, 55, 55	450
65	17,24,40	1.47, 1.05, 0.53	51, 51, 43	450
80	13,22,45	1.50, 0.95, 0.40	41, 41, 36	450

Sample Characterization The chord length distribution was monitored online by insertion of a Focused Beam Reflectance Measurement (FBRM) probe into the MSMPR. Once the signal from the FBRM was observed to be relatively stable, the total calcium concentration were then measured using an ion-specific electrode (ISE) from a sample diluted by a factor of 100. The concentration measurement process was repeated every ten to fifteen minutes until less than 1% change was observed for two consecutive measurements. The ISE was only used to further confirm that the system had reached its steady state, in addition to a stable particle density being detected by FBRM. Each steady-state liquid sample was analyzed by inductively coupled plasma (ICP) to obtain accurate total Ca, S, and P element concentrations. The first three element concentrations are collected to cross-verify the measurement through an overall mass balance. The steady-state supersaturation ratio defined in (2.18) was then computed using the MSE thermodynamic model by providing the ICP-measured solution composition. The steady-state solids were washed by acetone

first and then dried in a vacuum oven overnight. Sonication of solids in mineral oil was performed for better separation of single crystals. Images of these gypsum crystals was then captured using moving stage microscope by spreading the crystal solids on glass slides with mineral oil. This is carried out by using the capture multi-point function on Nikon AR software by pre-defining a $n \times m$ grid on the XY plane. The grid size is chosen such that no overlapping occurs between adjacent images from all directions. Auto-focus using adaptive steps can be used to make sure images taken are of good quality which is important for using image analysis for object detection and size measurement. For each steady state solid sample, about 2-3 glass slides were prepared and captured under microscope to ensure at least 200 high quality images are collected. The resulting 2D size distribution was measured through a multi-scale image analysis technique.

7.2.1 Image Analysis

The construction of a 1D growth rate model only requires 1D size distribution data, which can be estimated from the chord length distribution from the focused beam reflectance measurement (FBRM) by a variety of first-principles and data-driven methods[71, 32, 83]. In the case of a 2D growth model, the distribution along multiple growth axes needs to be measured which motivates the use of on- or offline imaging technique.

Manual crystal detection was done first to remove agglomerates from the images after applying the default edge detection method. However, the data seems to be biased towards small crystals and only a limited amount of crystals can be sampled (on the order of 2000). To make this process more efficient and accurate, a different edge detection technique is applied to mass-process the images automatically.

In this work, images of steady-state gypsum crystals are collected through an automated moving-stage microscope with about 10,000 to 20,000 single crystal samples measured for each experimental run. A multi-scale image segmentation technique developed by Roberts[21] is adopted with additional removal of objects to exclude large agglomerates. The Canny method [15] is applied here for edge detection through

finding local maxima of the first derivative of the intensity function on gray-scaled images. Other approximation methods such as the Sobel or Prewitt method, zero-cross method can also been used. The multi-scale edge detection captures the complete delineation of edges, which may include some noise and is preferred for images with irregular pixel intensities. The method finds edges from multiple resolutions. The schematic diagram shown in figure 7-2 summaries the major steps involved in conducting a multi-scale image segmentation process as suggested by Roberts[21]. An example demonstration of the multi-scale segmentation method on sample microscopic images is shown in Figure 7-3.

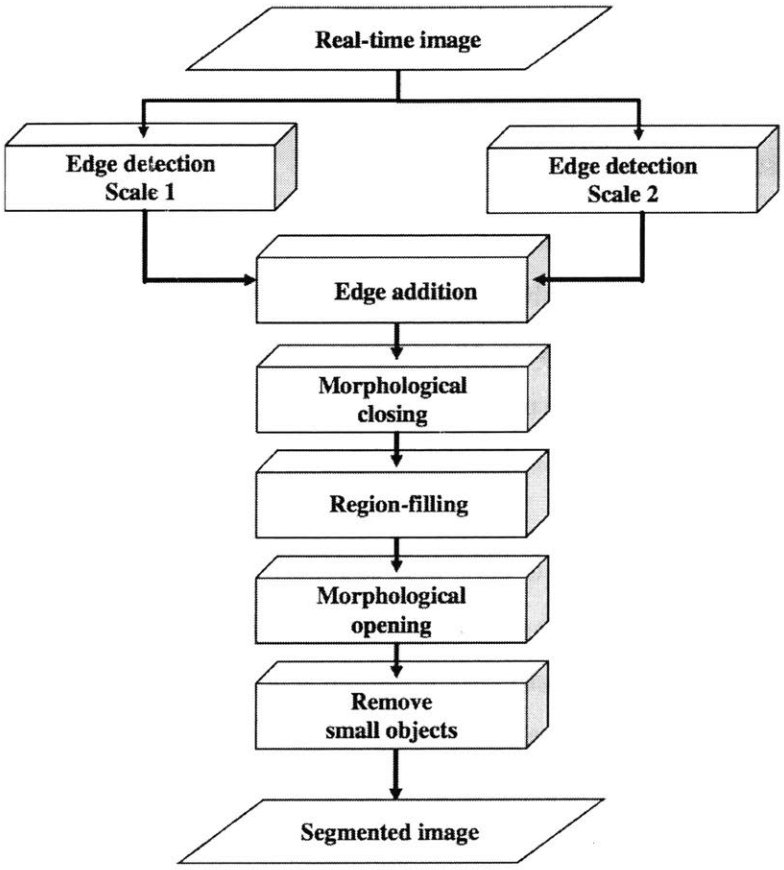

Figure 7-2: Schematic of multi-scale segmentation image analysis methodology. Reprint by permission from Elsevier [21], Copyright 2004

It is also important to make sure no or minimal bias is introduced from the image

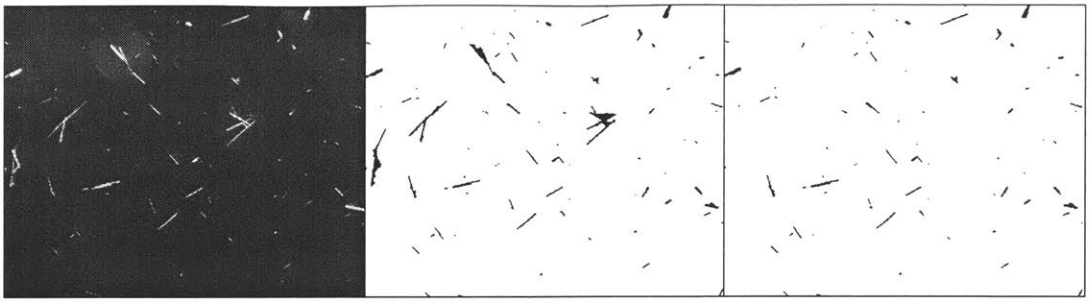

(a) Original image **(b) After edge detection** **(c) Large objects removal**

Figure 7-3: Multi-scale segmentation image analysis techniques applied to a sample microscope image.

analysis. More specifically, images taking at different magnification would lead to bias towards different sized crystals. Particularly, low magnification results in bias towards large crystals while high magnification results in bias towards small crystals. To resolve this issue, the final normalized cumulative distribution is reconstructed by combining the high magnification size distribution data for the small size crystals with low magnification size distribution data for the large size crystals and converge the two parts for the mid-range size crystals. The reconstructed distribution is compared with the FBRM measurement at low temperature (because at low temperature, FBRM measurement gives a reasonably accurate representation of the true size distribution since crystal aspect ratio is small) and the results indicate good agreement (Figure 7-4). This provides confidence in our reconstruction method for estimating the actual crystal size distribution. This is applied whenever we think bias is significant using measurements collected from just the low magnification images. Although later we found that it is very hard to collect good quality images at high magnification. Therefore, it is not generally applied for all of our samples. The algorithm is implemented in Matlab using its image toolbox functionalities.

7.3 Growth Rate Estimation from CSD

The steady state size distribution for each dimension can be derived analytically as (5.27) and (5.28). Besides using the measured (normalized) number density directly,

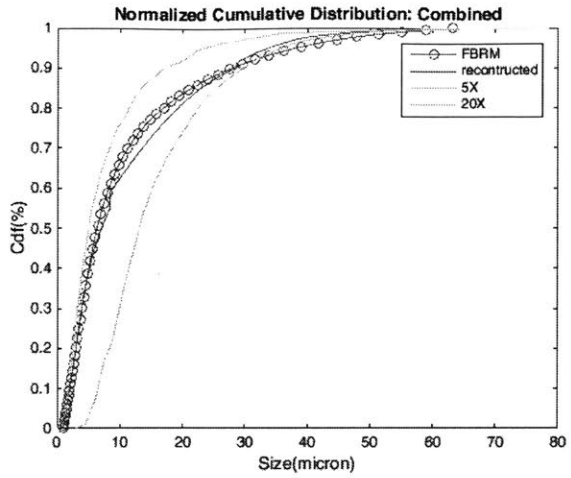

Figure 7-4: Reconstruction of normalized cumulative number density applied to steady state samples from 25 °C

both the (normalized) cumulative number density ($\int_0^{L_i} f(L)dL$) and the (normalized) volume density ($(\int_0^{L_i} L^3 f(L)dL$) are also common choices for estimating growth rate at a given supersaturation and temperature level. Analytical expressions for all three densities can be derived easily from (5.27) and (5.28). Figure 7-5 plots the estimated growth rate for both dimensions at various supersaturation using the three different densities. In general they give similar estimates although the ones obtained from using the cumulative number density is slightly smaller. This is probably due to the fact that using cumulative number density for estimation requires no discretization of the size (i.e. division into different bins for construction of distribution) comparing to the other two density metrics. Based on that, the (normalized) cumulative number density is selected to be used for growth rate estimation.

7.4 Kinetic Parameters

The kinetic parameters of the semi-empirical growth and nucleation relations (5.4), (5.5) and (5.6) were estimated using data collected from steady-state MSMPR experiments. Detailed experimental conditions of all of the MSMPR experiments conducted were summarized in Table 7.2. The model parameters were fitted using all data except

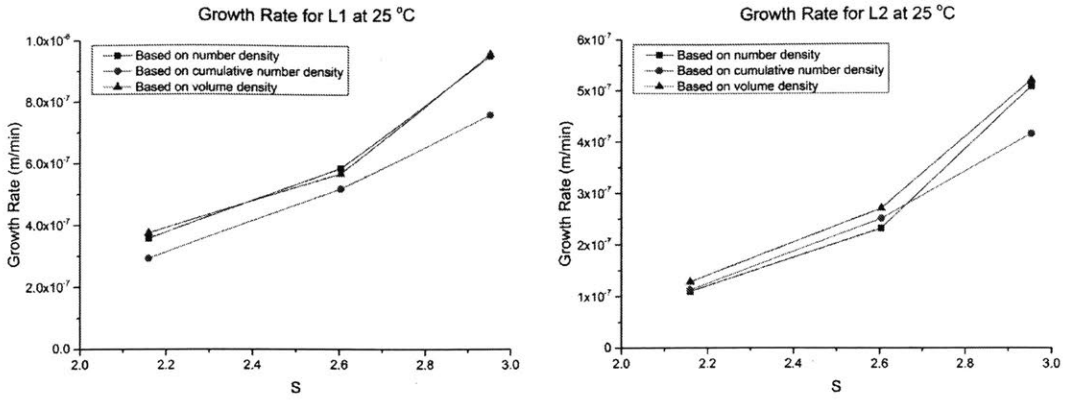

(a) $G_1(\sigma)$ at 25 °C (b) $G_2(\sigma)$ at 25 °C

Figure 7-5: Growth rate estimates using different size density data

for the 50 °C ones.

The model parameters were obtained by minimizing (5.10) using global search with multiple starting points. The estimated growth and nucleation kinetic parameters are summarized in Table 7.3. A range of [1,2] is added as an additional optimization constraint on the supersaturation exponents (g_1, g_2) for the growth rates. $\mu_{0,0}$ is found to give better fit for nucleation rates here.

Table 7.3: Estimated growth and nucleation kinetic parameters

Parameters	G_1	G_2	Parameters	B
$\ln k_g'$ (μm/min)	14.39 $\pm$6 %	12.37 $\pm$9 %	$\ln k_b'$ (1/min)	2.6
E_g/R (K)	4.14 $\times 10^3 \pm$ 7%	3.63 $\times 10^3 \pm$ 9%	E_b/R (K)	1529 $\pm$ 300
g	1.00	1.00	b	1.00 $\pm$ 0.15

The model-calculated growth and nucleation rates and the experimentally measured values at different supersaturations as well as temperatures are plotted against each other in Figure 7-6,7-7,7-8. Only the data points at 25, 40, 60 and 80 °C are shown here. The power law relation with an Arrhenius form for the rate constant is observed to well describe the two dimensional growth model for gypsum in phosphoric acid solution. The nucleation rate is found to have a very weak dependency on the temperature; therefore, a fixed rate constant is used in its rate law. Model verification is performed using 50 °C data points, with results shown in Figure 7-9,

7-10. The predicted two-dimensional growth and overall secondary nucleation rates are reasonably consistent with the experimental measurement.

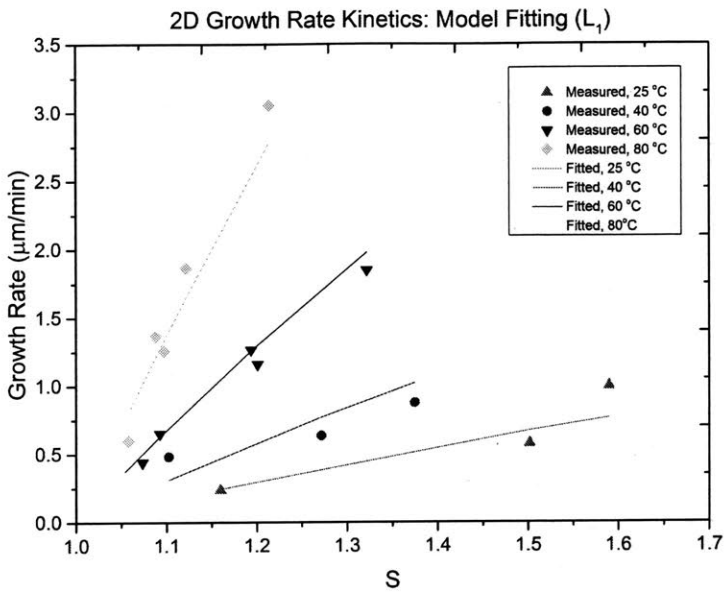

Figure 7-6: $CaSO_4 \cdot 2\,H_2O$ 2D growth kinetics at different supersaturation ratio and temperature for growth dimension L_1. Points are experimental measurements. The lines are the power law model calculation.

7.5 Growth Rate Dispersion

However, if we further examine the predicted crystal size distribution, we found with the above assumed size-independent growth model, the crystals at steady state will all be at a fixed aspect ratio and this is clearly not what we have observed from our measured 2D size distribution (figure 7-11).

To explain this broadening effect, growth rate dispersion (GRD) is introduced to our overall population balance model. GRD is a phenomenon resulting from different growth rates for crystals of the same size, most likely due to the different surface properties developed as a result of deformation or dislocation of the surface structure. The mechanism is known to be responsible for many sophisticated crystal structures and leads to the broadening of the crystal size distribution as observed.

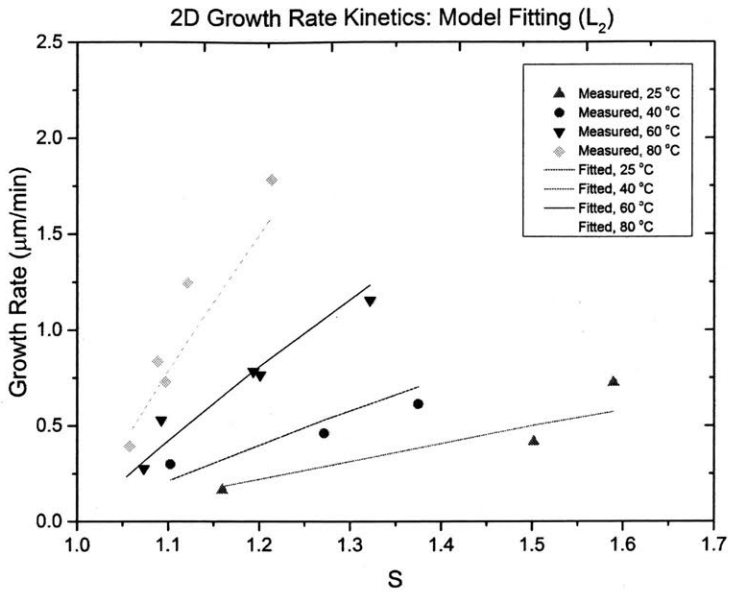

Figure 7-7: $CaSO_4 \cdot 2\,H_2O$ 2D growth kinetics at different supersaturation ratio and temperature for growth dimension L_2. Points are experimental measurements. The lines are the power law model calculation.

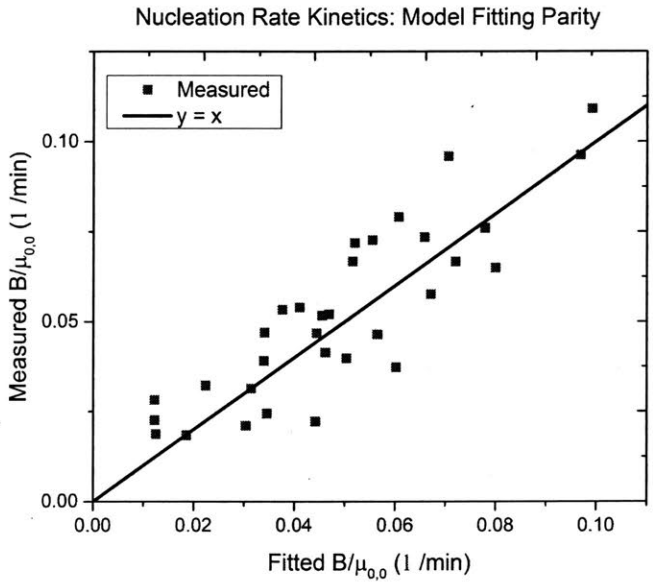

Figure 7-8: Parity plot for measured $CaSO_4 \cdot 2\,H_2O$ secondary nucleation kinetics against the model fitted values

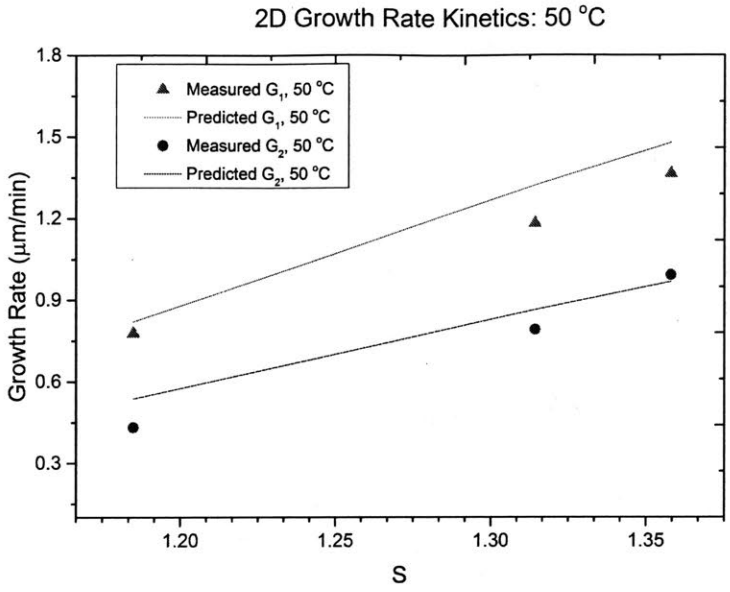

Figure 7-9: $CaSO_4 \cdot 2\,H_2O$ 2D growth kinetics at different supersaturation ratio and 50°C for L_1 and L_2. Points are experimental measurements. The line is the power law model prediction.

Here we adopted the random fluctuation (RF) model assumes crystals have temporal variation around a mean growth rate similar to the random fluctuation in molecular diffusion[51]. Adding the dispersion term thus changes the steady-state governing equation for a MSMPR system with two characteristic lengths to as follows:

$$G_1 \frac{\partial f}{\partial L_1} + G_2 \frac{\partial f}{\partial L_2} = B_0 \delta(L_1)\delta(L_2) - \frac{f}{\tau} + D_1 \frac{\partial^2 f}{\partial L_1^2} + D_2 \frac{\partial^2 f}{\partial L_2^2} \tag{7.3}$$

where D_i is the effective growth rate diffusivity. This thus changes the growth and nucleation model parameters presented above slightly and adds complexity to model fitting as we also need to fit the growth rate diffusivity at the same time. My collaborator worked on the methodology to resolve this issue. The details of his work regarding performing parameter estimation with GRD can be found in our publication [86]. One thing to mention here is that the kinetics model for growth rate diffusivity is rarely discussed in the literature. One of the earliest empirical evidence suggests that the magnitude of the random fluctuation is dependent on supersaturation. Such

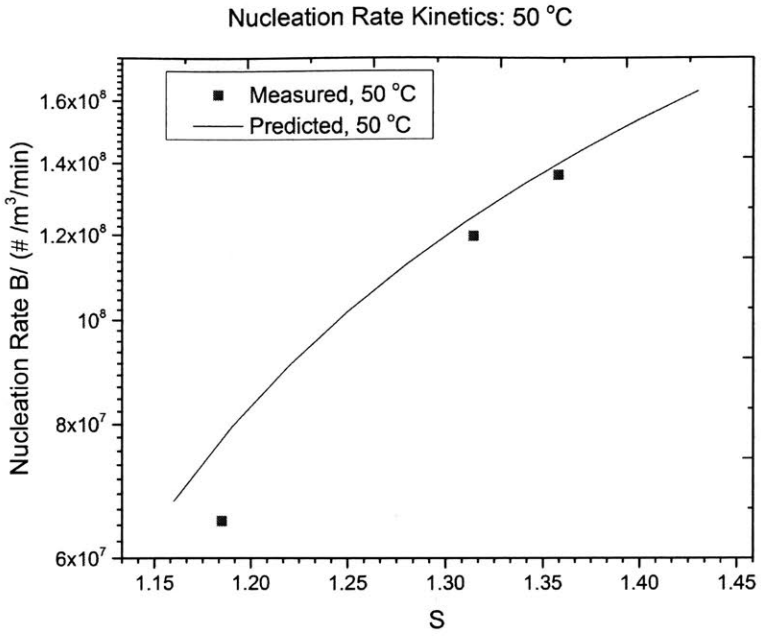

Figure 7-10: $CaSO_4 \cdot 2\,H_2O$ secondary nucleation kinetics at different supersaturation ratio and 50°C. Points are experimental measurements. The line is the power law model prediction.

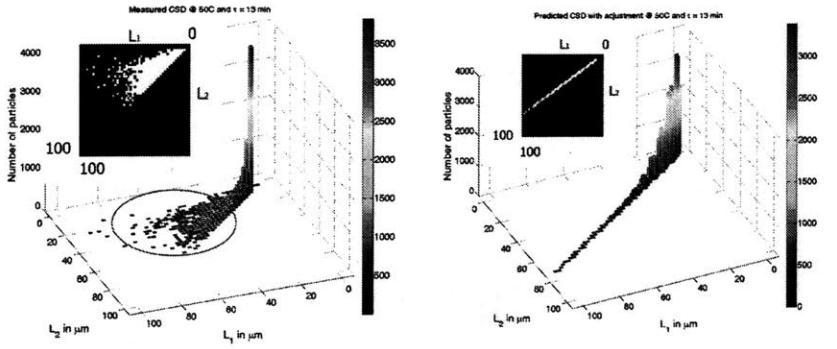

Figure 7-11: Measured and predicted CSD before introducing growth rate dispersion. The broadening effect of the CSD circled in red cannot be predicted by the 2D PBM with only size-independent growth and nucleation mechanisms alone [86]

dependency is assumed to follow a power-law expression[87]

$$D_1 = k_{d_1}\sigma^{d_1} \tag{7.4}$$

$$D_2 = k_{d_2}\sigma^{d_2} \tag{7.5}$$

where k_{d_i} and d_i are fitting parameters. Another study[81] in the early 1970s (discussed in a review by Ulrich [72]) suggested that the magnitude of the growth rate diffusivity is directly proportional to the growth rate and can be modeled as a linear function,

$$D_1 = L_{d_1} G_1 \tag{7.6}$$

$$D_2 = L_{d_2} G_2 \tag{7.7}$$

The proportionality constant L_d was referred as the *dispersion length.*

Both of these empirical expressions are qualitatively consistent with the RF framework. A larger growth rate diffusivity is expected when the growth rate is larger and no diffusivity when the growth rate approaches zero. Since no previous work has quantitatively verified these functional forms, their fitting to the estimated growth rate diffusivity are compared. The second model proposed by White and Wright [81] shows significantly better fitting.

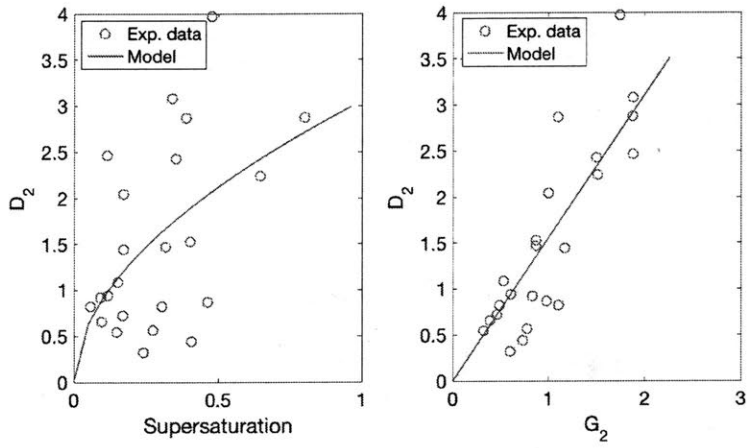

Figure 7-12: Comparison of goodness of fit for the two growth rate diffusivity models, (7.4) and (7.6) [86].

As a result, with the added growth rate dispersion term, the model now has the capability of predicting the broadening effect of aspect ratio at steady state as shown in figure 7-13. Particularly, the marginalized number density plot (figure 7-14), shows good agreement between the measurement and prediction.

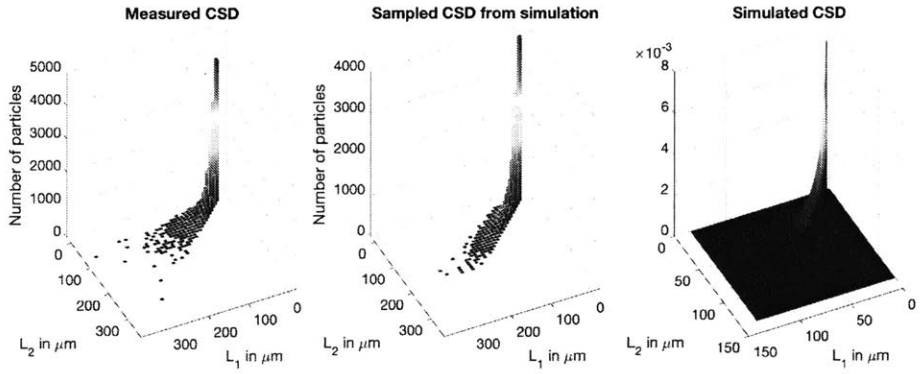

Figure 7-13: Comparison of measured and predicted 2D CSDs for a validation experiment at temperature of 60 °C and residence time $\tau = 13$ min [86].

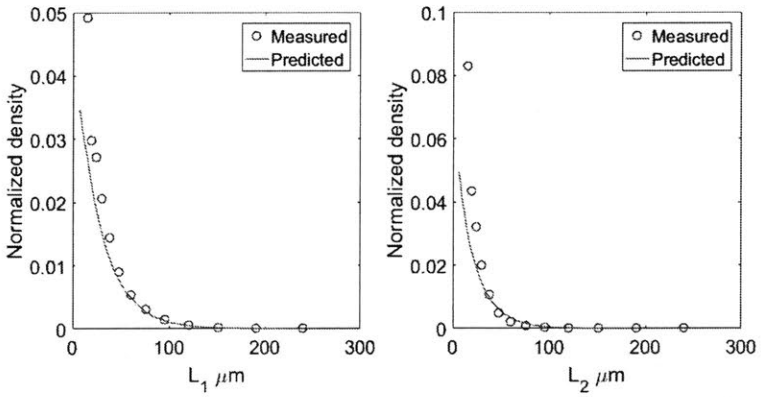

Figure 7-14: Marginalized number density plot comparison for a validation experiment at temperature of 60 °C and residence time $\tau = 13$ min [86].

THIS PAGE INTENTIONALLY LEFT BLANK

Chapter 8

Effect of Single Impurity on Crystal Growth

With the main ionic interactions captured through regression analysis using the collected gypsum solubility data as discussed in chapter 4, we managed to isolate impurity's thermodynamic contribution. This has never been done properly in the past, either not being considered by most researchers or not accounted for correctly from its role in altering solution speciation. This thus enables the calculation of proper liquid phase supersaturation when impurity ions are present in the system. Therefore, with the thermodynamic contribution properly captured in a supersaturation change, we can now look into its role as growth inhibitors. This is a general consensus that traces of certain additives are known to retard crystal growth (although there does exists impurities that leads to an increase in growth rate [53], it is a rather rare case). The extent of growth rate inhibition depends on a variety of factors such as the type of impurity and its concentration, supersaturation, temperature as well as the crystallizing solid since the surface interaction mechanism could differ[20]. Therefore in this chapter, we briefly review the models available in the literature for describing different impurity adsorption mechanism and test those against our experimental results in the presence of both single and multiple impurity ions to draw conclusions on the inhibition mechanism. The study is again carried out in a 2D framework to account for the shape changes.

8.1 Crystal Growth in the Presence of Impurities

Two dominant molecular-scale inhibition mechanism can be illustrated in Figure 8-1 [20]. Both types can cause changes in crystal growth rates when one considers impurity molecules only being adsorbed onto edges and surface, stay there for a while to block growth and eventually redissolve back into the solution phase while the other model assumes foreign particles incorporates into kink sites or being captured by the advancing step and becomes part of the crystal lattice [20]. The adsorption type usually predicts the existence of a growth dead zone where below certain critical supersaturation, no growth will be observed. Generally, such threshold supersaturation depends on both temperature and impurity concentration.

In general, most mathematical models developed in the literature assume impurity adsorption as the main mechanism and it will also be the focus of our study here. This is later verified through experiments as negligible or trace level of impurity were found in the collected solids.

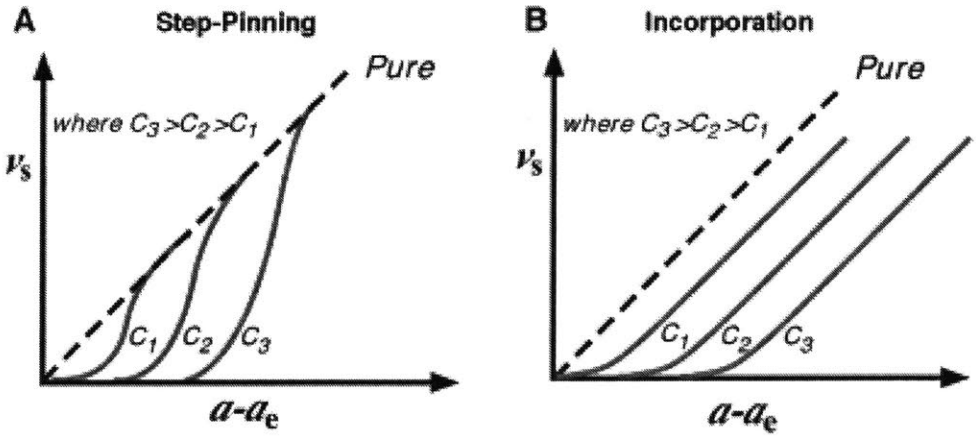

Figure 8-1: Mechanisms impurity ions or molecules can effect crystal growth (a) impurity adsorption (b) impurity incorporation Reprint by permission from The American Association for the Advancement of Science [20], Copyright 2000.

8.1.1 Step Pinning of Adsorbed Impurities

A crystal surface has three different types of sites for growth unit attachment that dominate the growth process: kinks, step ledges and surface terrace (Figure 8-2). Kinks and steps are the preferential sites for growth units capture as their bonding energy are higher comparing to surface terrace.

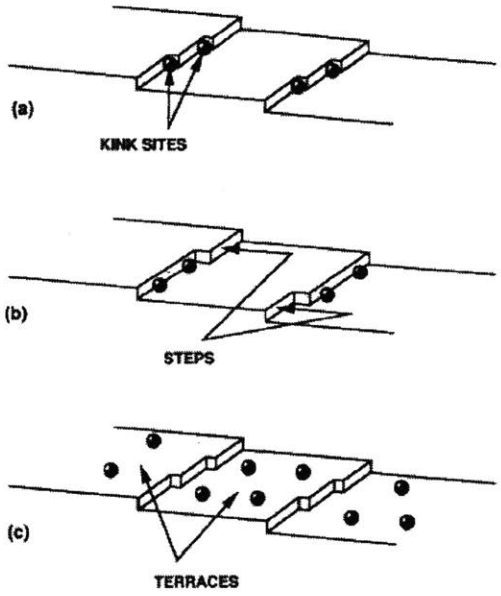

Figure 8-2: Key surface structures on an idealized crystal face (a) kink (b) step (c) terrace . Reprint by permission from Elsevier [51], Copyright 2002.

Therefore, impurities are either adsorbed on to the terrace and stays there if immobile or move to the preferential kink sites on the step when mobile. Thus the presence of impurity particles can pin the motion of the advancing steps by not only stop the movement of such a step but also physically block the integration of the crystallizing agent. Hence, when an advancing step meets a foreign particle, it will tend to curl around it as shown in Figure 8-3.

If the average distance L between the adjacent absorbed impurity particle is smaller than the critical diameter of a two-dimensional nucleus (denoted as $2r_c$), the advancing step will stop while if it is greater or equal to it, the step will squeeze between the neighboring particles. Therefore, this leads to a decrease in the average step velocity when impurity is present. Based on this idea, the advancing step

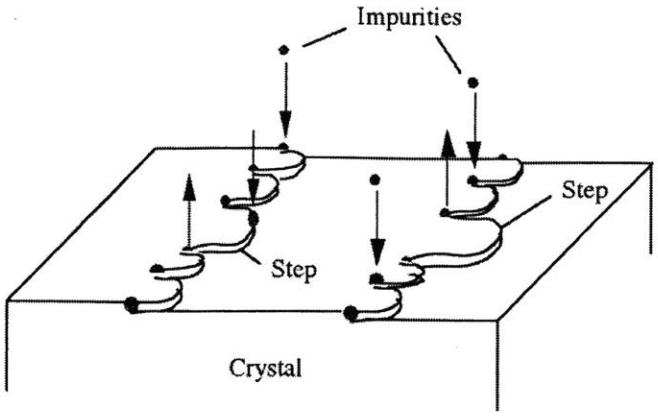

Figure 8-3: Step movement blocking by impurity particles. Reprint by permission from John Wiley and Sons [36], Copyright 2001.

velocity of a curved step can be quantified as [13]

$$\frac{v}{v_0} = 1 - r_c/r \tag{8.1}$$

where v_0 is the velocity of a linear step and v is the velocity of a curved step with curvature r. The critical radius of a 2D nucleus is given by [13]

$$r_c = \frac{\gamma a}{k_B T \sigma} \tag{8.2}$$

where γ is the linear edge free energy, a is the size of a growth unit which is also equivalent to the diameter of the host particle, k_B is the Boltzmann constant and T is the temperature in kelvin. Because the step only squeeze between adjacent impurity particles when it meets them during advancing and this does not happen at all instances, therefore the step velocity v changes with time. The maximum value $v_{\max} = v_0$ while the minimum value $v_{\min}$ can be found when the curvature $r = L/2$ (during such squeeze)

$$\frac{v_{\min}}{v_0} = 1 - 2r_c/L \tag{8.3}$$

Cabrera and Vermileya [14, 48] proposed to take the geometric mean of the min-

imum and maximum velocity in order to find the time-averaged velocity,

$$\frac{v}{v_0} = \sqrt{v_{\min} v_{max}} = \sqrt{1 - 2r_c/L} \tag{8.4}$$

While Kubota, Mullin and co-workers [37, 36] proposed to take the arithmetic mean of the minimum and maximum velocity to find the time-averaged velocity,

$$\frac{v}{v_0} = \frac{v_{\min} + v_{max}}{2} = 1 - r_c/L \tag{8.5}$$

This form is commonly used to calculate the average velocity.

8.1.2 Adsorption at Kinks

When adsorption occurs at kink sites, the linear coverage of impurity ions θ_l of kink sites along the step ledge can be found as the ratio between x_0, the average distance between active adsorption sites in a step and L [64]

$$\theta_l = x_0/L \tag{8.6}$$

By using this in equation (8.5), we find that the Kubota-Mullin model can be rearranged into

$$\frac{v}{v_0} = 1 - r_c/x_0\theta_l = 1 - \alpha_l\theta_l \tag{8.7}$$

$$\alpha_l = \frac{\gamma a}{k_B T x_0 \sigma} \tag{8.8}$$

Here α_l is impurity effectiveness factor. Additionally, this linear coverage should equal the surface coverage θ_s which can be found from adsorption isotherms. Here, we assume impurity adsorption is always at equilibrium (much faster time scale comparing to growth). The most common one is the Langmuir isotherm which suggests

that

$$\theta_s = \frac{K_i c_i}{1 + K_i c_i} \tag{8.9}$$

where c_i is impurity concentration, and K_i is the impurity adsorption equilibrium constant that is given by [19]

$$K_i = \exp(\frac{Q_{\text{i,diff}}}{RT}) \tag{8.10}$$

and $Q_{\text{i,diff}}$ is the differential heat of adsorption corresponding to θ_s. The step velocity is assumed to be proportional to the crystal growth rate

$$\frac{G}{G_0} \approx \frac{v}{v_0} \tag{8.11}$$

where G is the growth rate with impurity and G_0 is the growth rate without impurity. Now if we plug in θ_l using equation (8.9) into equation (8.7), we find the final Kubota-Mullin form as commonly presented in the literature as [65]

$$\frac{G}{G_0} = 1 - \alpha_l(\frac{K_i c_i}{1 + K_i c_i}) \tag{8.12}$$

$$\alpha_l = \frac{\gamma a}{k_B T x_0 \sigma} = \frac{\beta_{\text{KM}}}{\sigma T} \tag{8.13}$$

Here α_l is a function of both supersaturation and temperature while β_{KM} is a constant and it will be treated as one fitting parameter when we try to use Kubota-Mullin model to explain our data.

One thing to notice is that because this model is derived based on the pinning mechanism, it suggests that growth will stop whenever $L < 2r_c$. As per our derivation above, $L = x_0/\theta_l$ and as impurity concentration increases, θ_l will increase to be closer to 1. With an increasing θ_l, L will decrease and eventually it might fall below $2r_c$ when impurities occupy most of the active kink sites. Therefore, this model naturally generates a critical supersaturation where below such value, growth will be fully inhibited (usually referred to as the dead zone). This threshold value can be found

as

$$\sigma_c = \frac{\gamma a}{k_B T x_0} \frac{K_i c_i}{1 + K_i c_i} = \frac{\beta_{\mathrm{KM}}}{T} \frac{K_i c_i}{1 + K_i c_i} \tag{8.14}$$

which is a function of temperature and impurity concentration. The presence of such "dead zone" due to impurity has not reached an agreement in the scientific community. There are many experimental observations supporting critical supersaturation. [66, 70] However, many argue that the observation of "dead zone" is a misinterpretation due to increased solubility that was not accounted by the addition of impurities. [22, 25]. This model has been effectively used to describe growth rate inhibition in many systems and generalized for non-equilibrium impurity adsorption [38] as well as multiple impurities adsorption [64].

8.1.3 Competitive Adsorption Model

More recently, Martins and co-workers [46] have developed another model for describing crystal growth behavior in the presence of impurities. The Competitive Adsorption Model (CAM) is constructed based on assuming the solute molecules and the foreign particles are competing for the preferential kink sites. As discussed above, when we use the Langmuir isotherm to find θ_l for the impurity ion, we did not account for the fact that the crystallizing agent will also be occupying the kink sites and hence should reduce the effective number of active kink sites available for the foreign molecules to occupy. When supersaturation is high ($c >> c_i$), most of the kink sites should be occupied by the solute molecules rather than the impurity ions and thus $\theta_l << 1$ in this case.

Therefore, if we apply the above framework by considering crystal growth in impure solution as a multicomponent adsorption process where adsorption sites can be taken up by both the solute and the impurity, we can again make use of the Langmuir isotherm to find the surface coverage for the impure particles

$$\theta_s = \frac{K_i c_i}{1 + K_i c_i + Kc} \tag{8.15}$$

where c should be the solute concentration in the solution. K should also follows the form shown in equation (8.10) and here we denote its corresponding adsorption heat as $Q_{c,\text{diff}}$. According to the Kossel model [51], crystal growth in impure solution should involve three stages when impurity ions are mobile: (1) surface adsorption of impurity ion diffusing from the bulk solution (2) surface migration of the adsorbed impurity ion (3) step/kink adsorption of the surface migrated impurity ion.

Now the linear coverage of impurity along the step can be found by

$$\theta_l = \beta\theta_s \tag{8.16}$$

The parameter β essentially indicates the relative favoritism of the three adsorption stages. For very mobile impurities, $\beta >> 1$ and stage 2 and 3 are more favored and stage 1 is the limiting step. For less mobile impurities, $\beta < 1$, surface adsorption is favored and the opposite is observed [46]. Growth rate is linearly proportional to the density of absorbed solute molecule on the surface n_s according to the BCF model [13]. This value approaches the equilibrium value n_{se} near the step, and with the presence of impurity, this density will decrease to $n_{se}(1-\theta_l)$. Therefore, we can find the corresponding growth rate in impure solution as

$$\frac{G}{G_0} = 1 - \theta_l = 1 - \beta\theta_s \tag{8.17}$$

$$= 1 - \beta\frac{K_i c_i}{K_i c_i + Kc + 1} \tag{8.18}$$

Only when $\beta < 1$, no growth dead zone is present (Figure 8-4).

In the case of a two-dimensional growth mechanism, inhibition models will be developed for each of the growth dimensions. Because adsorption of metal impurity during crystallization only happens at the outermost surface, and impurity ions are not permanently adsorbed (otherwise would be the incorporation mechanism), the concentration of the impurity in solution should remain almost constant. This is also verified experimentally by examining impurity uptake in precipitated crystals.

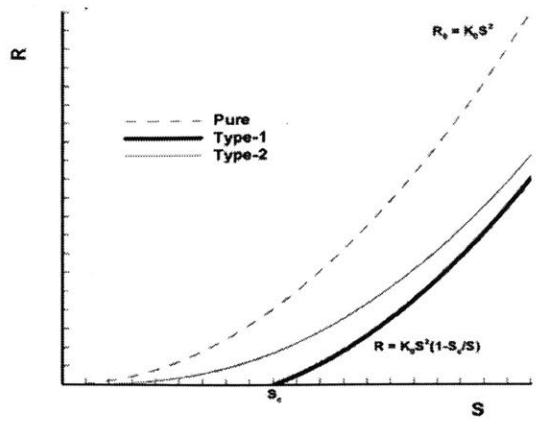

Figure 8-4: Growth rate curves in the presence of impurities as modeled by CAM. Reprint by permission from American Chemical Society [46], Copyright 2006.

8.2 Continuous Crystallization Experiments with Impurities

Materials For all experiments, reagent-grade calcium phosphate monobasic $Ca(H_2PO_4)_2$, sulfuric acid H_2SO_4 (96 wt%), phosphoric acid H_3PO_4 (85 wt%, 99.99 % trace metal basis) magnesium oxide MgO and aluminum nitrate nonahydrate ($Al(NO_3)_3 \cdot 9\,H_2O$) were purchased from Sigma-Aldrich. Ultrapure water was used for solvent dilution. A couple of choices such as $CaHPO_4$ [2, 61] and $Ca(H_2PO_4)_2$ [74, 5] can be used to model raw phosphate rock and the choice should not affect the kinetic study results. However, the purchased $Ca(H_2PO_4)_2$ has almost no metal impurities, which makes it a better choice here.

Experimental Setup A schematic diagram of the experimental setup is shown in Figure 6-1. The setup was designed to simulate wet phosphoric acid production with the presence of impurity ions. Magnesium oxide and aluminum nitrate nonahydrate is added to the calcium phosphate monobasic feed stream to introduce Mg^{2+} and Al^{3+} impurity respectively. The same procedure and sample characterization method is adopted here as used in the 2D study for the pure system. Different steady states can be achieved by manipulating the residence time of the reaction system through ad-

justing the flowrate of the feed solutions. Each steady-state liquid sample is analyzed by ICP to obtain accurate total Ca, S, P and impurity element concentrations. The steady-state saturation ratio defined in (2.18) can then be computed using the MSE thermodynamic model by providing the ICP-measured solution composition. Images of steady-state gypsum crystals are collected through an automated moving-stage microscope to make sure about 10,000 to 20,000 single crystal samples are captured for each experimental run. A multi-scale image analysis algorithm is then applied to obtain the resulting 2D size distribution.

8.3 Growth Inhibition Models with Mg^{2+}

Mg^{2+} is one of the main impurity ions in the raw phosphate rock and it is also present in a relatively abundant amount. Also, many studies have been done in understanding its effect in the past[61, 29, 26]. Therefore, experiments were first carried out in a system with Mg^{2+} ions in the entire temperature range up to 80 °C with a maximum Mg^{2+} impurity level of about 500 mg/L. The detailed feed compositions can be found in Table 8.1.

Table 8.1: Feed compositions in wt% for all MSMPR experiments with Mg^{2+}

	$Ca(H_2PO_4)_2$	H_2SO_4	P_2O_5	H_2O	MgO
$Ca(H_2PO_4)_2$ feed	7.5	–	23.13	69.37	0-0.15
H_2SO_4 feed	–	3.0	24.25	72.75	–

All the experiments carried out were summarized in Table 8.2.

Table 8.2: Experimental conditions for MSMPR experiments with added Mg^{2+}

Temperature (°C)	Residence time (min)	Mg^{2+} (mg/L)	Agitation rate (rpm)
25	10-45	50, 250, 450	600
40	9-50	80, 150, 550	600
60	9-45	60, 120, 400	600
80	7-50	50, 180, 400	600

Our results indicate that, while retarding crystal growth, Mg^{2+} ions tend to increase the crystal aspect ratio and lead to elongated needle-like crystals (Figure 8-5 and 8-6), which is consistent with past observation reported in the literature[61, 29, 26].

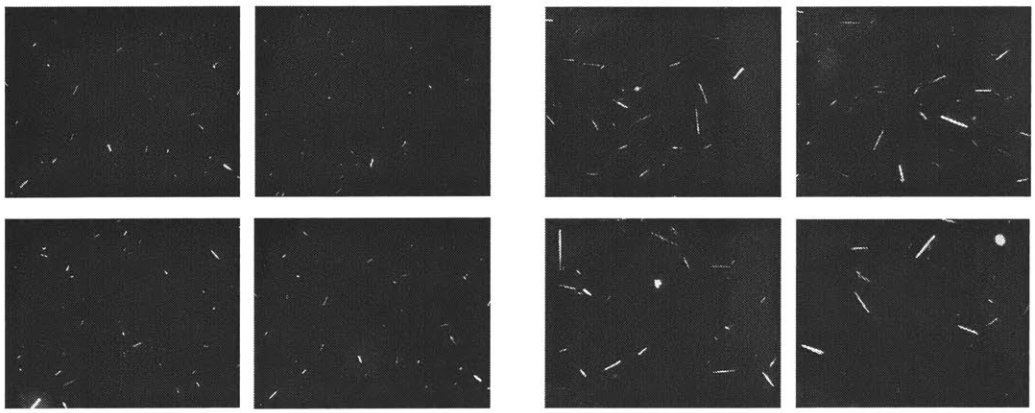

(a) Pure System (b) Mg^{2+}: 55 mg/L

Figure 8-5: $CaSO_4 \cdot 2\,H_2O$ crystal images collected at 80 ℃ from continuous crystallization experiments conducted with Mg^{2+}

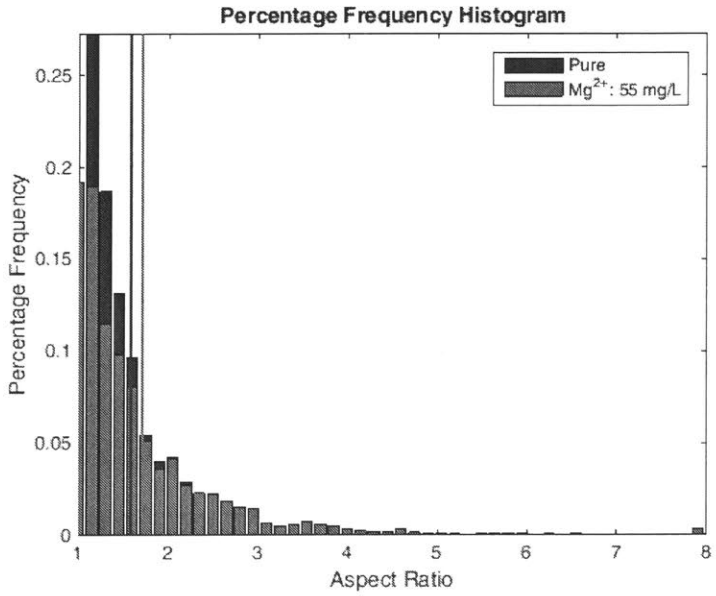

Figure 8-6: Comparison of gypsum crystal aspect ratio distribution with and without the presence of Mg^{2+} at 80 ℃

8.3.1 Model Comparison

Different model forms are tested against experimental data at different temperatures, supersaturation values, and Mg^{2+} amount. The model fitting uses nonlinear least square formulation and is solved using the trust-region-reflective algorithm in Matlab with the constraint that β, the effectiveness factor, are non-negative. The nonlinear regression was carried out using global search (multiple initial guesses) to try to find a solution that is close to the global minimum as much as possible. c_i and c are both in the unit of mg/L. The results we obtained using the Kubota-Mullin and CAM model were shown in figure 8-7 and 8-8. The fitted parameters are summarized in table 8.3 and 8.4.

Table 8.3: Kubota-Mullin's model parameter estimates for G_1 and G_2 in the presence of Mg^{2+}

	model parameters	parameter estimates	units
$\frac{G_1}{G_{10}}$	$Q_{i,\text{diff}}/R$	-2293	Kelvin
	β_{KM}	239.3	Kelvin
$\frac{G_2}{G_{20}}$	$Q_{i,\text{diff}}/R$	-1583	Kelvin
	β_{KM}	91.3	Kelvin

Table 8.4: CAM's model parameter estimates for G_1 and G_2 in the presence of Mg^{2+}

	model parameters	parameter estimates	units
$\frac{G_1}{G_{10}}$	$Q_{i,\text{diff}}/R$	-1849	Kelvin
	$Q_{c,\text{diff}}/R$	-5152	Kelvin
	β_{CAM}	0.68	dimensionless
$\frac{G_2}{G_{20}}$	$Q_{i,\text{diff}}/R$	-1856	Kelvin
	$Q_{c,\text{diff}}/R$	-5121	Kelvin
	β_{CAM}	0.54	dimensionless

Visually, both seem to fit the data reasonably although the Kubota-Mullin model

gives a smaller mean squared error (MSE). Here in CAM, because ionic crystal is formed, c should be referring to the free Ca^{2+} concentration as it directly competes with Mg^{2+} for adsorption sites.

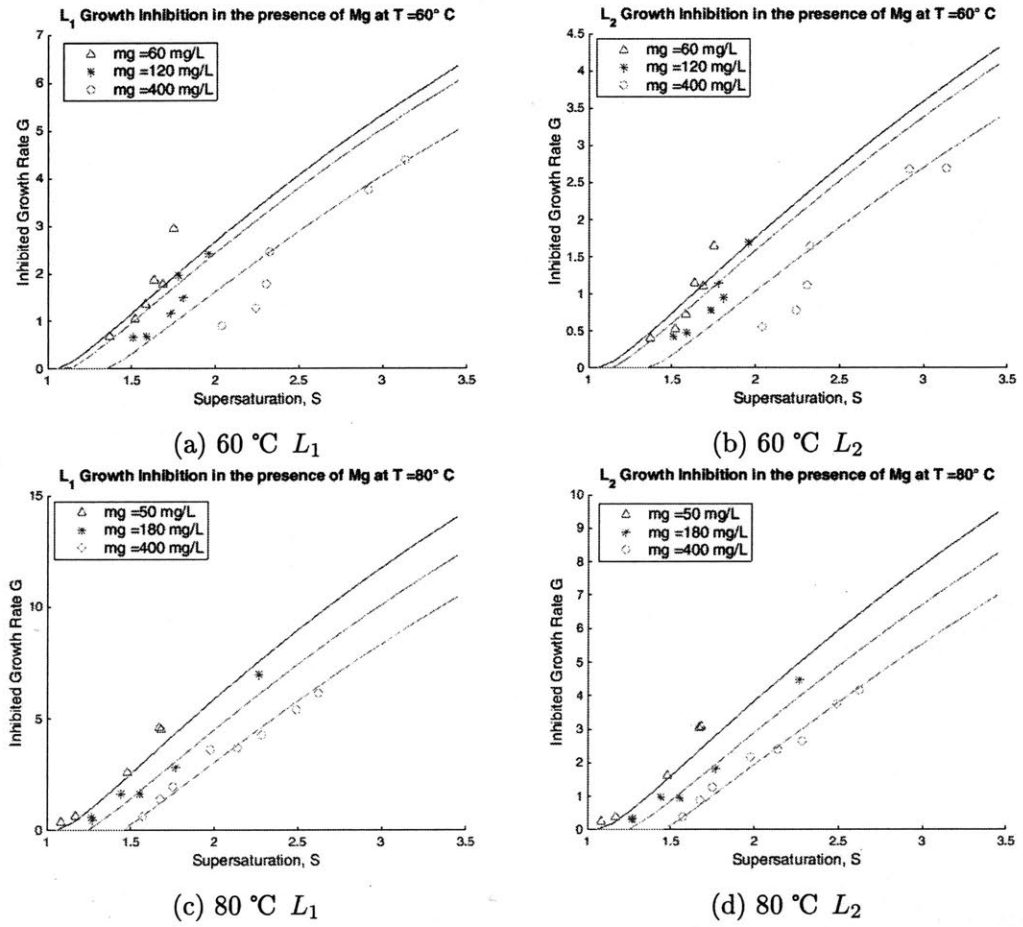

(a) 60 °C L_1

(b) 60 °C L_2

(c) 80 °C L_1

(d) 80 °C L_2

Figure 8-7: Kubota-Mullin growth inhibition model fit for both growth dimensions in the presence of Mg^{2+}

However, if we examine the model fit carefully especially at low supersaturation, we notice that the Kubota model predicts a zero growth rate region below certain supersaturation level. This may indicates no or very slow or minimal growth in real systems to be observed or measured. This critical supersaturation can be found by (8.14) as discussed above. Using the fitted parameters, the threshold supersaturation is plotted in figure 8-9 for each growth dimension. These values are higher at higher magnesium concentration and lower temperature.

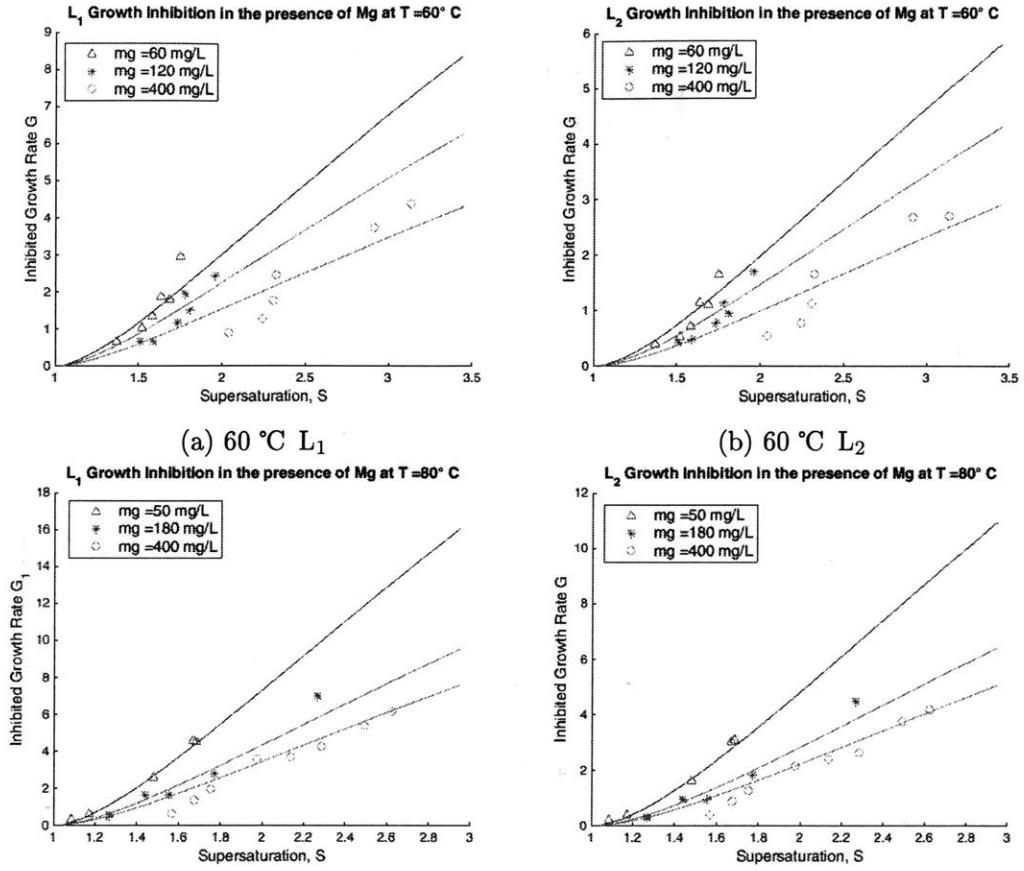

(a) 60 °C L_1

(b) 60 °C L_2

(c) 80 °C L_1

(d) 80 °C , L_2

Figure 8-8: CAM growth inhibition model fit for both growth dimension in the presence of Mg^{2+}

On the other side, CAM only predicts the existence of a growth dead zone when $\beta > 1$. Our model fit suggests that for both dimensions, $\beta < 1$. Therefore, no fully inhibited growth region is predicted.

At this point, with the fitted CAM model, it predicts that the average aspect ratio increases with the amount of impurity in the system at a fixed supersaturation. This is consistent with most of the literature findings.

8.3.2 Measured Impurity Updake

A number of the steady state gypsum solids collected from the MSMPR experiments were further examined to check if any impurity uptake is observed in the crystal

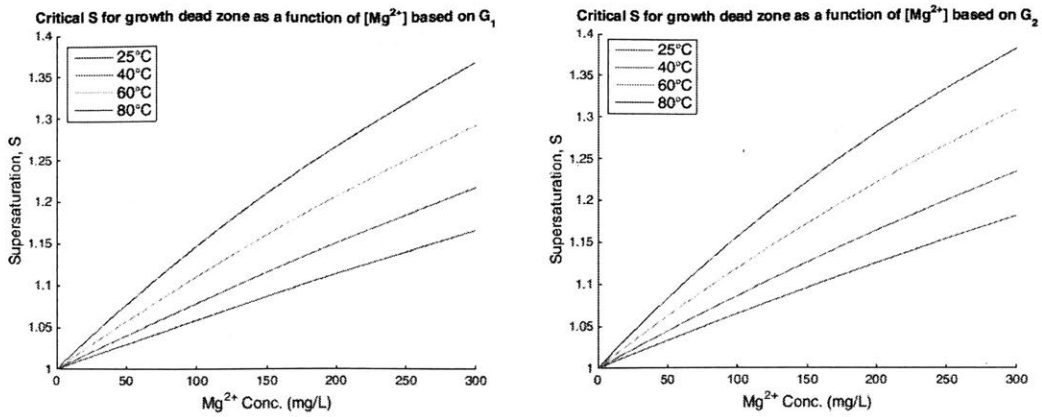

(a) Based on G_1 (b) Based on G_2

Figure 8-9: Critical supersaturation predicted by the fitted Kubota-Mullin model in the presence of Mg^{2+}

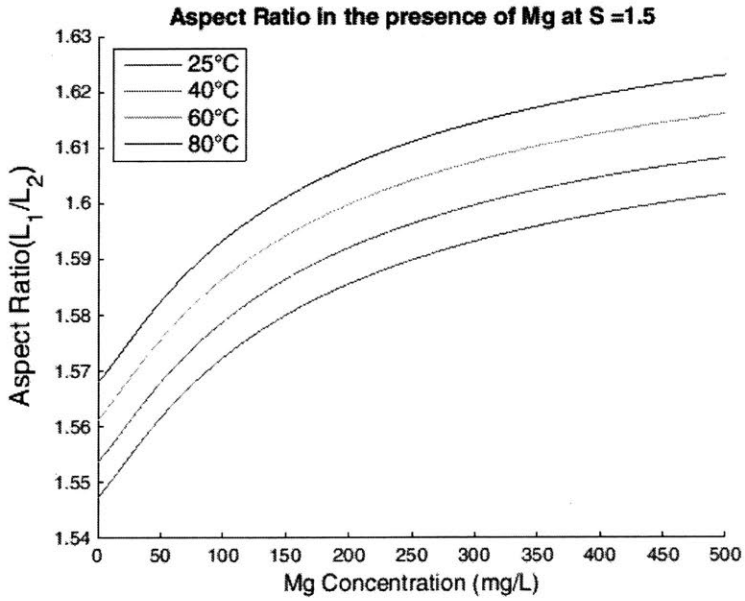

Figure 8-10: Average aspect ratio suggested by CAM growth inhibition model fit at S = 1.5 in the presence of Mg^{2+}

lattice. These solid samples were dissolved and the solution is measured by ICP to check for Mg^{2+} concentration. Table 8.5 summarized the measured Mg^{2+} uptake in gypsum solids in terms of mol/mol Ca^{2+}. Very trace or even undetectable amount of Mg^{2+} is reported. This suggests that incorporation is not likely to be the retarding mechanism for crystal growth for our system.

Table 8.5: ICP measured Mg^{2+} uptake in gypsum solids from MSMPR experiments

Temperature (℃)	$[Mg^{2+}]$ in Feed (mg/L)	Mg^{2+} content in solids (mol/mol Ca^{2+})
25	250	0 (negative measurement)
40	80	0 (negative measurement)
40	150	0.0024
60	150	0 (negative measurement)
80	50	0.0019
80	180	0.0012

8.4 Growth Inhibition Models with Al^{3+}

Al^{3+} is another main impurity ion in the raw phosphate rock which is also present in a relatively abundant amount. Although many studies have been done in understanding its effect in the past[61, 29], there is never a consistent conclusion about its impact on crystal shape. Nevertheless, none of these studies have presented any quantitative results that provides either insights into the mechanism behind or models that can be used to capture growth rate changes. Therefore, experiments were also carried out in a system with single Al^{3+} ions in the entire temperature range up to 80 ℃ with a maximum feed Al^{3+} impurity level of about 650 mg/L. The detailed feed compositions can be found in Table 8.6.

Table 8.6: Feed compositions in wt% for all MSMPR experiments with Al^{3+}

	$Ca(H_2PO_4)_2$	H_2SO_4	P_2O_5	H_2O	$Al(NO_3)_3 \cdot 9H_2O$
$Ca(H_2PO_4)_2$ feed	7.5	–	23.13	69.37	0-1.45
H_2SO_4 feed	–	3.0	24.25	72.75	–

All the experiments carried out were summarized in Table 8.7.

One thing we would like to point out here before testing out different models for Al^{3+} added system is how to correctly identify the amount of free Al^{3+} in solution. This is not an issue for Mg^{2+} added system as Mg^{2+} ions are the dominant (only) magnesium-related species in the solution phase. This means the free Mg^{2+} concentration is always almost the same as the Mg^{2+} added in the feed stream. However,

Table 8.7: Experimental conditions for MSMPR experiments with added Al^{3+}

Temperature (°C)	Residence time (min)	Al^{3+} (mg/L)	Agitation rate (rpm)
25	7-40	115, 250, 550	600
40	7-42	115, 250, 550	600
60	5-37	115, 250, 550	600
80	6-36	115, 250, 550	600

for Al^{3+} added system, the free Al^{3+} concentration in steady state solution is very different from the total amount of Al^{3+} added into the feed stream. In fact, added Al^{3+} ions will mostly bind with SO_4^{2-} ions to form $Al(SO_4)_2^-$ thus the amount og free Al^{3+} ion will be much smaller comparing to the total Al^{3+} added into the feed stream. This is plotted in figure 8-11.

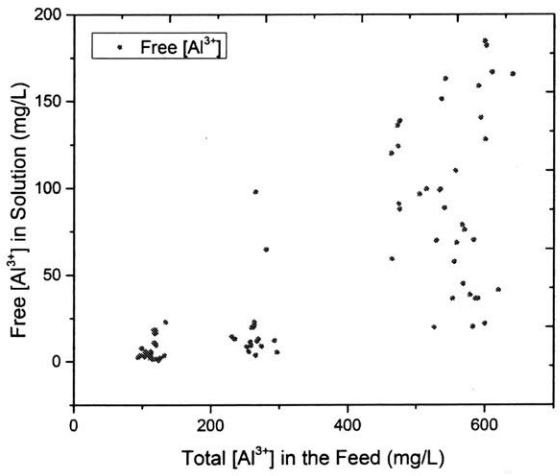

Figure 8-11: Free Al^{3+} concentration in steady state solution compared to the total Al^{3+} in the feed from all runs

This is very important as the models we discussed above all makes use of the adsorption isotherm which needs the free impurity ion concentration in the bulk solution. Physically, only the free Al^{3+} ions would be pinning or attaching onto the kink sites and cause a retardation in the crystal growth, while $Al(SO_4)_2^-$ ions won't. This might be the reason that contradicting results regarding Al^{3+}'s effects were

presented in the literature as none of these studies ever correctly identifies the true free Al^{3+} concentration. They have always been using the total Al^{3+} concentration based on the amount added to the solution. Here, because of the thermodynamic models we used, we were able to find the free Al^{3+} concentration in the supersaturated solution. This will be the c_i we use in fitting inhibition model parameters.

8.4.1 Model Comparison

Different model forms are tested against experimental data at different temperatures, supersaturation values, and free Al^{3+} amount. the same fitting algorithm is used here. The results we obtained using the Kubota-Mullin and CAM model were shown in figure 8-12 and 8-13. The fitted parameters are summarized in table 8.8 and 8.9.

Table 8.8: Kubota-Mullin's model parameter estimates for G_1 and G_2 in the presence of Al^{3+}

	model parameters	parameter estimates	units
$\frac{G_1}{G_{10}}$	$Q_{i,\text{diff}}/R$	-2097	Kelvin
	β_{KM}	239.3	Kelvin
$\frac{G_2}{G_{20}}$	$Q_{i,\text{diff}}/R$	-489	Kelvin
	β_{KM}	91.3	Kelvin

Table 8.9: CAM's model parameter estimates for G_1 and G_2 in the presence of Al^{3+}

	model parameters	parameter estimates	units
$\frac{G_1}{G_{10}}$	$Q_{i,\text{diff}}/R$	-84.06	Kelvin
	$Q_{c,\text{diff}}/R$	-5152	Kelvin
	β_{CAM}	0.43	dimensionless
$\frac{G_2}{G_{20}}$	$Q_{i,\text{diff}}/R$	-380.42	Kelvin
	$Q_{c,\text{diff}}/R$	-5121	Kelvin
	β_{CAM}	0.434	dimensionless

Visually, both seem to fit the data reasonably although the Kubota-Mullin model gives just a slightly smaller MSE. Here in CAM, because ionic crystal is formed, c should be referring to the free Ca^{2+} concentration as it directly competes with Al^{3+} for adsorption sites. Because as we mentioned above, incorporation is not the mechanism, therefore Al^{3+} will not permanently stays in the surface thus it won't cause the lattice structure to change due to charge balance.

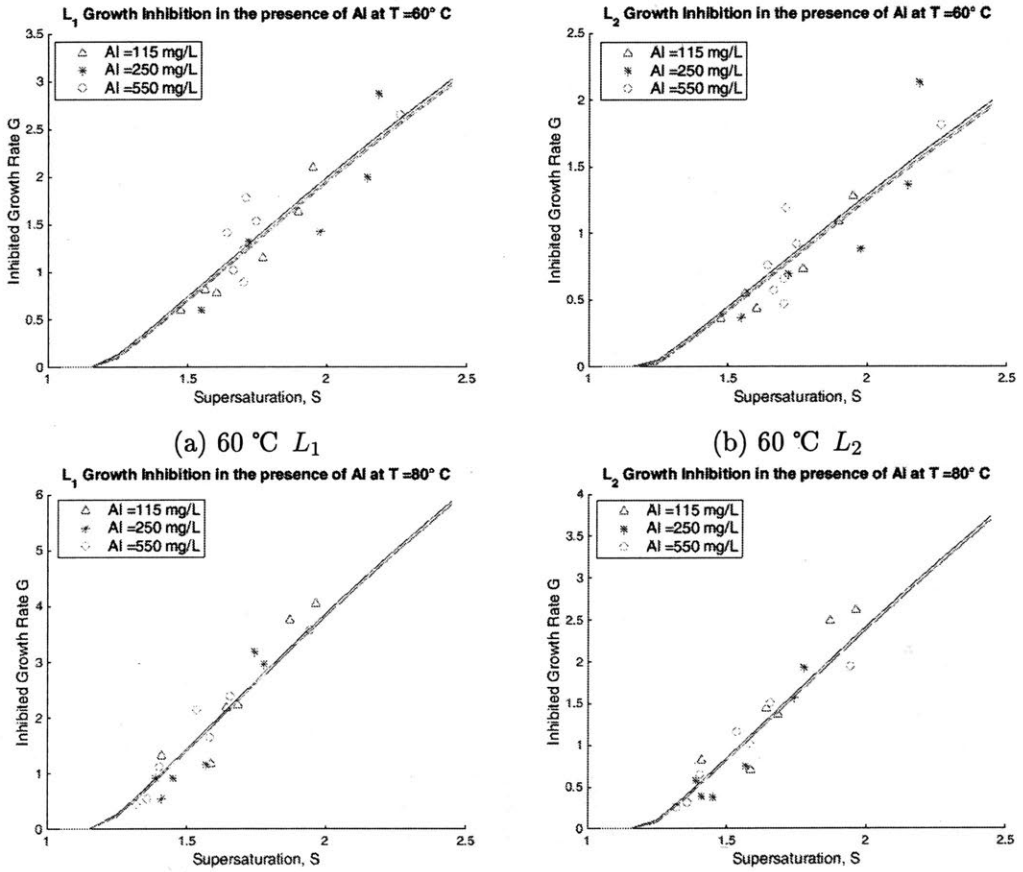

(a) 60 °C L_1 (b) 60 °C L_2

(c) 80 °C L_1 (d) 80 °C L_2

Figure 8-12: Kubota-Mullin growth inhibition model fit for both growth dimensions in the presence of Al^{3+}

Here, both model fit shows the impurity adsorption equilibrium constant K_i shows relatively small temperature dependency ($Q_{\text{i,diff}}$ is relatively small). This means K_i is almost a constant and it is big. Therefore, when c_i is relatively large, the equilibrium surface coverage θ_s will be close to 1. Only when c_i is very small, θ_s will be less

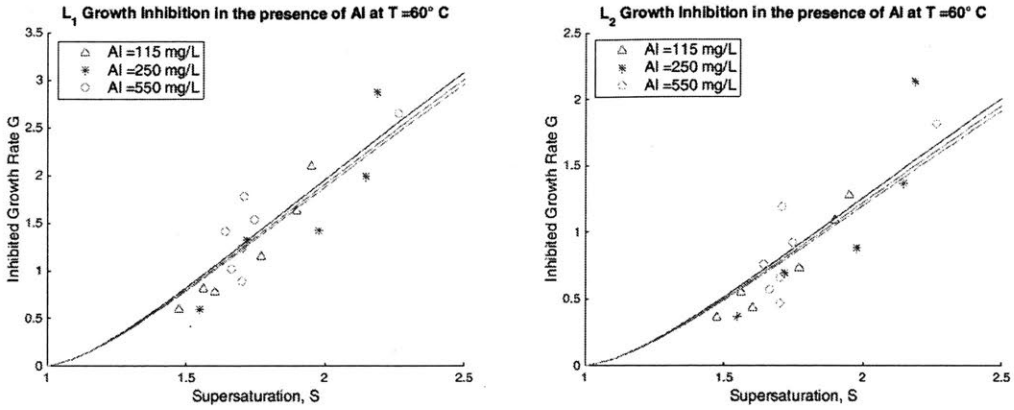

(a) 60 °C L_1

(b) 60 °C L_2

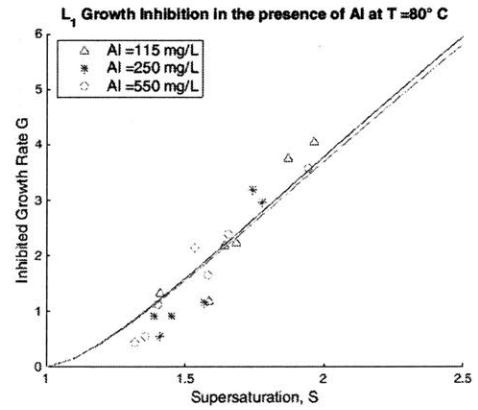

(c) 80 °C L_1

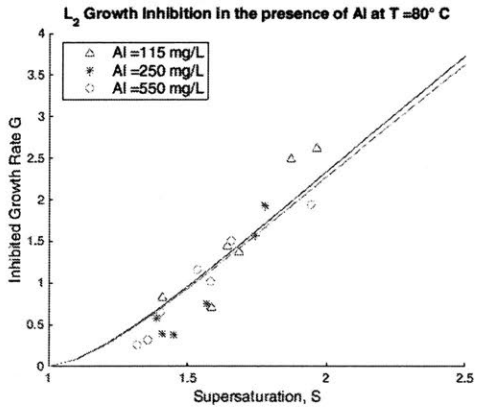

(d) 80 °C , L_2

Figure 8-13: CAM growth inhibition model fit for both growth dimension in the presence of Al^{3+}

than 1. This is also reflected in the plots where the amount of impurity does not change the model fit by much. This might due to the fact that even we varied the feed aluminum concentration, the free Al^{3+} in the solution is much smaller and are very close to each other from run to runs.

Again, if we examine the model fit carefully especially at low supersaturation, we notice that the Kubota model still predicts a zero growth rate region below certain supersaturation level. This may indicates no or very slow or minimal growth in real systems to be observed or measured. This critical supersaturation can be found by (8.14) as discussed above. Using the fitted parameters, the threshold supersaturation is plotted in figure 8-14 for each growth dimension. These values are higher at lower

temperature. Because K_i is mostly 1 in this case, the critical supersaturation does not vary much at when $c_i >> 1$.

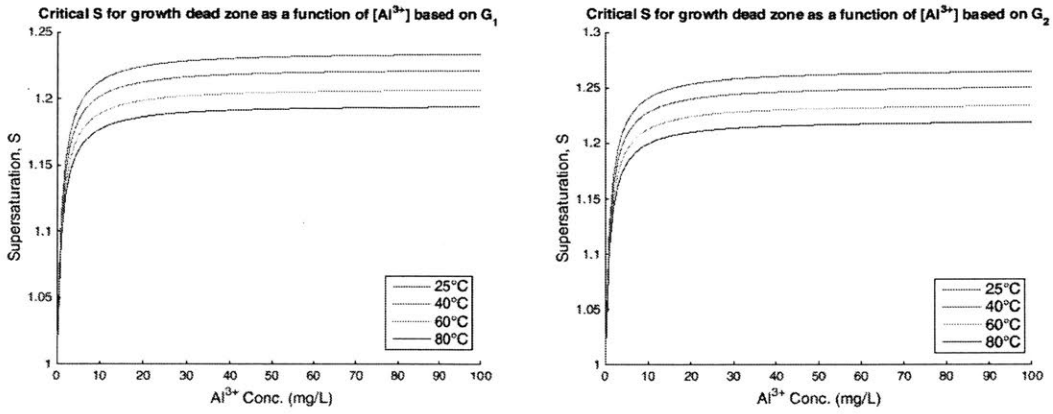

(a) Based on G_1 (b) Based on G_2

Figure 8-14: Critical supersaturation predicted by the fitted Kubota-Mullin model in the presence of Al^{3+}

On the other side, CAM only predicts the existence of a growth dead zone when $\beta > 1$. Our model fit suggests that for both dimensions, $\beta < 1$. Therefore, no fully inhibited growth region is predicted.

At this point, with the fitted CAM model, it predicts that the average aspect ratio increases with the amount of impurity in the system at a fixed supersaturation.

Also, if we plot the average aspect ratio change with impurity predicted from both models, we find that the Kubota-Mullin model predicts the change to be bigger than the CAM model at low impurity concentration while the reverse is observed at higher impurity concentration.

8.5 Growth Dead Zone

From a modeling perspective, the concept of this "dead zone" can be contradictory from higher dimensional analysis. When crystals are modeled by two characteristic lengths, the critical supersaturation must be the same for all crystal faces, otherwise in regions where one dimension is inhibited but not the other, crystals will be predicted to have infinite aspect ratio. This is not physical in real systems. However, if we try to

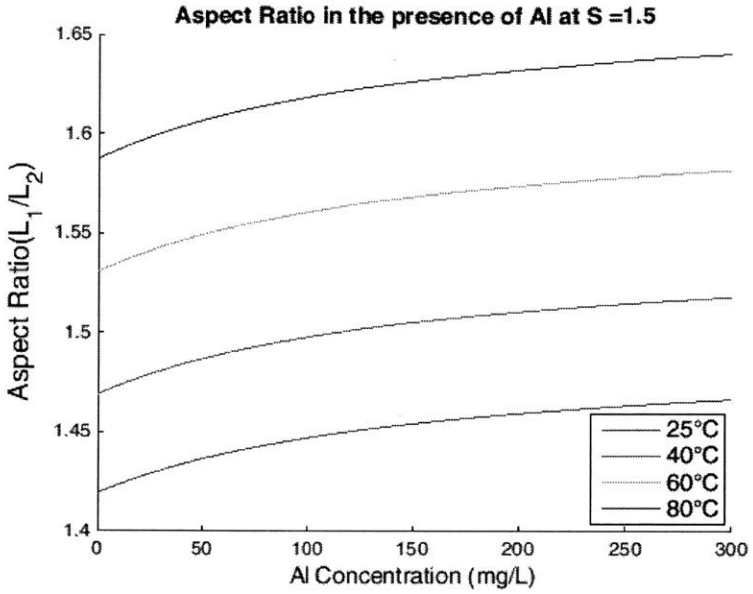

Figure 8-15: Average aspect ratio suggested by CAM growth inhibition model fit at S = 1.5 in the presence of Al^{3+}

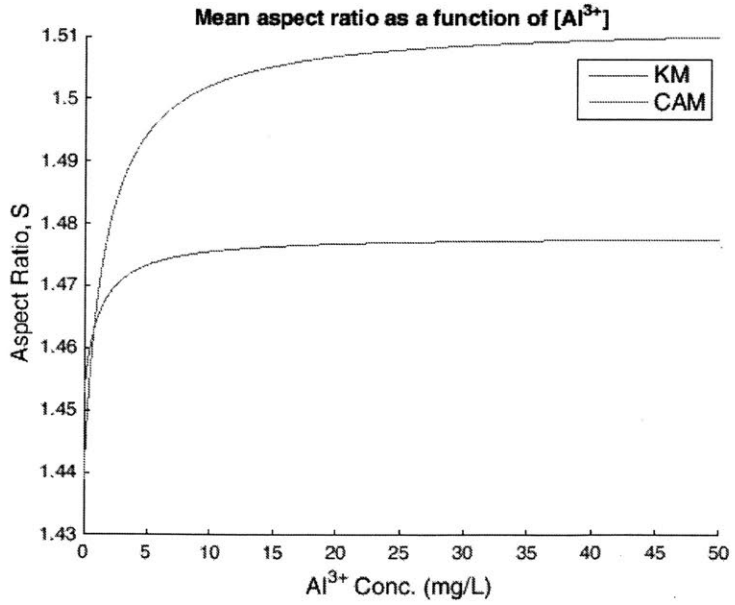

Figure 8-16: Average aspect ratio suggested by KM and CAM growth inhibition model fit at S = 1.5 and T = 60 °C in the presence of Al^{3+}

force the critical supersaturation on both growth dimensions to be the same, the fitting parameters for the Kubota-Mullin model would become identical on both growth

directions and therefore the same extent of crystal growth inhibition is expected. In this case, the Kubota-Mullin model cannot predict varying crystal aspect ratio observed at different impurity concentration. Here, we plot the Kubota-Mullin model predicted critical supersaturation for both dimensions on the same graph. We can see for both Mg^{2+} added and Al^3 added system, this threshold value does not match for the two growth dimension. Therefore, when solution supersaturation falls in between the gap ($\sigma_{c,1} < \sigma < \sigma_{c,2}$), this model would predict crystals to growth into infinitely long needles.

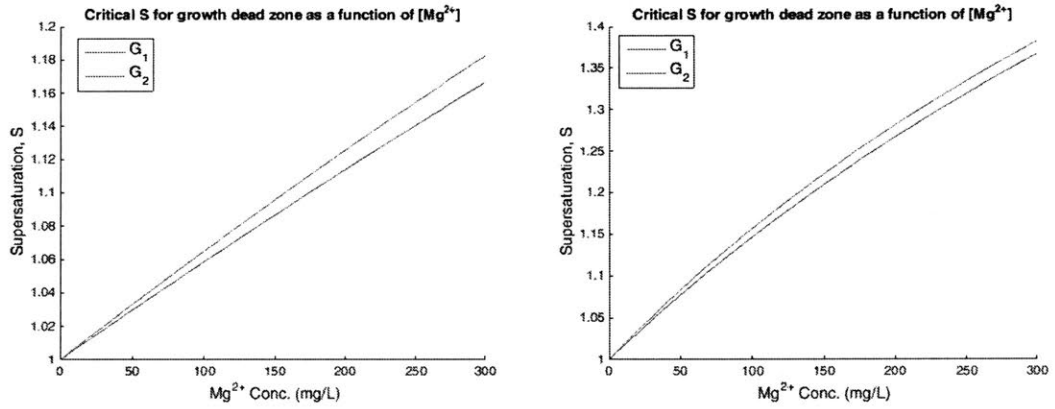

(a) 25 °C (b) 80 °C

Figure 8-17: Critical supersaturation predicted by the fitted Kubota-Mullin model in the presence of Mg^{2+}, both dimensions

Other empirical evidence also suggests that for calcite crystal, which is similar to gypsum, no total step stoppage was observed from addition of magnesium ions even at high concentration. [7] Therefore, our hypothesis is that growth should not completely be stopped under supersaturated solution, and the observed no growth is a manifestation of extremely slow growth. To test this hypothesis, we carried out seeded batch crystallization experiments at predicted inhibition region to check if growth can be physically observed. Magnesium ions were used as the impure particles.

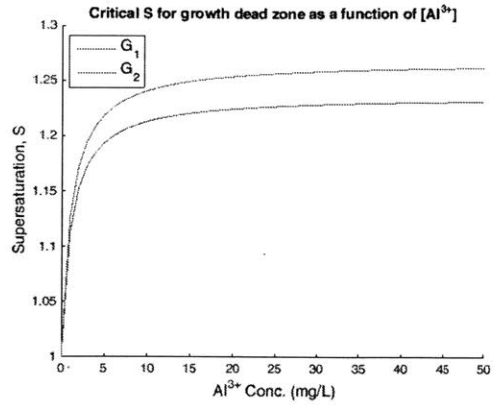

(a) 25 °C

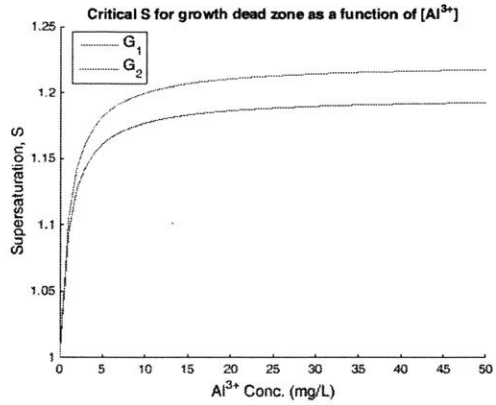

(b) 80 °C

Figure 8-18: Critical supersaturation predicted by the fitted Kubota-Mullin model in the presence of Al^{3+}, both dimensions

8.5.1 Seeded Batch Crystallization

Seeded batch crystallization experiments were carried out at predicted growth dead region by the Kubota-Mullin Model to test its physical validity. Three experiments with no, low and high magnesium were conducted at 25 and 80 °C respectively. For all three batch runs at a fixed temperature, the solutions were prepared so that the supersaturation ratio (S) is almost the same. This not only ensures that we operate in the inhibited region if a growth dead zone exists but also minimizes nucleation since supersaturation is low. Gypsum crystals were added to the solutions at the beginning of the experiment. All solutions were kept at a constant temperature with overhead mechanical agitation to ensure good mixing. Throughout the experiment, FBRM is used to monitor the size distribution changes for the seeded crystals. Experimental conditions for all runs were summarized in table 8.10.

Table 8.10: Solution compositions and conditions for zero growth experiments

	25 °C			80 °C		
(wt%)	Pure	Mg^{2+} (180 mg/L)	Mg^{2+} (30 mg/L)	Pure	Mg^{2+} (180 mg/L)	Mg^{2+} (30 mg/L)
$Ca(H_2PO_4)_2$	1 %	0.95%	1 %	2 %	1.9%	2 %
H_2SO_4	0.6 %	0.6%	0.6 %	1.2 %	1.2%	1.2 %
P_2O_5	25%	25%	25 %	25 %	25%	25%

8.5.2 Zero Growth Tests

Seeded crystal chord length distribution is monitored throughout the batch crystallization experiments to determine if growth phenomena has occurred. For all six runs (table 8.10), the chord length distribution is found to shift right which indicates crystal growth has been taking place under the given solution condition. This shift is less obvious for 25 ℃ as growth rate is smaller at lower temperature but still observable. This indicates even with the presence of Mg^{2+} ions, growth is barely inhibited at low supersaturation. Thus the predicted growth dead zone by the Kubuta-Mullin model does not exist for our system. In the limiting case of high impurity concentration, growth tends to approach a fixed value at given temperature rather than being fully inhibited.

Table 8.11: Growth results from zero growth experiments

	25 ℃			80 ℃		
	Pure	Mg^{2+} (30 mg/L)	Mg^{2+} (180 mg/L)	Pure	Mg^{2+} (30 mg/L)	Mg^{2+} (180 mg/L)
S	1.156	1.165	1.162	1.041	1.064	1.051
S_c	1.0	1.043	1.26	1.0	1.04	1.14
Expected	Yes	Yes	No	Yes	Yes	No
Observed	Yes	Yes	Yes	Yes	Yes	Yes

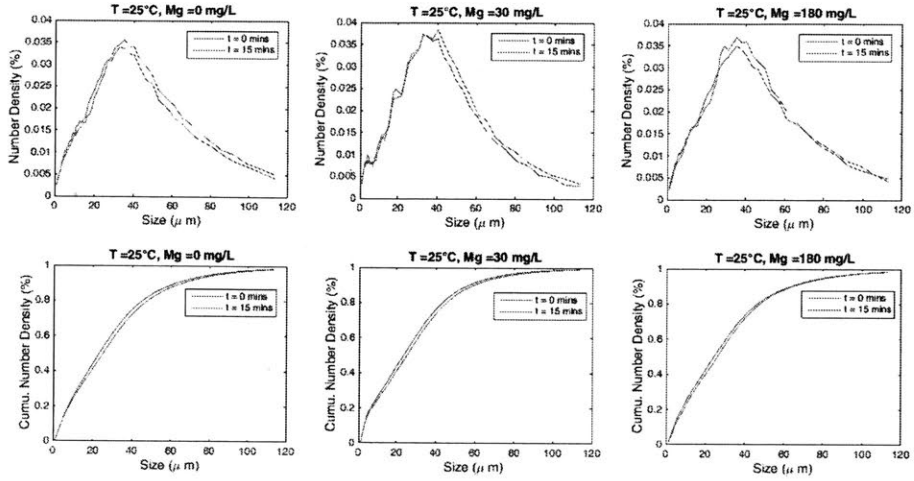

Figure 8-19: FBRM measured chord length distribution at $t = 0$ and $t = 15$ mins for all 3 seeded batch crystallization runs at 25 °C. Top: number density; Bottom: cumulative number density.

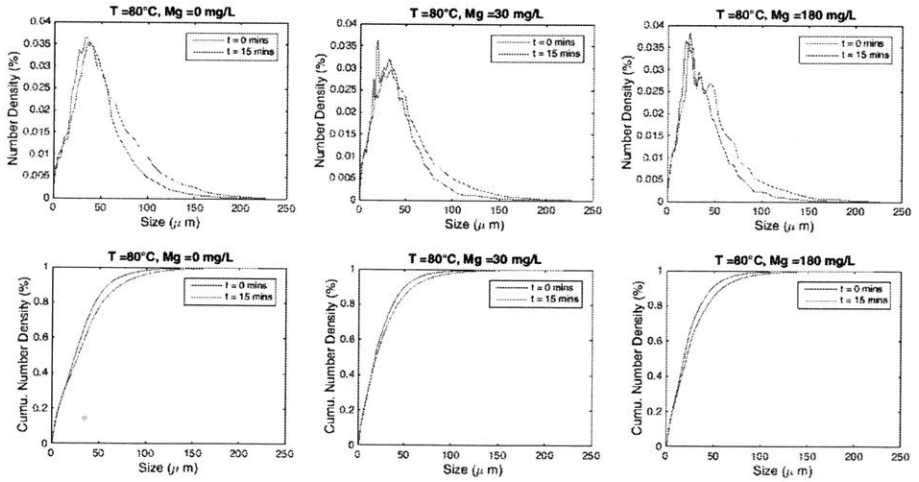

Figure 8-20: FBRM measured chord length distribution at $t = 0$ and $t = 15$ mins for all 3 seeded batch crystallization runs at 80 °C. Top: number density; Bottom: cumulative number density.

Chapter 9

Effect of Competing Impurities on Crystal Growth

In the precious chapter, we looked at the effect of single impurity, where only one type of foreign particle is assumed to be present in the system. However, in the raw phosphate rock, there are a number of different metal ions that will enter the acid solution during reactive crystallization and they all play a role in modifying gypsum crystal shape and size distributions. Therefore, it is important to look at the combined effects from multiple impurities. Most of the time, the previously discussed inhibition models can be generalized easily to account for the presence of multiple impurities. Here we conducted experiments with added Mg^{2+} and Al^{3+} ions simultaneously and used these measurements to verify the generalized inhibition models.

9.1 Crystal Growth in the Presence of Multiple Impurities

When two different types of impure particles are present in the growth medium, namely, A and B, they both will be adsorbed onto the surface terrace and then migrate through the surface and incorporate into kinks and steps to block the growth of crystal lattice. One immediate effect is the change of available kink sites due to the

adsorption of both impurity particles. This change thus affect the resulting growth rate and the effect of competing impurities will be discussed from both the stepping pinning mechanism framework in terms of the Kubota-Mullin model as well as the competitive adsorption framework.

9.1.1 Generalized Kubota-Mullin Model

When there are two competing foreign particles, denoted as A and B, the average distance L between the adjacent absorbed impurity is expected to be smaller comparing to when only one of the impurity ion is present . Now this L terms can be found as

$$\frac{1}{L} = \frac{1}{L_A} + \frac{1}{L_B} \tag{9.1}$$

where L_A and L_B refers to the average distance between adjacent absorbed impurity particle A and B respectively when only A or B is present. Now we can directly apply equation (8.6) to find the new linear coverage of total impurity in this case:

$$\theta_l = \frac{x_0}{L} = x_0(\frac{1}{L_A} + \frac{1}{L_B}) = \theta_{A,l} + \theta_{B,l} \tag{9.2}$$

Then we can directly substitute the above equation to the most general Kubota-Mullin equation as shown in (8.7) and we found that

$$\frac{v}{v_0} = 1 - r_c/x_0\theta_l = 1 - \alpha_l\theta_l \tag{9.3}$$

$$= 1 - \alpha_l(\theta_{A,l} + \theta_{B,l}) \tag{9.4}$$

Now only if we know $\theta_{A,l}$ and $\theta_{B,l}$, we have the generalized Kubota-Mullin model that can describe the inhibited growth rate when two competing impurities are present. This is easy as the linear coverage should still be equal to the surface coverage $\theta_{A,s}$ and $\theta_{B,s}$. Surface coverage can be found directly from the multi-component Langmuir

isotherm

$$\theta_{A,s} = \frac{K_A c_A}{K_A c_A + K_B c_B + 1} \tag{9.5}$$

$$\theta_{B,s} = \frac{K_B c_B}{K_A c_A + K_B c_B + 1} \tag{9.6}$$

where c_A and c_B is the corresponding impurity concentration. K_A and K_B follows the form as given in equation (8.10). Now we find the final generalized Kubota-Mullin form commonly presented in the literature as [65]

$$\frac{G}{G_0} = 1 - \alpha_l \left(\frac{K_A c_A + K_B c_B}{1 + K_A c_A + K_B c_B}\right) \tag{9.7}$$

$$\alpha_l = \frac{\gamma a}{k_B T x_0 \sigma} = \frac{\beta_{\mathrm{KM}}}{\sigma T} \tag{9.8}$$

9.1.2 Generalized Competitive Adsorption Model

Alternatively, the competitive adsorption model assume when there is presence of impurity, the density of absorbed solute molecules on the surface n_s approaches $n_{se}(1-\theta_l)$ and growth rate is proportional to n_s according to the BCF model. Therefore, when two competing impurities are present, $n_{se}(1 - \theta_l$ becomes $n_{se}(1 - \theta_{A,l} - \theta_{B,l})$. Therefore, the generalized CAM can be easily derived as

$$\frac{G}{G_0} = 1 - \theta_{A,l} - \theta_{B,l} \tag{9.9}$$

$$= 1 - \beta_A \theta_{A,s} - \beta_B \theta_{B,s} \tag{9.10}$$

Substitute the competitive multicomponent Langmuir isotherm,

$$\theta_A = \frac{K_A c_A}{K_A c_A + K_B c_B + Kc + 1} \tag{9.11}$$

$$\theta_B = \frac{K_B c_B}{K_A c_A + K_B c_B + Kc + 1} \tag{9.12}$$

$$\tag{9.13}$$

we find the final form as

$$\frac{G}{G_0} = 1 - \beta_A \frac{K_A c_A}{K_A c_A + K_B c_B + Kc + 1} - \beta_B \frac{K_B c_B}{K_A c_A + K_B c_B + Kc + 1} \tag{9.14}$$

$$= 1 - \frac{\beta_A K_A c_A + \beta_B K_B c_B}{K_A c_A + K_B c_B + Kc + 1} \tag{9.15}$$

9.2 Continuous Crystallization Experiments with Impurities

Materials For all experiments, reagent-grade calcium phosphate monobasic $Ca(H_2PO_4)_2$, sulfuric acid H_2SO_4 (96 wt%), phosphoric acid H_3PO_4 (85 wt%, 99.99 % trace metal basis) magnesium oxide MgO and aluminum nitrate nonahydrate ($Al(NO_3)_3 \cdot 9\,H_2O$) were purchased from Sigma-Aldrich. Ultrapure water was used for solvent dilution.

Experimental Setup A schematic diagram of the experimental setup is shown in Figure 6-1. The setup was designed to simulate wet phosphoric acid production with the presence of combined impurity ions. Magnesium oxide and aluminum nitrate nonahydrate is added together to the calcium phosphate monobasic feed stream to introduce Mg^{2+} and Al^{3+} impurity simultaneously. The same procedure and sample characterization method is adopted here as used in the 2D study for the pure system. Different steady states can be achieved by manipulating the residence time of the reaction system through adjusting the flowrate of the feed solutions. Each steady-state liquid sample is analyzed by ICP to obtain accurate total Ca, S, P, Mg and Al concentrations. The steady-state saturation ratio defined in (2.18) can then be computed using the MSE thermodynamic model by providing the ICP-measured solution composition. Images of steady-state gypsum crystals are collected through an automated moving-stage microscope to make sure about 10,000 to 20,000 single crystal samples are captured for each experimental run. A multi-scale image analysis algorithm is then applied to obtain the resulting 2D size distribution.

9.3 Growth Inhibition Models with Mg^{2+} and Al^{3+}

Now without requiring any additional fitting, we can directly make use of the results we obtained for the single impurity inhibition model and extend that to predict growth in the presence of both Mg^{2+} and Al^{3+} ions.

The detailed feed compositions can be found in Table 9.1.

Table 9.1: Feed compositions in wt% for all MSMPR experiments with Mg^{2+}

	$Ca(H_2PO_4)_2$	H_2SO_4	P_2O_5	H_2O	MgO	$Al(NO_3)_3 \cdot 9H_2O$
Ca Feed	7.5	–	23.13	69.37	0-0.15	0-1.3
H_2SO_4 Feed	–	3.0	24.25	72.75	–	–

All the experiments carried out were summarized in Table 9.2.

Table 9.2: Experimental conditions for MSMPR experiments with added Mg^{2+} and Al^{3+}

Temperature (°C)	Residence time (min)	Mg^{2+} (mg/L)	Al^{3+} (mg/L)	Agitation rate (rpm)
25,40,60,80	15	140	300	600
25,40,60,80	15	250	500	600
25,40,60,80	15	450	400	600

Parity plots showing model prediction against measured growth rates for both the generalized Kubota-Mullin Model and Competitive adsorption model are presented in Figure 9-1 and 9-2. Both model gives reasonable prediction although the Kubota-Mullin Model performance is slightly better. However, with the presence of growth deadzone, CAM model might be the more appropriate choice.

Lastly, we plotted both model prediction against supersaturation at different levels of impurity concentration. For all cases, the addition of a second impurity retard the growth process further and the reduced amount always tend to approach a fixed value at high impurity rather than leading to full inhibition where growth will becomes zero. This again indicates our impurity particles are mobile rather than immobile, therefore it will never inhibit growth completely.

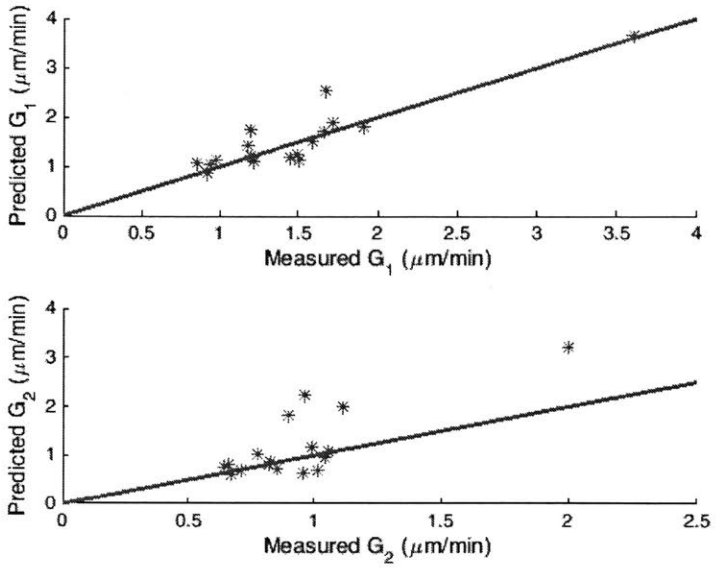

Figure 9-1: Comparison of generalized Kubota-Mullin model prediction versus experimental measured growth rates for both dimensions

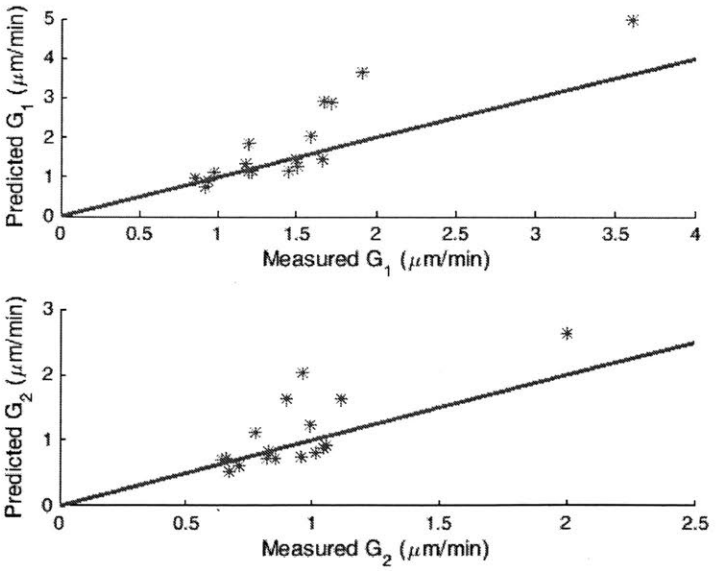

Figure 9-2: Comparison of generalized Kubota-Mullin model prediction versus experimental measured growth rates for both dimensions

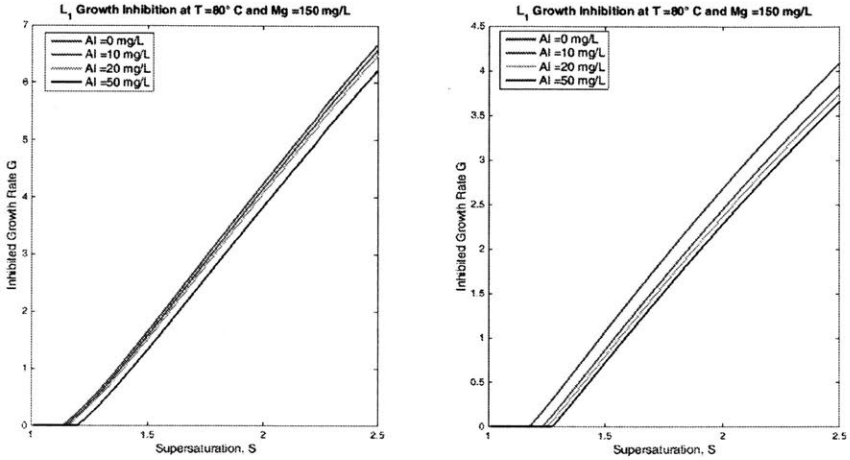

Figure 9-3: Generalized Kubota-Mullin model prediction at a fixed Mg^{2+} level

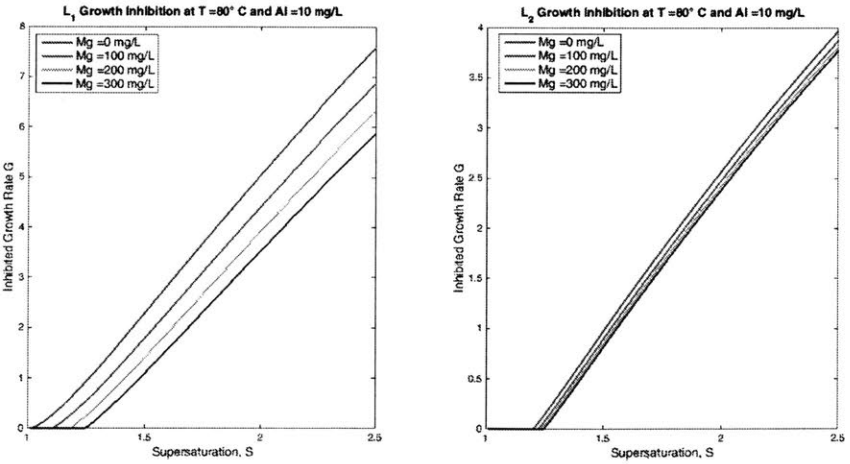

Figure 9-4: Generalized Kubota-Mullin model prediction at a fixed Al^{3+} level

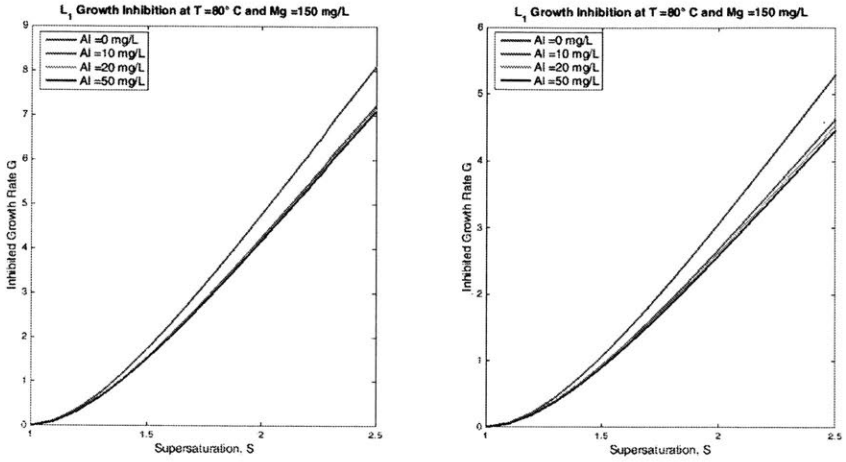

Figure 9-5: Generalized CAM model prediction at a fixed Mg^{2+} level

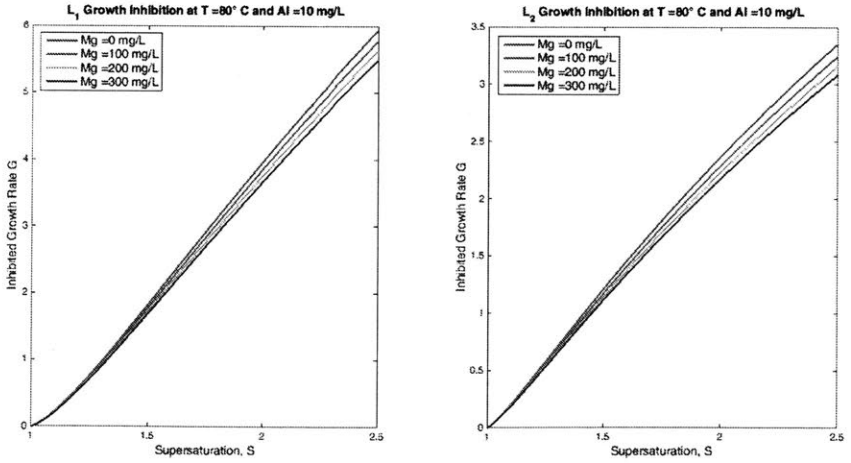

Figure 9-6: Generalized CAM model prediction at a fixed Al^{3+} level

Part IV

Conclusions and Suggestions for Future Work

THIS PAGE INTENTIONALLY LEFT BLANK

Chapter 10

Conclusions and Future Outlook

10.1 Summary of Contributions

This project tries to study the effect of metal ion impurities on the reactive crystallization process of gypsum during phosphoric acid production. More specifically, we aim to quantify their impact on crystal shape and size distributions. In order to achieve this purpose, population balance equation is used to model the entire process at any given operating conditions. To make use of PBM, we tried to understand both impurity's thermodynamic (alteration of solution speciation) and kinetic effects (retarding growth) individually.

Past work on ionic crystallization in electrolyte solutions usually only focus on the study of crystal growth and nucleation kinetics. Also, they did not use the correct definition of supersaturation when fitting kinetic parameters. The high concentrations in this multicomponent electrolyte system implies that supersaturation should be written in terms of the solubility product ratio. This thus requires the use of proper thermodynamic models that can capture solution non-ideality and has the power to enable the computation of activity coefficients as well as free ion concentrations. In this work, the mixed solvent electrolyte (MSE) model is utilized due to its ability to predict solution speciation. The MSE model is a first-principles model that determines solid-liquid equilibrium by calculating excess Gibbs energy from additive pairwise interactions. The key for utilizing this model it to capture the main pairwise

interactions related to the dominant solution complexes. Therefore, we collected both literature and experimental solubility data to carry out regression analysis to fill the missing interactions that are relevant to our system. We started by analyzing the base system first and then added impurity's effect on top of that. This is done for all relevant impurity ions such as Mg^{2+}, Al^{3+}, Fe^{3+}, K^{+}, Na^{+}, etc. The final model with all the fitted interaction parameters added is verified against collected gypsum solubility data when all impurities are present and it shows good agreement. With this model, we can properly quantify supersaturation at any given conditions.

Continuous reactive crystallization experiments are first carried out without additives using a mixed-suspension, mixed-product removal (MSMPR) crystallizer until it reaches steady state. Liquid and solid samples are collected at steady state for measuring solution composition and crystal size distribution. The solution composition is then fed into the MSE model for proper computation of supersaturation at given temperature while the crystal size distribution is converted to find out the corresponding growth rate. Different steady state conditions are imposed to acquire both the temperature and supersaturation dependency of the crystallization kinetics by adjusting the feed stream flowrate and chiller temperature. One-dimensional growth model was first developed for temperature range from 25 to 60 °C. However, it was then found out to be unable to capture the increasing aspect ratio at even higher temperature. A two-dimensional growth model with dispersion is then developed in order to capture this needle-like crystal morphology and the varying crystal aspect ratio with temperature, which is made possible by performing multi-scale image segmentation and edge detection using the canny method. Nucleation rate is found to have a first order dependency on supersaturation as well as the total number of particles. Numerical results are obtained for the base system kinetics.

Similar MSMPR experiments were carried out with the presence of single impurities, namely, Mg^{2+} and Al^{3+} ions. Both the Kubota-Mullin and competitive adsorption growth inhibition models are tested with experimental results for their validity. They both show reasonable fitting against measurements although Kubota-Mullin gives slightly smaller MSE. However, the main distinction between these two models

are the existence of a growth dead zone below certain critical supersaturation. While Kubota-Mullin always predict such a region, CAM only predicts the appearance of a growth dead zone for very mobile impurity ions (when $\beta > 1$). We carried out zero growth experiments at supersaturation below the threshold value and observed growth behavior. Also, from a higher dimensional perspective, it is not feasible to have a non-matching growth dead region for each growth dimension as this would lead to crystals with infinite aspect ratios in certain supersaturation regime. Therefore, it is likely that CAM model is more suitable in describing the growth inhibition behavior for our system. Lastly, generalized inhibition models are derived for systems with competing impure particles and the parameter values obtained from single impurity study are used directly for predicting growth rates when two impurities are present. The model again gives reasonable prediction comparing to the measured growth rates.

In summary, the key contributions in this work are (1) introduced proper definition of supersaturation for concentrated electrolyte system to be used in kinetic rate equations (2) made use of the MSE model framework that enables proper supersaturation calculation (3) quantitatively accounted for the effect of impurity on solution speciation (4) provided numerical results on gypsum crystallization kinetics in phosphoric acid solution in a two-dimensional framework to account for shape changes (5) tested and compared different growth inhibition models to quantify impurity's kinetic effect (6) extended the single impurity results to multi-component system. The work presented here builds the foundation for future study of the effect from other impurity ions. This study goes beyond past studies by providing a full two-dimensional kinetic model for a highly concentrated ionic system that includes crystallization kinetics and thermodynamically correct driving force accounting non-ideality as well as the effects of impurities. The results from this study represent the leading edge in modeling the effect of impurities in the crystallization of gypsum during the production of phosphoric acid.

10.2 Suggestions for Future Work

10.2.1 Filtration Study

In order to perform overall process optimization (i.e., maximize filtration efficiency), it is also important to study the relationship between the crystal size distribution and cake permeability. Most existing models describe permeability as a function of porosity (ϵ)and the first, second, and third moments of the size distribution

$$\kappa \propto f(\epsilon) D_p^2$$

where D_p refers to the mean particle size and it is defined as

$$D_p = \frac{\mu_{i+1}}{\mu_i}$$

where μ_i refers to the ith moment of particle size distribution. This is essentially by combining the Carman-Kozeny (CK) equation, which is used to describe the pressure drop of a fluid flowing through a packed bed of solids with Darcy's law.

$$\kappa = a\frac{\epsilon^3}{(1-\epsilon)^2} D_p^2$$

$$\kappa = \frac{\mu L}{\Delta P A}\frac{dV}{dt} \text{ (Darcy's Law)}$$

We did some preliminary study to find what type of filtration model is suitable to predict gypsum cake permeability based on it crystal size distribution. Buchner funnel filtration experiments [50] were conducted to record the average filtrate rate for a given cake. We simply pour water through a pre-made incompressible cake so the porosity is fixed during filtration experiments. Therefore, based on Darcy's law, we would expect filtrate volume to change linearly with time. This is exactly what is observed as shown in Figure 10-1. Here, results from only a few runs were plotted. Thus, we can use Darcy's law to compute cake permeability from the measured average filtrate rate.

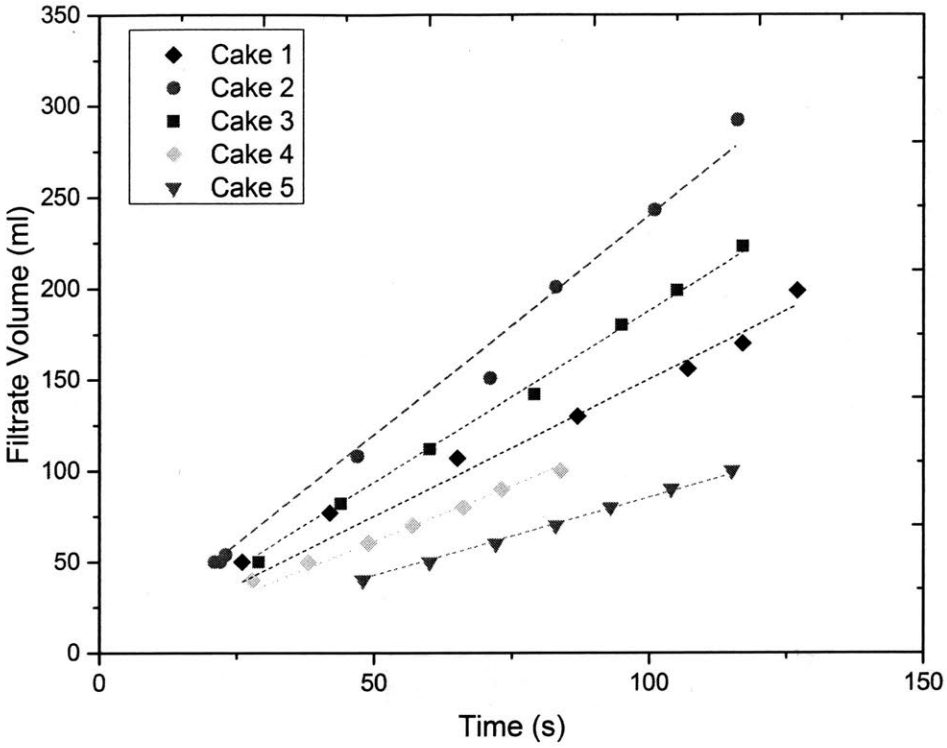

Figure 10-1: Filtrate volume versus time for a few example cakes from simple buchner funnel experiments

These results can then be applied to study the relationship between gypsum cake resistance and its crystal size distributions. Most literature models indicates there is a linear relationship between the cake permeability and the square of the mean particle size at a given porosity which can be computed in various ways using the first, second and the third moment of the particle distribution. Here, we again make use of image analysis to measure the two dimensional size distribution for more accurate moment calculation. Three models from the literature based on the CK equation [45, 54, 24] are compared and the model fitting are shown in figure 10-2. Here, because a 2D size distribution is measured, the first, second and third moments can be calculated based on a combination of the two dimensions. For each model, we found that $D_p = \frac{\mu_{1,1}}{\mu_{0,1}}$, $D_p = \frac{\mu_{2,1}}{\mu_{1,1}}$ and $D_p^2 = \frac{\mu_{2,1}}{\mu_{0,1}}$ outperforms the other ways of computing mean particle size slightly. All models seems to capture the trend to a reasonable degree although none of them are perfect. It is recommended to collect more data and testing out

the additive principle [12] to find resistance for cakes made of particles with a size distribution.

$$\kappa = a\frac{\epsilon^3}{(1-\epsilon)^2}(\frac{\mu_2}{\mu_1})^2 \text{ (MacDonald et al, 1991)}$$

$$\kappa = \frac{1}{72c}\frac{\epsilon^3}{(1-\epsilon)^2}(\frac{\mu_3}{\mu_2})^2 \text{ (Panda et al, 1994)}$$

$$\kappa = \frac{1}{18kv(\epsilon)}\frac{\epsilon^2}{(1-\epsilon)}\frac{\mu_3}{\mu_1} \text{ (Endo et al, 2001)}$$

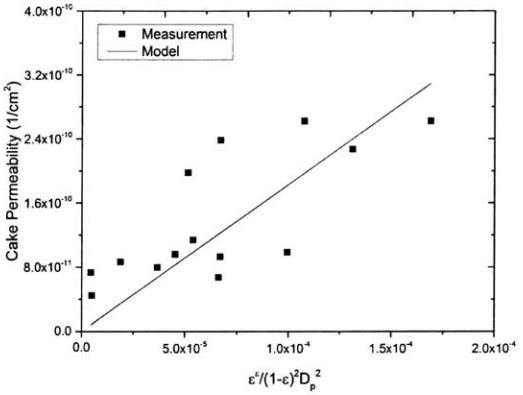

(a) MacDonald et al, 1991

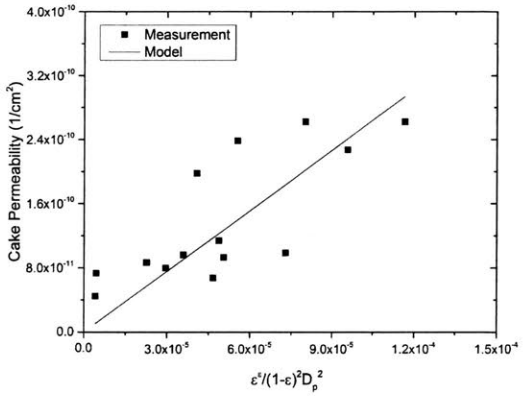

(b) Panda et al, 1994

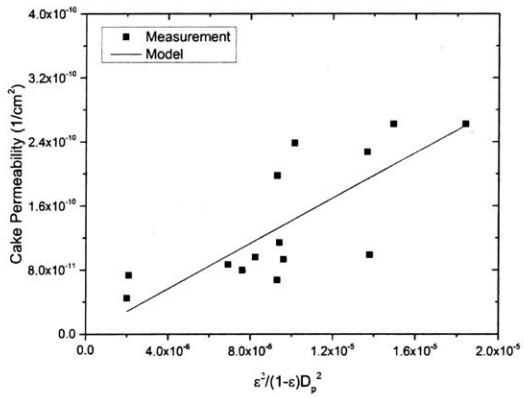

(c) Endo et al, 2001

Figure 10-2: Filtration model comparison: based on 2D size distribution for moment calculation

10.2.2 Total Impurity Inhibition Effect

Although we studied the effect of Mg^{2+} and Al^{3+} ions, there are still more metal ions in the system that might play a significant role in modifying the crystallization process. Since not all impurity's effect are fully explored in this work, it would be interesting to find out what other impurities are important and how important they are. One simple way to check if other impurity's kinetic effect needs to be added is to run the reactive crystallization experiments with all impurities present and compare the model predicted growth rate assuming only Mg^{2+} and Al^{3+} are the key shape modifiers. If the predicted growth rate is close to the measured value, it might not be necessary to keep adding other impurity's inhibition effect. If there is large deviation, then more experiments should be carried out to close that gap.

THIS PAGE INTENTIONALLY LEFT BLANK

Bibliography

[1] E. Aamir, Z. K. Nagy, C. D. Rielly, T. Kleinert, and B. Judat. Combined quadrature method of moments and method of characteristics approach for efficient solution of population balance models for dynamic modeling and crystal size distribution control of crystallization processes. *Industrial & Engineering Chemistry Research*, 48(18):8575–8584, 2009.

[2] E. A. Abdel-Aal, M. M. Rashad, and H. El-Shall. Crystallization of calcium sulfate dihydrate at different supersaturation ratios and different free sulfate concentration. *Crystal Research and Technology*, 39(4):313–321, 2004.

[3] D. S. Abrams and J. M. Prausnitz. Statistical thermodynamics of liquid mixtures: A new expression for the excess gibbs energy of partly or completely miscible systems. *AIChE Journal*, 21(1):116–128, 1975.

[4] A. H. Alexopoulos, A. I. Roussos, and C. Kiparissides. Part i: Dynamic evolution of the particle size distribution in particulate processes undergoing combined particle growth and aggregation. *Chemical Engineering Science*, 59(24):5751–5769, 2004.

[5] A. B. Amin and M. A. Larson. Crystallization of calcium sulfate from phosphoric acid. *Industrial & Engineering Chemistry Process Design and Development*, 7(1):133–137, 1968.

[6] A. Anderko, P. Wang, and M. Rafal. Electrolyte solutions: From thermodynamic and transport property models to the simulation of industrial processes. *Fluid Phase Equilibria*, 194:123–142, 2002.

[7] J.M. Astilleros, L. Fernández-Díaz, and A. Putnis. The role of magnesium in the growth of calcite: An afm study. *Chemical Geology*, 271(1):52–58, 2010.

[8] G. Azimi and V. G. Papangelakis. Thermodynamic modeling and experimental measurement of calcium sulfate in complex aqueous solutions. *Fluid Phase Equilibria*, 290(1):88–94, 2010.

[9] G Azimi, V. G. Papangelakis, and J. E. Dutrizac. Modelling of calcium sulphate solubility in concentrated multi-component sulphate solutions. *Fluid Phase Equilibra*, 260(2):300–315, 2007.

[10] G. Azimi, V. G. Papangelakis, and J. E. Dutrizac. Development of an MSE-based chemical model for the solubility of calcium sulphate in mixed chloride–sulphate solutions. *Fluid Phase Equilibra*, 266(1):172–186, 2008.

[11] P. Becker. *Phosphates and Phosphoric Acid: Raw Materials, Technology, and Economics of the Wet Process.* M. Dekker, New York, 2nd edition, 1989.

[12] D. Bourcier, J. P. Féraud, D. Colson, K. Mandrick, D. Ode, E. Brackx, and F. Puel. Influence of particle size and shape properties on cake resistance and compressibility during pressure filtration. *Chemical Engineering Science*, 144:176–187, 2016.

[13] W. K. Burton, N Cabrera, and F. C. Frank. The growth of crystals and the equilibrium structure of their surfaces. *Philosophical Transactions of the Royal Society of London A: Mathematical, Physical and Engineering Sciences*, 243(866):299–358, 1951.

[14] N. Cabrera and D. A. Vermilyea. The growth of crystals from solution. *Growth and Perfection of Crystals*, pages 393–410, 1958.

[15] J. Canny. A computational approach to edge detection. *IEEE Transactions on Pattern Analysis and Machine Intelligence*, (6):679–698, 1986.

[16] C. Chen and Y. Song. Generalized electrolyte-nrtl model for mixed-solvent electrolyte systems. *AlChE J.*, 50(8):1928–1941, 2004.

[17] W. Cheng, Q. Bo, F. Cheng, and Z. Du. Crystal growth rate of KCl in theKCl–$MgCl_2$–H_2O system based on MSE modeling. *Industrial & Engineering Chemistry Research*, 52(49):17658–17666, 2013.

[18] C. B. B. Costa, M. R. W. Maciel, and F. R. Maciel. Considerations on the crystallization modeling: Population balance solution. *Computers & Chemical Engineering*, 31(3):206–218, 2007.

[19] R. J. Davey and J. W. Mullin. Growth of the {100} faces of ammonium dihydrogen phosphate crystals in the presence of ionic species. *Journal of Crystal Growth*, 26(1):45–51, 1974.

[20] K. J. Davis, P. M. Dove, and J. J. De Yoreo. The role of Mg^{2+} as an impurity in calcite growth. *Science*, 290(5494):1134–1137, 2000.

[21] J. C. De Anda, X. Z. Wang, and K. J. Roberts. Multi-scale segmentation image analysis for the in-process monitoring of particle shape with batch crystallisers. *Chemical Engineering Science*, 60(4):1053–1065, 2005.

[22] J. J. De Yoreo and P. G. Vekilov. Principles of crystal nucleation and growth. *Reviews in Mineralogy and Geochemistry*, 54(1):57–93, 2003.

[23] M. El Moussaouiti, R. Boistelle, A. Bouhaouss, and J. P. Klein. Crystallization of calcium sulphate hemihydrate in concentrated phosphoric acid solutions. *Chemical Engineering Journal*, 68(2):123–130, 1997.

[24] Y. Endo, D. Chen, and D. Y Pui. Air and water permeation resistance across dust cakes on filtersâĂŤeffects of particle polydispersity and shape factor. *Powder Technology*, 118(1):24–31, 2001.

[25] G. Févotte, N. Gherras, and J. Moutte. Batch cooling solution crystallization of ammonium oxalate in the presence of impurities: study of solubility, supersaturation, and steady-state inhibition. *Crystal Growth & Design*, 13(7):2737–2748, 2013.

[26] X. Gao, H. Wang, Y. Zhong, Z. Luo, K. Cen, M. Ni, and L. Chen. Effects of magnesium and ferric ions on crystallization of calcium sulfate dihydrate under the simulated conditions of wet flue-gas desulfurization. *Chemical Research in Chinese Universities*, 24(6):688–693, 2008.

[27] R. L. Gilbert Jr. Crystallization of gypsum in wet process phosphoric acid. *Industrial & Engineering Chemistry Process Design and Development*, 5(4):388–391, 1966.

[28] B. Guan, L. Yang, and Z. Wu. Effect of Mg2+ ions on the nucleation kinetics of calcium sulfate in concentrated calcium chloride solutions. *Industrial & Engineering Chemistry Research*, 49(12):5569–5574, 2010.

[29] S. K. Hamdona and U. A. Al Hadad. Crystallization of calcium sulfate dihydrate in the presence of some metal ions. *Journal of Crystal Growth*, 299(1):146–151, 2007.

[30] D. Hasson, J. Addai-Mensah, and J. Metcalfe. Filterability of gypsum crystallized in phosphoric acid solution in the presence of ionic impurities. *Industrial & Engineering Chemistry Research*, 29(5):867–875, 1990.

[31] S. He, J. E. Oddo, and M. B. Tomson. The seeded growth of calcium sulfate dihydrate crystals in NaCl solutions up to 6 m and 90 c. *J. Colloid Interface Sci.*, 163(2):372–378, 1994.

[32] E. J. Hukkanen and R. D. Braatz. Measurement of particle size distribution in suspension polymerization using in situ laser backscattering. *Sensors and Actuators B: Chemical*, 96(1):451–459, 2003.

[33] H. Hulburt and S. Katz. Some problems in particle technology: A statistical mechanical formulation. *Chemical Engineering Science*, 19(8):555–574, 1964.

[34] D. John. Grapical methods for study of dissolved aluminum complexes (*).

[35] A. Kruger, W. W. Focke, Z. Kwela, and R. Fowles. Effect of ionic impurities on the crystallization of gypsum in wet-process phosphoric acid. *Industrial & Engineering Chemistry Research*, 40(5):1364–1369, 2001.

[36] N. Kubota. Effect of impurities on the growth kinetics of crystals. *Crystal Research and Technology*, 36(8-10):749–769, 2001.

[37] N. Kubota and J. W. Mullin. A kinetic model for crystal growth from aqueous solution in the presence of impurity. *Journal of Crystal Growth*, 152(3):203–208, 1995.

[38] N. Kubota, M. Yokota, and J. W. Mullin. The combined influence of supersaturation and impurity concentration on crystal growth. *Journal of crystal growth*, 212(3):480–488, 2000.

[39] O. I. Kurteva and E. B. Brustkus. Solubilities of calcium sulfate in H_3PO_4 + H_2SO_4 and H_3PO_4 + H_2SiF_6 acid mixtures. *Zhurnal Prikladnoi Khimii*, 34(1):1714–1722, 1961.

[40] K. Lai, J. Chen, C. Liu, and S. Yang. Effect of permeability–porosity functions on simulated morphological evolution of a chemical dissolution front. *Hydrological Processes*, 28(1):16–24, 2014.

[41] J. Li, J. Wang, and Y. Zhang. Effects of the impurities on the habit of gypsum in wet-process phosphoric acid. *Industrial & Engineering Chemistry Research*, 36(7):2657–2661, 1997.

[42] Y. Lin, A. T. Kate, M. Mooijer, J. Delgado, P. L. Fosbøl, and K. Thomsen. Comparison of activity coefficient models for electrolyte systems. *AIChE Journal*, 56(5):1334–1351, 2010.

[43] S. Liu and G. H. Nancollas. The kinetics of crystal growth of calcium sulfate dihydrate. *Journal of Crystal Growth*, 6(3):281–289, 1970.

[44] J. R. Loehe and M. D. Donohue. Recent advances in modeling thermodynamic properties of aqueous strong electrolyte systems. *AlChE Journal*, 43(1):180–195, 1997.

[45] M. J. MacDonald, C. Chu, P. P. Guilloit, and K. M. Ng. A generalized blake-kozeny equation for multisized spherical particles. *AIChE Journal*, 37(10):1583–1588, 1991.

[46] P. M. Martins, F. A. Rocha, and P. Rein. The influence of impurities on the crystal growth kinetics according to a competitive adsorption model. *Crystal Growth & Design*, 6(12):2814–2821, 2006.

[47] A. Mersmann. *Crystallization Technology Handbook*. Marcel Dekker, New York, 2nd edition, 2001.

[48] A. Mersmann. *Crystallization Technology Handbook.* Marcel Dekker, New York, 2nd edition, 2001. pg. 98.

[49] J. W. Mullin and O. Söhnel. Expressions of supersaturation in crystallization studies. *Chemical Engineering Science*, 32(7):683–686, 1977.

[50] S. Murugesan, D. M. Hallowand, J. P. Vernille, J. W. Tom, and J. E. Tabora. Lean filtration: approaches for the estimation of cake properties. *Organic Process Research & Development*, 16(1):42–48, 2011.

[51] A. S. Myerson. *Handbook of Industrial Crystallization.* Butterworth-Heinemann, Woburn, MA, 2nd edition, 2002.

[52] M. Ohara and R. C. Reid. *Modeling Crystal Growth Rates From Solution.* Prentice Hall, Englewood Cliffs, NJ, 1973.

[53] I. Owczarek and K. Sangwal. Effect of impurities on the growth of kdp crystals: Mechanism of adsorption on (101) faces. *Journal of Crystal Growth*, 102(3):574–580, 1990.

[54] M. N. Panda and L.W. Lake. Estimation of single-phase permeability from parameters of particle-size distribution. *American Association of Petroleum Geologists Bulletin*, 78(7):1028–1039, 1994.

[55] Y. Peng, Z. Zhu, R. D. Braatz, and A. S. Myerson. Gypsum crystallization during phosphoric acid production: Modeling and experiments using the mixed-solvent-electrolyte thermodynamic model. *Industrial & Engineering Chemistry Research*, 54(32):7914–7924, 2015.

[56] K. S. Pitzer and G. Mayorga. Thermodynamics of electrolytes. ii. activity and osmostic coefficients for strong electrolytes with one or both ions univalent. *Journal of Physical Chemistry.*, 77(19):2300–2308, 1973.

[57] B. Plumer. This terrifying chart shows we're not growing enough food to feed the world.

[58] F. Puel, G. Févotte, and J. P. Klein. Simulation and analysis of industrial crystallization processes through multidimensional population balance equations. part 1: a resolution algorithm based on the method of classes. *Chemical Engineering Science*, 58(16):3715–3727, 2003.

[59] S. Qamar and G. Warnecke. Numerical solution of population balance equations for nucleation, growth and aggregation processes. *Computers & Chemical Engineering*, 31(12):1576–1589, 2007.

[60] A. D. Randolph and M. A. Larson. *Theory of Particulate Processes: Analysis and Techniques in Continuous Crystallization.* Academic Press, San Diego, CA, 2nd edition, 1988.

[61] M. M. Rashad, M. H. H. Mahmoud, I. A. Ibrahim, and E. A. Abdel-Aal. Crystallization of calcium sulfate dihydrate under simulated condition of phosphoric acid production in the presence of aluminum and magnesium ions. *Journal of Crystal Growth*, 267:372–379, 2004.

[62] M. M. Rashad, M. H. H. Mahmoud, I. A. Ibrahim, and E. A. Abdel-Aal. Crystallization of calcium sulfate dihydrate under simulated conditions of phosphoric acid production in the presence of aluminum and magnesium ions. *Journal of Crystal Growth*, 267(1):372–379, 2004.

[63] S. I. Sandler. *Models for Thermodynamic and Phase Equilibria Calculations.* Dekker, New York, 1994.

[64] K. Sangwal. Kinetic effects of impurities on the growth of single crystals from solutions. *Journal of Crystal Growth*, 203(1):197–212, 1999.

[65] K. Sangwal. *Additives and crystallization processes: from fundamentals to applications.* John Wiley & Sons, 2007.

[66] B. Simon, A. T. Grassi, and R. Boistelle. Cinétique de croissance de la face (110) de la paraffine c36h74 en solution: I. croissance en mileu pur. *Journal of Crystal Growth*, 26(1):77–89, 1974.

[67] J. M. Sullivan, J. J. Kohler, and J. H. Grinstead Jr. Solubilities of α-calcium sulfate hemihydrate 40, 45, 50, and 55 % P_2O_5 phosphoric acid solutions at 80, 90, 100 and 110 °C. *Journal of Chemical Engineering Data*, 33:367–370, 1988.

[68] A. A. Taperova. L'analyse physicochimique dans le domaine du traitement des phosphates par l'acide sulfurique. *Zhurnal Prikladnoi Khimii*, 13(1):634–651, 1940.

[69] A. A. Taperova and M. H. Shulgiva. Solubilities of $CaSO_4$ hydrates in phosphoric acid. *Zhurnal Prikladnoi Khimii*, 18(1):521–528, 1945.

[70] T. N. Thomas, T. A. Land, M. Johnson, and W. H. Casey. Molecular properties of adsorbates that affect the growth kinetics of archerite (kdp). *Journal of Colloid and Interface Science*, 280(1):18–26, 2004.

[71] T. Togkalidou, H.-H. Tung, Y. Sun, A. Andrews, and R. D. Braatz. Parameter estimation and optimization of a loosely-bound aggregating pharmaceutical crystallization using in-situ infrared and laser backscattering measurement. *Industrial & Engineering Chemistry Research*, 43(11):6168–6181, 2004.

[72] J. Ulrich. Growth rate dispersion: a review. *Crystal Research and Technology*, 24(3):249–257, 1989.

[73] A. E. D. M. Van Der Heijden, J. P. Van Der Eerden, and G. M. Van Rosmalen. The secondary nucleation rate: A physical model. *Chemical Engineering Science*, 49(18):3103–3113, 1994.

[74] S. Van Der Sluis, G. J. Witkamp, and G. M. Van Rosmalen. Crystallization of calcium sulphate in concentrated phosphoric acid. *Journal of Crystal Growth*, 79:620–629, 1986.

[75] D. Vidal, C. Ridgway, G. Pianet, J. Schoelkopf, R. Roy, and F. Bertrand. Effect of particle size distribution and packing compression on fluid permeability as predicted by lattice-boltzmann simulations. *Computers & Chemical Engineering*, 33(1):256–266, 2009.

[76] P. Wang, A. Anderko, R. D. Springer, and R. D. Young. Modeling phase equilibria and speciation in mixed-solvent electrolyte systems: Ii. liquid–liquid equilibria and properties of associating electrolyte solutions. *Journal of Molecular Liquids*, 125(1):37–44, 2006.

[77] P. Wang, A. Anderko, and R. D. Young. A speciation-based model for mixed-solvent electrolyte systems. *Fluid Phase Equilibria*, 203(1):141–176, 2002.

[78] P. Wang, A. Anderko, and R. D. Young. A speciation-based model for mixed-solvent electrolyte systems. *Fluid Phase Equilibria*, 203(1):141–176, 2002.

[79] H. Wei and J. Garside. Application of CFD modelling to precipitation systems. *Chemical Engineering Research and Design*, 75(2):219–227, 1997.

[80] E. T. White and S. Mukhopadhyay. Crystallization of gypsum from phosphoric acid solutions. In A. S. Myerson and K. Toyokura, editors, *Crystallization as a Separations Process*, chapter 23, pages 292–315. American Chemical Society, Washington, DC, 1990.

[81] E. T. White and P. G. Wright. Magnitude of size dispersion effects in crystallization. In *Chemical Engineering Progress Symposium Series No*, volume 110, pages 81–87, 1971.

[82] G. J. Witkamp, J. P. Van der Eerden, and G. M. Van Rosmalen. Growth of gypsum: I. kinetics. *Journal of Crystal Growth*, 102(1):281–289, 1990.

[83] J. Worlitschek and M. Mazzotti. Model-based optimization of particle size distribution in batch-cooling crystallization of paracetamol. *Crystal Growth & Design*, 4(5):891–903, 2004.

[84] Y. Yoshikawa, G. H. Nancollas, and J. Barone. The kinetic of crystallization of group II fluoride salts in aqueous solution. *Journal of Crystal Growth*, 69(2):357–361, 1984.

[85] A. B. Yu, R. P. Zou, and N. Standish. Modifying the linear packing model for predicting the porosity of nonspherical particle mixtures. *Industrial & Engineering Chemistry Research*, 35(10):3730–3741, 1996.

[86] Z. Zhu, Y. Peng, A. S. Myerson, and R. D. Braatz. Multidimensional population balance model of the continuous crystallization of gypsum with growth rate dispersion. *submitted.*

[87] R. C. Zumstein and R. W. Rousseau. Growth rate dispersion in batch crystallization with transient conditions. *AIChE Journal*, 33(11):1921–1925, 1987.